Nonlinear Ionospheric Propagation Effects on UHF and VLF Radio Signals

by

Keith Michael Groves

B.S., Physics, Andrews University
(1984)

Submitted to the Department of Earth, Atmospheric and Planetary Sciences
in partial fulfillment of the requirements for the degree of

Doctor of Philosophy

at the

MASSACHUSETTS INSTITUTE OF TECHNOLOGY

September 1991

Author .....
Department of Earth, Atmospheric and Planetary Sciences
September 3, 1991

Certified by .....
Min-Chang Lee
Thesis Supervisor

Certified by .....
John C. Foster
Thesis Supervisor

Accepted by .....
Thomas H. Jordan
Department Head

Nonlinear Ionospheric Propagation Effects on UHF and VLF Radio Signals

by

Keith Michael Groves

Submitted to the Department of Earth, Atmospheric and Planetary Sciences
on September 3, 1991, in partial fulfillment of the
requirements for the degree of
Doctor of Philosophy

Abstract

An investigation of nonlinear wave-plasma interactions in the ionosphere causing significant propagation effects on VLF and UHF radio waves has been conducted. Nonlinear scattering of VLF waves off existing density irregularities is shown to be responsible for the observed spectral broadening reported by Bell et al. [1983]. When the irregularity scale size does not exceed a few tens of meters, the scattered wave is found to be a quasi-electrostatic elliptically polarized mode with a much larger wave number than the incident VLF wave. The large wave number results in significant Doppler broadening of the wave spectrum received by a moving satellite. For large amplitude VLF waves, parametric instabilities generating lower hybrid waves and short scale electron density fluctuations are predicted. A series of radar experiments were conducted in conjunction with the ACTIVE satellite to test the VLF wave propagation hypotheses. Incoherent scatter UHF radars at Millstone Hill and Arecibo Observatory were employed to diagnose the ionosphere for evidence of enhanced radar backscatter induced by powerful VLF waves launched from the satellite's 10 kW VLF transmitter; it was expected that the electric field amplitudes in the vicinity of the satellite would exceed the parametric instability thresholds. Experimental confirmation of this phenomenon was not conclusively obtained because the actual VLF radiated power levels were at least 20 dB less than anticipated. Intense enhancements ($\sim$ 20 dB) of the normal UHF radar backscatter have recently been observed with the Millstone Hill, EISCAT and Sondreström incoherent scatter radars in the presence of intense field-aligned currents, elevated electron temperatures, and red aurora [*Foster, et al.*, 1988; *Rietveld, et al.*, 1991; *Collis, et al.*,1991]. Current driven source mechanisms proposed by Rosenbluth and Rostoker [1962] and Kindel and Kennel [1971] partially explain these observations. A new mechanism is presented whereby ion acoustic waves are amplified through the nonlinear coupling of intense Langmuir waves generated by suprathermal electrons. Large populations of suprathermal electrons are a regular feature of auroral arcs and field-aligned currents. A Langmuir

wave spectrum is calculated based on an electron distribution function constructed from satellite data. The Langmuir waves are then coupled via the ponderomotive force and subsequently amplify ion acoustic wave modes. For the distribution function considered here, nearly two orders of magnitude enhancement are predicted for wave numbers corresponding to UHF backscatter radars. This mechanism can act in addition to known current driven processes to stimulate ion acoustic wave growth, and it predicts some previously unexplained features of the observations, such as the symmetric enhancement of both peaks of the ion acoustic power spectrum. Failure to include the nonlinear coupling effect results in overestimation of the field-aligned current intensities required to produce observed enhancements.

Thesis Supervisor: Prof. Min-Chang Lee
Title: Head of Ionospheric Plasma Research Group
Plasma Fusion Center

Thesis Supervisor: Dr. John C. Foster
Title: Assistant Director of Atmospheric Sciences
MIT Haystack Observatory

Acknowledgments

I am both fortunate and grateful to have had the opportunity to pursue graduate studies at MIT. Compiling an exhaustive list of the people who have supported, guided, encouraged, motivated, and otherwise aided and abetted my efforts to complete this project would prove nearly as taxing as the actual writing of the thesis. Nevertheless, I will attempt to recognize those individuals and groups whose contributions were foremost.

I am especially grateful to my adviser, Min-Chang Lee. His enthusiasm, support and guidance were surpassed only by his personal commitment to my progress. By his example of perseverance and diligence in professional endeavors, I have learned a great deal.

The contribution of John Foster cannot be overstated. His patient instruction, encouragement and understanding imparted hope, confidence and motivation to forge on. I am also indebted to his cheerful tolerance (and support) of my quest to visit every major IS radar site in the world.

Working with the Ionospheric Plasma Research Group has been an enjoyable privilege. Special recognition belongs to Karen Koh and Chan Yoo, for their untiring efforts during the Arecibo campaign and many good discussions.

My interactions with the crew at the Millstone Hill Radar site are the source of productive results and many fine memories. I would particularly like to thank Steve Cariglia for his spontaneous assistance on numerous occasions, and Steve Cohn, with whom I have shared the privileged position of graduate student at the Hill.

I would like to thank the members of my thesis committee, Richard Lindzen, Ron Prinn, and Earle Williams, for their patient participation in evaluating a dissertation on this topic.

Special thanks also go to Edward Lorenz, who supported me financially during the early stages of my graduate work at MIT and made this possible.

In the course of acquiring data from other sites and working on various topics, I have had the opportunity to interact with a number of outstanding individuals working outside the Institute who deserve my sincere gratitude and recognition for their interest and efforts on my behalf. These include:

> Jack Klobuchar, who, from the beginning, has offered unwavering support and encouragement.
>
> Frank Djuth, John Elder, and Ken Williams for their unselfish support in data acquisition and analysis at Arecibo and Millstone Hill, and generous contributions of ideas, discussions, and good humor.

Mike Sulzer, without whose expert assistance making and interpreting measurements at Arecibo would not have been possible.

Tony van Eyken, Mike Rietveld, and Kristian Schlegel for making my experience at EISCAT productive, rewarding, and fun.

Mary McCready and Bob Livingston for their gracious support in acquiring and processing Sondreström. data.

Bill Peterson, whose patient help with DE-1 enabled the MICAD campaign to move forward.

Terry Hughes and the rest of the CANOPUS science team for their ready willingness to support the MICAD experiments.

I would also like to thank two physics professors from my undergraduate years, Robert Kingman and Clark Rowland, for giving me the confidence and the competence to get started down this road.

Sharing my experience with friends at MIT has made it both worthwhile and enjoyable. I would especially like to thank those amazing meteorologists Robert X. Black III, Chris Davis, and Josh Wurman; those down-to-earth geophysicists, Randy Mackie and Mike Bergman; and the last great Synoptic Lab instructor, Peter Neilley, who enabled me to graduate a few hours early.

A special debt of gratitude is owed to April Ratana. Her companionship has supplied a source of strength and understanding, laughter, and renewed perspective when things got crazy.

My family has provided unconditional support and encouragement. I would like to extend my appreciation to my siblings, Cindy, Terry, Sherry, Brad and Jennifer, their spouses, and their wonderful too-numerous-to-name children who have known me as a student all their lives. Finally, I would like to thank my parents, Marge and Clarence, to whom this thesis is dedicated. Their lives of unselfish dedication and committment to their family and each other have been an inspiration to us all.

Contents

Chapter 1

Introduction

Significant interactions of the earth's upper atmosphere with radio waves were first recognized near the turn of the century when Marconi transmitted radio waves across the Atlantic. Pioneering wave reflection experiments by Appleton and Barnett [1925] and Breit and Tuve [1925] verified the existence of a conducting layer known as the ionosphere in the earth's upper atmosphere, determining its height and stratified nature. Since that time a multitude of propagation effects have been discovered, ranging from total wave reflection to weak scintillations of phase and amplitude depending on the frequency, intensity, and propagation angle of the incident waves and the density, temperature, and structure of the ionosphere.

While some of the wave modification effects induced by the ionosphere have been utilized beneficially by man [e.g., long range communications], others present significant obstacles to reliable communication and navigation systems; in either case, an examination of the underlying physics is necessary to mitigate undesirable effects or exploit those which may prove beneficial. Presented here is an investigation of significant ionospheric effects on the propagation of radio waves in two distinctly different frequency regimes, VLF and UHF.

1.1 Overview

The present work describes the results of investigations of nonlinear wave–plasma interaction processes generally characterized by the exchange of energy between one or more wave modes and the charged particles in the upper atmosphere.

These processes are divided into two classes of phenomena based on the frequencies of the wave modes involved in the interactions. One class is that of VLF (3–30 kHz) wave interactions with space plasmas. Investigations of VLF wave interactions were conducted primarily to address the unexplained observations of significant ($\sim$1% of the carrier frequency) spectral broadening of VLF waves traversing the ionosphere [*Bell et al.*, 1983]. The VLF effects considered include those from small amplitude waves, where the plasma acts to scatter the incident waves in a nonlinear process, and those induced by powerful VLF waves, found to be capable of significantly modifying the plasma medium through parametric instabilities. A unique experimental program to test the validity of these mechanisms was carried out as well; inconclusive results were obtained due to equipment failures on the satellite employed in these efforts.

The second class of interaction involves significant underdense plasma effects on UHF (300 – 3000 MHz) radiation. This work was driven, both observationally and theoretically, by the discovery of dramatic natural enhancements of the UHF radar backscatter signal [*Foster et al.*, 1988]. Observational evidence of this phenomenon has been acquired from three major incoherent scatter radar sites. Existing theories of UHF backscatter enhancements are considered, and a nonlinear coupling mechanism is developed which compares favorably with the observations.

1.1.1 Description of Topics

The propagation characteristics of VLF waves (3–30 kHz) in the ionosphere will be presented in Chapter 2, followed by a description of the unanticipated spectral

broadening experienced by VLF waves on transionospheric ray paths. Essentially monochromatic VLF waves (± 1 Hz) injected into the ionosphere by powerful ground-based transmitters were sometimes found to have a spectral width of up to a few hundred Hertz when measured by satellites in the ionosphere [*Bell, et al.*, 1983]. A new nonlinear scattering mechanism is developed to explain the observed bandwidth expansion. The scattered modes are found to have short wavelengths which give rise to appreciable Doppler shifts (i.e., broadening) when detected by orbiting satellites.

Initially motivated by the spectral broadening observations addressed in Chapter 2, Chapter 3 presents a theoretical analysis of the expected effects of the VLF wave on the plasma when the amplitude becomes large. Specifically, the theory of a two-step parametric instability in which the VLF wave excites electrostatic lower hybrid oscillations is investigated. In the first step the incident VLF pump waves excite lower hybrid waves and a short scale (10–20 m) purely growing mode. The lower hybrid waves excited in the first step may then excite lower hybrid sidebands and a low frequency mode in the second step. Ionospheric density fluctuations and the acceleration of electrons and ions producing airglow are predicted. A quantitative analysis of the instability's thresholds, growth rates and induced effects in different altitude regimes is included.

Chapter 4 contains a description and analysis of unique experimental efforts to observationally verify the theoretical results presented in Chapters 2 and 3. Experiments utilized the recently launched ACTIVE satellite as an in-situ source of powerful VLF radiation and employed incoherent scatter radars, VLF receivers and satellite borne instruments to diagnose expected effects. These included enhanced radar backscatter, electron and ion heating, electron precipitation, and airglow. The HF heating facility at Arecibo Observatory was also used in some of the experiments to induce spectral broadening of the transmitted VLF waves. Results from these experiments proved

inconclusive, however, because of problems with the VLF transmitter onboard the satellite.

The remainder of the dissertation explores significant propagation effects for UHF waves (300–3000 MHz), specifically the large cross section enhancement for UHF backscatter at ion acoustic wave frequencies. These enhancements had not been recognized as a geophysical phenomenon previously, having been dismissed as satellites penetrating the radar beam. Observations from the Millstone Hill Radar located in Westford, Massachusetts and two other high latitude incoherent radar sites, EISCAT and Sondreström, show that up to a few percent of the coherent echoes received by the radars are actually geophysical enhancements associated with intense field-aligned currents, elevated electron temperatures, and red aurora in most cases [*Foster et al.*, 1988; *Rietveld et al.*, 1991; *Collis et al.*, 1991]. These data are presented in Chapters 5 and 6.

Explanations for the observed enhancements are explored in Chapter 7. These include a consideration of existing current-driven theories applied to the recent observations and a newly proposed mechanism promoting the growth of ion acoustic waves via the nonlinear coupling of intense Langmuir waves. The intense Langmuir waves are proposed to be generated by the relatively large population of suprathermal electrons associated with auroral activity during magnetically disturbed conditions. The nonlinear coupling mechanism provides good agreement with many observed features of the data, including the magnitude of the enhancements and the symmetric enhancement of upgoing and downgoing ion acoustic waves.

Chapter 8 contains a brief summary of significant results from the previous six chapters, which are fairly focused and somewhat self-contained.

The characteristics of most of the wave phenomena considered in this work can be adequately described by the fluid model of a plasma. The governing fluid equa-

tions, given in Appendix A, form the basis for the description of the plasma waves presented here and will be referred to often. The general approach is to linearize the equations assuming perturbations about a zeroth order equilibrium state. Valid simplifying assumptions will be applied whenever possible in specific applications to reduce needless algebra and complications which may obscure the underlying physics.

Chapter 2

Spectral Broadening of VLF Signals

In this chapter we investigate the observed (~10% of the carrier frequency) spectral broadening experienced by VLF waves traversing the ionosphere. A description of this phenomenon is presented, followed by the derivation of a new theory predicting the nonlinear scattering of incident VLF waves by plasma density irregularities [*Groves et al.*, 1988]. For irregularity scale lengths less than about 100 meters, the scattered wave is a quasi-electrostatic mode with much shorter wavelength than the incident waves. The reduced wavelength gives rise to a large Doppler shift ($\Delta f \propto \lambda^{-1}$) when the waves are received by moving satellites, producing an apparent broadening in the power spectrum.

Whistler Waves

In the absence of a magnetic field radio signals with frequencies lower than the local plasma frequency in the ionosphere can not propagate in the plasma medium. In the daytime ionosphere a typical peak electron density is about $10^{12}\mathrm{m}^{-3}$, implying that the region remains impenetrable to radiation with frequencies less than about

10 MHz. The presence of the earth's magnetic field, however, introduces anisotropy to the upper atmosphere through its direct effects on the motion of charged particles. When the quasi-static field is included in the equations of motion, many new plasma wave modes are supported.

One such mode of great importance found to propagate along the magnetic field at very low frequencies ($\omega \ll \omega_{pe}$) was dubbed the "whistler mode" and was first explained by Storey [1953]. These electromagnetic waves are so named because they commonly occur in the audio frequency range and exhibit a falling tone due to the dispersive nature of their propagation.

Whistlers may be generated naturally by emissions from lightning or artificially produced by manmade VLF (3 kHz $< f <$ 30 kHz) transmissions [*Helliwell*, 1965]. Indeed, many navigation/communication systems operate in this frequency regime to transmit signals over great distances via reflections in the earth–ionosphere wave guide. VLF wave energy can escape the wave guide by entering the ionosphere in a whistler wave mode (see Figure 2-1). Furthermore, whistler wave interactions with the ionized medium can degrade the signal quality of transmitted VLF waves.

2.1 Observations of Spectral Broadening

A mechanism is proposed here to explain the recently observed bandwidth expansion that was experienced by nearly monochromatic signals at 13.6 kHz $\pm$1 Hz injected from a ground-based VLF transmitter as they traverse the ionosphere and reach satellite altitudes in the range of 600–3800 kilometers [*Bell et al.*, 1983]. A schematic illustration of this phenomenon is shown in Figure 2-2.

This expansion of bandwidth, which results in a proportional decrease in signal–to–noise ratio, may be nearly as large as 10% ($\geq$ 100 Hz) of the carrier frequency, and the off-carrier components are thought to be electrostatic in nature [*Inan and*

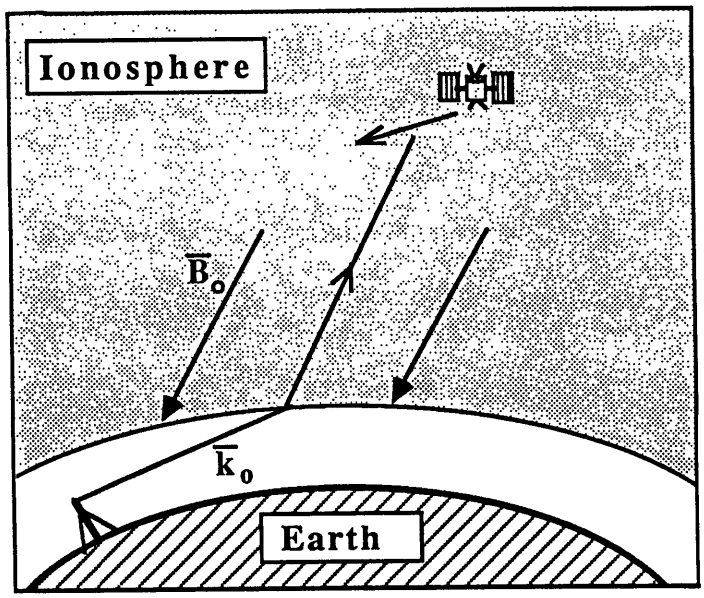

Figure 2-1: Propagation geometry of VLF wave from ground transmitter to satellite location

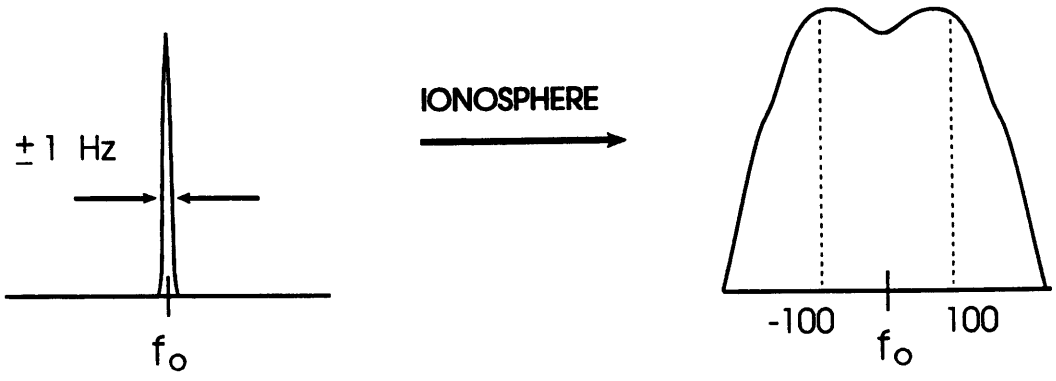

Figure 2-2: Bandwidth expansion of VLF wave following transionospheric propagation

Bell, 1985]. The five types of spectrally broadened transmitter signals which have been found are illustrated in Figure 2-3. They occur only in the presence of impulsive VLF hiss and/or a lower hybrid resonance (LHR) noise band with an irregular cutoff frequency, and only for signals whose frequencies exceed the LHR frequency at the satellite location. The observed signal at the carrier frequency is usually suppressed relative to the sidebands.

A linear scattering source mechanism was first suggested by Bell et al., [1983], who hypothesized the creation of the required ionospheric density fluctuations by precipitating, low energy ($<$ 1 kev) electrons. Such precipitation events have been accompanied by both VLF hiss and irregular LHR noise bands [*McEwen and Barrington*, 1967; *Laaspere et al.*, 1971; *Gurnett and Frank*, 1972]. Bell et al. [1983] then speculated that the broadening of the transmitted pulse spectrum results from the scattering of the initial signals from the precipitation-induced density fluctuations and the subsequent coupling into quasi-electrostatic whistler mode waves of short wavelength. The Doppler shift associated with these short wavelength modes is large enough to produce the bandwidth expansion of the signals measured on a moving satellite.

The mechanism described here, presented in section 2, differs from that of Bell et al.'s in that the proposed scattering is the nonlinear scattering of VLF signals by induced ionospheric density fluctuations resulting in the nonlinear mode conversion of VLF waves into lower hybrid waves [*Groves et al.*, 1988]. In other words, the scattering of VLF waves by ionospheric density fluctuations causes elliptically polarized modes. The induced elliptically polarized modes have much shorter scale lengths than the incident VLF waves and may be predominantly electrostatic. This has important consequences for the detection of such waves by orbiting satellites, since the measured Doppler shift associated with the spacecraft's velocity is inversely proportional to the

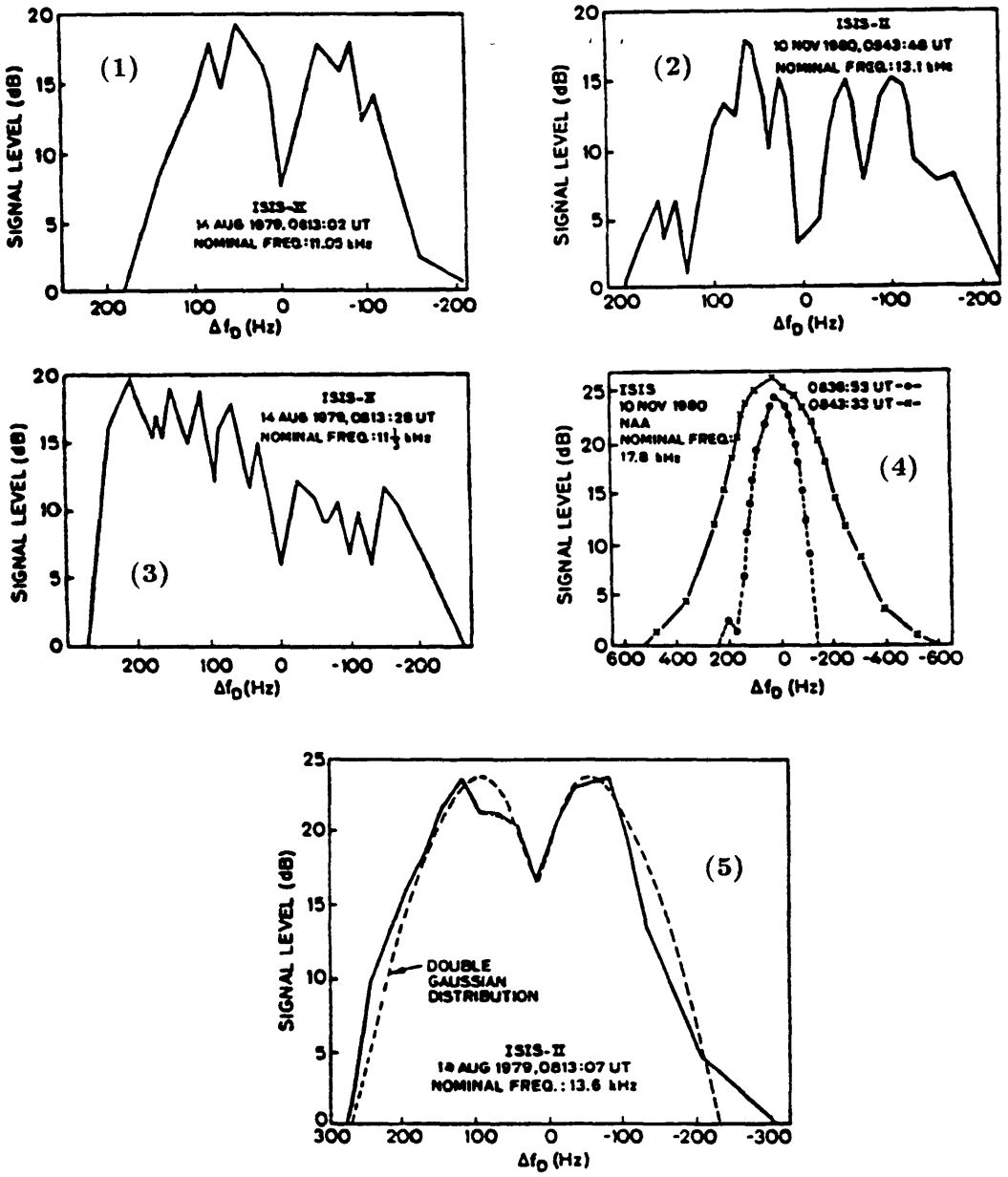

Figure 2-3: Five different types of observed spectral broadening. Type 4 is the most common. After Bell et al., [1983]

wave length.

The mechanism of Bell et al. [1983] requires that the linear scattering into short wavelength modes occur at low altitudes (200–300 km); these scattered waves must then propagate several hundred kilometers to be observed by satellites at altitudes exceeding 1000 km. The phase velocity of the short wavelength waves (~250 km/sec) is comparable to the electron thermal velocity in the plasma. These modes ($\lambda \approx 20$ m), then, experience heavy Landau damping as they propagate and are attenuated exponentially, effectively preventing them from reaching satellite altitudes.

By contrast, the nonlinear mechanism derived here predicts that the scattering process can occur at the satellite location because it depends only on the relative electron density fluctuation, $\delta n/n_o$, rather the electron density itself. In both mechanisms, the actual shape of the broadened spectrum is determined by the scale size spectrum of the existing irregularities. Relatively isotropic field-aligned irregularities produce a broadened Gaussian type spectrum such as that shown in Figure 2-3, # 4. Asymmetric and/or structured broadening may result when spatial gradients in irregularity amplitudes or scale sizes are present. Such spectra were observed less frequently than the symmetric Gaussian type [H. G. James, private communication, 1987].

2.2 Nonlinear Wave Scattering

I first derive a theory starting with the basic fluid equations and Maxwell's equations which predicts the nonlinear scattering of VLF (whistler) waves by ionospheric density fluctuations. A discussion of the consequences of this theory with regard to the spectral broadening phenomenon follows.

Theory

A monochromatic VLF wave transmitted from a ground-based station into space has been observed to change from linear into circular polarization (i.e., whistler mode). If a ducted whistler wave mode is considered for simplicity, the wave electric field may be represented as

$$\mathbf{E_o} = \mathrm{E_o}(\hat{\mathbf{x}} + \mathrm{i}\hat{\mathbf{y}}) \exp[\mathrm{i}(\mathrm{k_o z} - \omega_o \mathrm{t})] \tag{2.1}$$

where the z axis has been taken along the geomagnetic field lines, $\mathbf{B_o}$; ω_o is the transmitted wave frequency, and $\mathbf{k_o}$ the associated wave vector, assumed to be along the z axis for a ducted mode, as illustrated in Figure 2-4a. Propagating into an unperturbed ionosphere, the whistler wave satisfies the electromagnetic wave equation

$$\nabla^2 \mathbf{E_o} - \frac{1}{\mathrm{c}^2} \frac{\partial^2}{\partial \mathrm{t}^2} \mathbf{E_o} = \mu_o \frac{\partial}{\partial \mathrm{t}} \mathbf{j_o} \tag{2.2}$$

where $\mathbf{j_o}$ is the uniform oscillatory current driven by the incident wave field in the ionospheric plasma,

$$\mathbf{j_o} = \frac{\mathrm{ie}^2 \mathrm{N_o} \mathbf{E_o}}{\mathrm{m_e}(\omega_o - \Omega_e)} \tag{2.3}$$

and e, $\mathrm{N_o}$, $\mathrm{m_e}$ and Ω_e are the electron charge, uniform background plasma density, electron mass, and the unsigned electron cyclotron frequency, respectively. In the presence of field-aligned ionospheric density irregularities, the scattered wave, allowing for longitudinal modes, can be described by

$$\nabla(\nabla \cdot \mathbf{E_s}) - \nabla^2 \mathbf{E_s} + \frac{1}{\mathrm{c}^2} \frac{\partial^2}{\partial \mathrm{t}^2} \mathbf{E_s} = -\mu_o \frac{\partial}{\partial \mathrm{t}} \delta \mathbf{j_s} \tag{2.4}$$

where $\delta \mathbf{j_s}$ is the nonuniform current induced by the interaction of the whistler wave field with the density irregularities. We take the x axis along the direction of the density irregularities which are assumed to be of the form

$$\delta \mathrm{n} = \delta \tilde{\mathrm{n}} \exp[\mathrm{ikx}] \tag{2.5}$$

depicted graphically in Figure 2-4b. The nonuniform current, $\delta \mathbf{j_s}$, can then be ex-

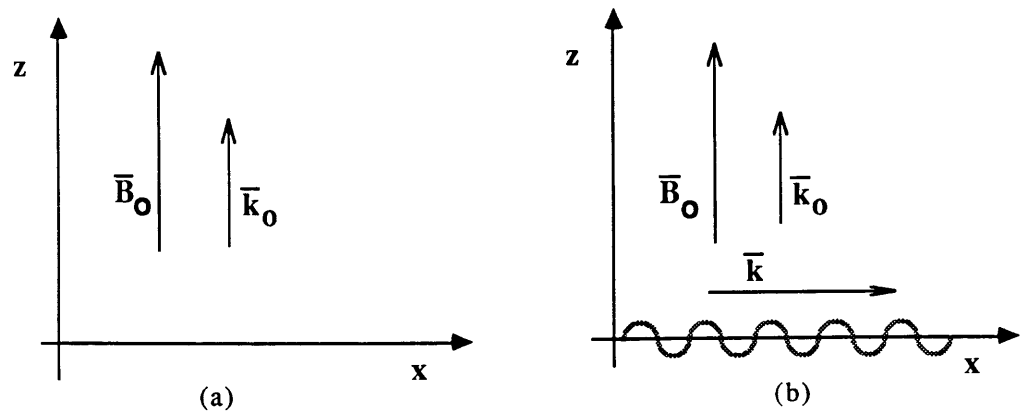

Figure 2-4: Coordinate system and wave vector geometry for (a) uniform ionosphere; (b) ionosphere with existing irregularities

pressed as

$$\delta \mathbf{j_s} = -e(N_o \delta \mathbf{v} + \frac{\delta n}{N_o} \mathbf{j_o}) \tag{2.6}$$

where $\delta \mathbf{v}$ is the induced velocity perturbation. The scattered wave field has the general form of

$$\mathbf{E_s} = [\hat{x} E_x + i\hat{y} E_y] \exp[i(k_o z - \omega_o t)] \tag{2.7}$$

Solving the wave equation together with the electron momentum equation, the scattered wave field is found to be elliptically polarized

$$\mathbf{E_s} = E_o(\delta n / N_o)[\hat{x} + (\hat{x} + i\hat{y}) E_s] \exp[i(k_o z - \omega_o t)] \tag{2.8}$$

E_s is the amplitude of the circularly polarized component of the wave given by

$$E_s = -\frac{2\omega_{pe}^2 \omega_o}{k^2 c^2 (\omega_o - \Omega_e)} \tag{2.9}$$

where ω_{pe} and c are the electron plasma frequency and the speed of light in vacuum, respectively, and k is the wavenumber of the density perturbation defined by (2.5). Writing the scattered field in terms of the ionospheric irregularity scale length, $\lambda =$

$2\pi/k$, we find

$$\mathbf{E_s} = E_o \exp[ikx](\delta\tilde{n}/N_o)[\underbrace{\hat{x}}_{LP} + \underbrace{(\hat{x} + i\hat{y})}_{CP}\frac{\lambda^2}{\lambda_c^2}]\exp[i(k_o z - \omega_o t)] \tag{2.10}$$

where,

$$\lambda_c = \sqrt{2}\pi(c/\omega_{pe})(\Omega_e/\omega_o)^{1/2} \approx 4.4/k_o \tag{2.11}$$

The scattered field is composed of a linearly polarized (LP) part and a circularly polarized (CP) part as indicated in (2.10). If the ratio $(\lambda^2/\lambda_c^2) \ll 1$ (i.e., $|\mathbf{k}| \gg |\mathbf{k_o}|$) the scattered wave is dominated by the linearly polarized component, which oscillates in the direction of the irregularity wavevector, $\mathbf{k}$; hence, the wave is electrostatic in nature and exhibits a broadened, enlarged wave vector spectrum relative to the incident wave. The Doppler shift frequency measured by a moving satellite will be enlarged as well.

Analysis

The condition found above for effective nonlinear scattering into quasi-electrostatic modes requires $\lambda^2/\lambda_c^2 \ll 1$. Typical plasma parameters for the upper ionosphere/lower magnetosphere region of interest are $\omega_{pe}/2\pi = 0.8$ MHz, $\Omega_e/2\pi = 0.6$ MHz. Using these values and assuming an incident frequency of $\omega_o/2\pi = 13.6$ kHz in equation (2.11), we calculate $\lambda_c \simeq 1.3$ km. The magnitude of the bandwidth expansion measured by a moving satellite due to the Doppler shift of the scattered VLF wave is

$$\Delta f = \frac{\mathbf{k_s} \cdot \mathbf{v_s}}{2\pi} \simeq \frac{v_s \cos\theta}{\lambda} \approx \frac{v_s}{\lambda} \tag{2.12}$$

where $\mathbf{v_s}$ is the velocity of a satellite moving across the earth's magnetic field as shown in Figure 2-5, and $\mathbf{k_s} = k\hat{x} + k_o\hat{z}$. For a typical satellite with velocity, $v_s \simeq 8$ km/sec, to observe a signal shifted by the observed amount of broadening, $\Delta f \simeq 100$ Hz, equation (2.12) requires density fluctuations of wavelength, $\lambda \simeq 80$ m. Comparing

this value with that found for λ_c above, we find $\lambda^2/\lambda_c^2 \approx 4\times10^{-3} \ll 1$, so the condition for nonlinear scattering is well satisfied.

Thus we have found that ionospheric irregularities with scale lengths of several tens of meters can produce Doppler shifts of the observed magnitude. The Doppler shift of a single mode does not in itself produce broadened spectra similar to those that have been observed. In practice, of course, the scale spectrum of existing irregularities is relatively broad, and nonlinear scattering can occur effectively over a wide range of wavelengths satisfying the condition found in (2.10). It is this spectrum of waves that the satellite encounters, recording a full range of Doppler shifted signals with the resulting spectrum appearing to have been smoothly broadened. This explanation predicts that the dominant spectral shape produced should be that of a broadened Gaussian distribution, similar to the Type 4 spectrum in Figure 2-3. These type spectra are, in fact, the ones most commonly observed [*H. G. James*, private communication, 1987].

Asymmetric spectra could also be generated by this mechanism when gradients in the scale size and/or amplitude of the density irregularities exist in either time or space. The satellite receives both forward scattered and back scattered waves. If the forward scattered waves have been scattered by shorter scale irregularities than the back scattered waves, for example, would lead to more broadening on the upshifted side of the spectrum. This could occur if the spectrum of density irregularities had a positive scale size gradient in the direction of the approaching satellite. A drift of the irregularities towards the receiving satellite could produce a similar effect. The sometimes observed suppression of the broadened spectrum at the carrier frequency, however, cannot be easily explained with the nonlinear scattering mechanism described here for physically realistic irregularity spectra. Ionospheric irregularities can occur naturally or be created by the incident VLF waves.

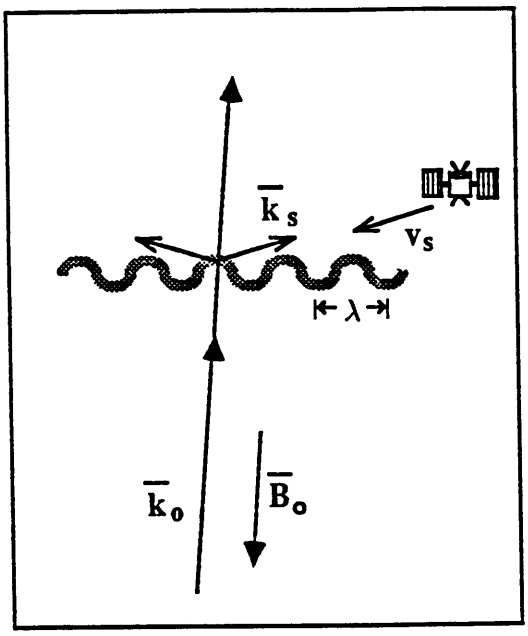

Figure 2-5: Satellite reception geometry leading to Doppler broadened spectra

Particle precipitation can produce irregularities with a broad range of scale lengths in a region near the F-layer peak, about 300 km above the earth's surface. However, the reduced phase speed of the scattered quasi-electrostatic wave leads to significant Landau damping of this wave mode, and the amplitude of such a wave decreases exponentially as it propagates upwards to satellite altitudes of 600–3800 km. Nevertheless, the required irregularities can be induced by intense VLF waves locally [*Lee and Kuo,* 1984]. Furthermore, these wave-induced irregularities possess a relatively narrow spectrum of scale lengths ranging from a few meters to a few tens of meters in the ionosphere, which might produce some of the more structured spectral types in Figure 2-3.

2.3 Summary and Conclusion

In summary, a possible source mechanism has been investigated that can be responsible for the observed spectral broadening of injected VLF waves. In the presence of ionospheric irregularities with scale lengths less than several tens of meters, the

nonlinear scattering of the relatively weak VLF waves off these density irregularities can produce quasi-electrostatic modes with larger wave vectors which give rise to the apparent spectral broadening through the Doppler shift observed by the moving satellite; the broadening produced through this mechanism is of the same magnitude as the observed values. The amplitude of the quasi-electrostatic modes depends linearly on the amplitude of the ionospheric irregularities. Possible sources of the field-aligned ionospheric irregularities include particle precipitation, various plasma instabilities, [see, e.g., *Bell, et al.*, 1983; *Providakes, et al.*, 1985; *Sudan, et al.*, 1973; *Farley*, 1963], or the VLF waves themselves [*Lee and Kuo*, 1984]. This mechanism can largely explain the observed spectral broadening of injected VLF waves reported by Bell, et al. [1983] and others. An experiment attempting to verify the validity of the mechanism is presented in Chapter 4.

Chapter 3

Irregularity Formation Induced by Powerful VLF Waves

The work presented here was motivated by the spectral broadening observations discussed in Chapter 2. Specifically, two parametric instabilities are investigated theoretically to explain observed spectral broadening features not easily accounted for with the nonlinear scattering mechanism, such as the carrier frequency suppression of some broadened spectra [*Bell et al.*, 1983].

In the first instability, reported by Lee and Kuo [1984], the injected VLF wave excites both upshifted and downshifted components of lower hybrid waves, concomitantly producing a field-aligned purely growing mode. *Lower hybrid* waves are electrostatic waves which propagate nearly perpendicular to the geomagnetic field, involving both electron and ion dynamics. The short scale length of the density irregularities produced by this process (few tens of meters) can nonlinearly scatter the incident VLF radiation and produce apparent spectral broadening as described in Chapter 2. Because the real frequency of the purely growing mode equals zero, the frequency of the excited lower hybrid waves matches that of the incident VLF waves. These lower hybrid waves, acting as pump waves, can then interact with low frequency thermal-

level density fluctuations, generating both backscattered and forwardscattered lower hybrid wave sidebands in the second instability, as shown by Kuo and Lee, [1986].

I have solved the dispersion relation and analyzed the characteristics of the second instability. The nonzero real frequency of the low frequency fluctuations corresponds to the carrier frequency offset experienced by the lower hybrid wave sidebands and a resulting decrease in wave power at the carrier frequency. In addition, the forwardscattered lower hybrid waves have a much smaller phase velocity than the parent waves enabling them to accelerate charged particles, potentially generating ionospheric density fluctuations and airglow. The wave electric field required to excite the second instability is about an order of magnitude larger than the threshold field of the first instability, varying from about 25 mvolts/m at altitudes above 1000 km to several volts/m below 800 km altitude.

The processes may be summarized as follows:

$$\text{Step 1)}\quad \text{VLF} \longrightarrow \text{LH}_{1\pm} + \text{Zero Frequency FA Mode}$$

$$\text{Step 2)}\quad \text{LH}_1 \longrightarrow \text{LH}_{2\pm} + \text{Low Frequency FA Mode}$$

where VLF, LH, and FA stand for Very Low Frequency wave, Lower Hybrid wave, and Field Aligned, respectively. The $+/-$ indicates that both upshifted and downshifted modes are produced.

3.1 Step 1: Parametric Excitation of Lower Hybrid Waves

In this section we discuss the first step of the mechanism believed to cause observable plasma density fluctuations; namely, parametric excitation of lower hybrid waves and ionospheric irregularities. Before proceeding with the derivation, however, it may be useful to review the basic theory of parametric processes presented in Appendix B.

3.1.1 Theory

As in the previously considered case of nonlinear scattering (Chapter 2), the incident wave is also assumed to be a ducted whistler mode with $\mathbf{k_o} = \mathrm{k_o}\hat{\mathbf{z}}$, propagating along the geomagnetic field lines, taken to be the z axis. Assuming the space-time dependence of the perturbations to be $\exp[\mathrm{i}(\mathbf{k_o}\cdot\mathbf{r}-\omega\mathrm{t})]$, the first physical process of [VLF $\longrightarrow$ $\mathrm{LH}_{1\pm}$ + Zero Frequency FA Mode] can be described by the following wave frequency and wave vector matching relations:

$$\begin{aligned} \omega_{1+} - \omega_s &= \omega_o = \omega_{1-} + \omega_s^* \\ \mathbf{k_{1+}} - \mathbf{k_s} &= \hat{\mathbf{z}}\mathrm{k_o} = \mathbf{k_{1-}} + \mathbf{k_s} \end{aligned} \tag{3.1}$$

where the subscripts $-/+$ and s refer to the Stokes/anti-Stokes components of the high frequency lower hybrid sidebands and the field-aligned zero frequency mode, respectively. Choosing the x axis to coincide with the wave vector, $\mathbf{k_s}$, of the field-aligned modes, as shown in Figure 3-1a, and expressing the frequency $\omega_s = i\gamma$ ($Re[\omega_s] = 0$), the matching conditions (3.1) may be represented by

$$\begin{aligned} \omega_{1\pm} &= \omega_o + i\gamma \\ \mathbf{k_{1\pm}} &= \hat{\mathbf{z}}\mathrm{k_o} \pm \hat{\mathbf{x}}\mathrm{k_s} \end{aligned} \tag{3.2}$$

This process has been investigated in detail in *Lee and Kuo*, [1984]. For the upper ionosphere in the frequency range of interest, the nonoscillatory current resulting from the beating of the density fluctuations associated with the lower hybrid waves and the electron response to the whistler pump field is found to be the dominant nonlinear effect. The threshold electric field is of the order of 1 mvolt/m, which can be exceeded by the powerful ground based transmitters used in the observational studies of spectral broadening. The scale lengths of the zero frequency modes are found to be a few tens of meters.

3.2 Step 2: Stimulated Scattering of Lower Hybrid Waves

The lower hybrid waves generated by the first process, with wave vector and wave frequency denoted by $\mathbf{k_1}$, ω_1, respectively, can act as pump waves to produce high frequency lower hybrid sidebands ($\mathbf{k_2}, \omega_2$), and low frequency field-aligned modes ($\mathbf{k_s}, \omega_s$; $Re[\omega_s] \ll \omega_1$) via the second parametric instability [*Kuo and Lee*, 1986],

$$\begin{aligned} \omega_{2+} - \omega_s &= \omega_1 = \omega_{2-} + \omega_s^* \\ \mathbf{k_{2\pm}} &= \mathbf{k_1} \pm \mathbf{k_s} \end{aligned} \tag{3.3}$$

where the subscripts $+/-$ refer to the anti- Stokes/Stokes components of the lower hybrid sidebands. The wave vector matching relation for this step is illustrated graphically in Figure 3-1b. The Stokes component of the sidebands may be chosen as an eigenmode of the plasma by setting $\mathbf{k_s} = 2\mathbf{k_1}$, which minimizes the threshold of the instability. While the backscattered sideband mode has the same scale length as the pump wave, that of the forward scattered sideband mode is one-third of the pump wavelength. The dispersion relation obeyed by the LH pump wave is given by,

$$\omega_1 = \omega_{lh}[1 + (m_i k_{1z}/m_e k_1)]^{1/2} \tag{3.4}$$

where

$$\omega_{lh} = \frac{(\omega_{pi}^2 + k_1^2 v_{ti}^2)^{1/2}}{(1 + \omega_{pe}^2/\Omega_e^2)^{1/2}} \tag{3.5}$$

is the lower hybrid resonance frequency.

The plasma dynamics under consideration are determined by the momentum equation,

$$m_j n_j (\partial/\partial t + \mathbf{v_j} \cdot \nabla)\mathbf{v_j} = n_j q_j (\mathbf{E} + \mathbf{v_j} \times \mathbf{B_o}) - \nabla T_j n_j \tag{3.6}$$

the equation of continuity,

$$(\partial/\partial t) n_j + \nabla \cdot n_j \mathbf{v_j} = 0 \tag{3.7}$$

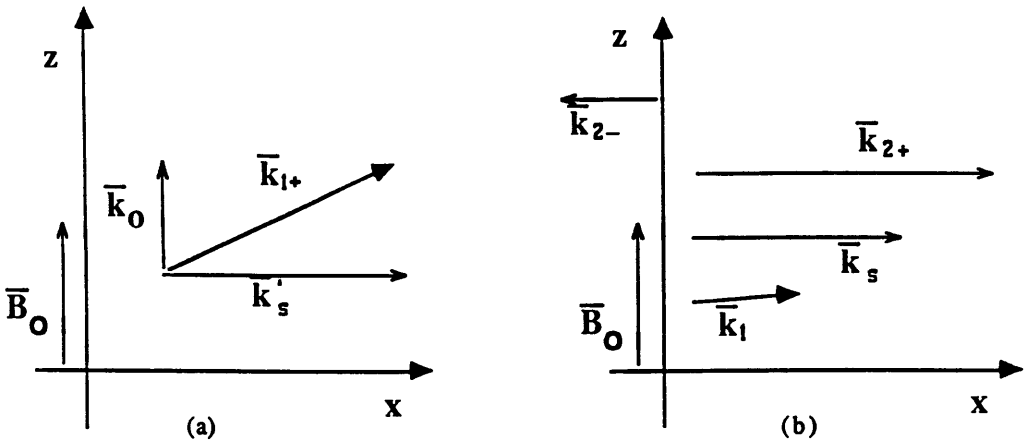

Figure 3-1: Graphical representation of wave vector matching condition for (A) Step 1 and (B) Step 2 of the VLF driven parametric instability.

and, in the case of low frequency oscillations, the quasi-neutrality condition,

$$n_i \approx n_e = n_o \tag{3.8}$$

where n, q, and T represent particle density, charge, and temperature in units of energy. The subscript j refers to the particle species; i for O^+ ions and e for electrons, as written explicitly in (3.8). Wavelike perturbations are assumed, having the form $\delta n_1, \mathbf{v_1} \sim \exp[i(\mathbf{k_1} \cdot \mathbf{r} - \omega_1 t)]$; $n_s, \mathbf{v_s} \sim \exp[i(\mathbf{k_s} \cdot \mathbf{r} - \omega_s t)]$; and $\delta n_\pm, \mathbf{v_\pm} \sim \exp[i(\mathbf{k_{2\pm}} \cdot \mathbf{r} - \omega_{2\pm} t)]$ where $\mathbf{k_{2\pm}}$ and $\omega_{2\pm}$ are defined by (3.3). Under the electrostatic approximation we may also express the electric field, E, as the gradient of a potential function, ϕ.

The beating interaction of the LH pump wave with the LH sidebands drives the low frequency field-aligned modes; the corresponding momentum equation is,

$$\omega_s m_j v_{sj} = i q_j / n_o (\mathbf{v_{sj}} \times \mathbf{B_o}) + \mathbf{k_s} T_j (n_s / n_o) + i \mathbf{F_j} \tag{3.9}$$

where $\mathbf{F_j}$, the ponderomotive force arises in the convective derivative as the first order velocity products which beat at a frequency difference, $|\omega_1 - \omega_2| \equiv \omega_s$. This force

is equivalent to the radiation pressure in the plasma due to the presence of the high frequency lower hybrid waves. $\mathbf{F_j}$ has the form

$$\mathbf{F_j} = -\mathrm{im_j}[\mathbf{k_1}\cdot(\mathbf{v^*_{j-}v_{j1}} - \mathbf{v_{j+}v^*_{j1}}) + \mathbf{k_+}\cdot\mathbf{v^*_{j1}v_{j+}} - \mathbf{k_-}\cdot\mathbf{v_{j1}v^*_{j-}}] \tag{3.10}$$

Applying (3.8) to the equation of continuity, we obtain

$$\omega_s(\mathrm{n_s/n_o}) = \mathbf{k_s}\cdot(\mathbf{v_{se}} + \mathbf{v^{nl}_e}) = \mathbf{k_s}\cdot(\mathbf{v_{si}} + \mathbf{v^{nl}_i}) \tag{3.11}$$

where the induced electron and ion nonoscillatory beating currents are defined by

$$n_o\mathbf{v^{nl}_j} = \delta n^*_{j1}\mathbf{v_{j+}} + \delta n_{j1}\mathbf{v^*_{j-}} + \delta n_{j+}\mathbf{v^*_{j1}} + \delta n^*_{j-}\mathbf{v_{j1}} \tag{3.12}$$

The velocity responses of the electrons and ions to the lower hybrid wave fields in (3.12) may be found by solving the linearized momentum equations for both species; the results are

$$\begin{aligned}\mathbf{v_{e1,\pm}} &= -ik_{1,\pm} \times[\hat{\mathbf{x}} + \mathrm{i}\hat{\mathbf{y}}(\omega_{1,\pm}/\Omega_\mathrm{e}) - \mathrm{i}\hat{\mathbf{z}}(\mathrm{k_{1z}}\Omega_\mathrm{e}/\mathrm{k_{1_\perp}}\omega_{1,\pm})] \\ &\quad \times[(\mathrm{e}\phi_{1,\pm}/\mathrm{m_e}\Omega_\mathrm{e}) - (\mathrm{v^2_{te}}\delta\mathrm{n_{e1,\pm}}/\mathrm{n_o}\Omega_\mathrm{e})] \qquad (3.13)\\ \mathbf{v_{i1,\pm}} &= ik_{1,\pm} \times[\hat{\mathbf{x}}(\Omega_\mathrm{i}/\omega_{1,\pm} - \mathrm{i}\hat{\mathbf{y}} - \mathrm{i}\hat{\mathbf{z}}(\mathrm{k_{1z}/k_{1_\perp}})] \\ &\quad \times[(\mathrm{e}\phi_{1,\pm}/\mathrm{m_i}\omega_{1,\pm}) - (\mathrm{v^2_{ti}}\delta\mathrm{n_{i1,\pm}}/\mathrm{n_o}\omega_{1,\pm})] \qquad (3.14)\end{aligned}$$

The equation of continuity can then be linearized and solved for the corresponding density perturbations,

$$\begin{aligned}\delta\mathrm{n_{e1,\pm}} &= (\mathrm{n_o e/m_e}\Omega^2_\mathrm{e})\mathrm{k^2_{1,\pm\perp}}\{(1 - \mathrm{k^2_{1z}}\Omega^2_\mathrm{e}/\mathrm{k^2_{1_\perp}}\omega^2_{1,\pm})\phi_{1,\pm} \\ &\quad +\delta_{\mathrm{o},\pm}(\mathrm{k_{1_\perp}/k_{\pm\perp}})(\omega_1/\omega_\pm)(1 - \mathrm{k^2_{o1}}\Omega^2_\mathrm{e}/\mathrm{k^2_{1_\perp}}\omega^2_1) \\ &\quad \times(1 + \mathrm{k_1}\omega_{\mathrm{s}_\pm}/\mathrm{k_s}\omega_1)[1 + (\mathrm{k^2_{1_\perp}v^2_{te}}/\Omega^2_\mathrm{e})(1 - \mathrm{k^2_{1z}}\Omega^2_\mathrm{e}/\mathrm{k^2_{1_\perp}}\omega^2_1)] \\ &\quad \times\phi_1(\mathrm{n_{s_\pm}/n_o})\}[1 + (\mathrm{k^2_{1,\pm\perp}v^2_{te}}/\Omega^2_\mathrm{e})(1 - \mathrm{k^2_{1z}}\Omega^2_\mathrm{e}/\mathrm{k^2_{1_\perp}}\omega_{1,\pm})]^{-1} \qquad (3.15)\\ \delta\mathrm{n_{i1,\pm}} &= (\mathrm{n_o e/m_i}\omega_{1,\pm^2})\mathrm{k^2_{1,\pm\perp}}[\phi_{1,\pm} + \delta_{\mathrm{o},\pm}(\mathrm{k_1/k_\pm})(\omega_\pm/\omega_1) \\ &\quad \times(1 + \mathrm{k_1}\omega_{\mathrm{s}_\pm}/\mathrm{k_s}\omega_1)(1 - \mathrm{k^2_1v^2_{ti}}/\omega^2_1)\phi_1(\mathrm{n_{s_\pm}/n_o})] \\ &\quad \times(1 - \mathrm{k^2_{1,\pm\perp}v^2_{ti}}/\omega^2_{1,\pm})^{-1} \qquad (3.16)\end{aligned}$$

where $\delta_o = 0$ and $\delta_\pm = 1$. From Poisson's equation, $k_\pm^2 \phi_\pm = 4\pi e \delta n_{i_\pm} - \delta n_{e_\pm}$, together with the continuity equations and the momentum equations of electrons and ions, we can derive the coupled mode equation for the excited LH sideband modes as follows:

$$\begin{aligned} \phi_\pm &= l_\pm (k_1/k_\pm)(\omega_1/\omega_\pm)(\omega_\pm^2 - k_\pm^2 v_{ti}^2) \\ &\quad \times (1 - k_{\pm z}^2 v_{te}^2/\omega_\pm^2 + k_\pm^2 v_{te}^2/\Omega_e^2) \\ &\quad \times (1 + k_1 \omega_{s_\pm}/k_s \omega_1)\phi_1 (n_{s_\pm}/n_o) \end{aligned} \tag{3.17}$$

where

$$\begin{aligned} l_\pm &= \Big((\omega_\pm^2 - \omega_1^2)(1 + \omega_{pe}^2/\Omega_{pe}^2) - (k_\pm^2 - k_1^2) \\ &\quad \times \{1 + \omega_{pe}^2/\Omega_{pe}^2 + [\omega_{pe}^2 + (k_1^2 + k_\pm^2)v_{te}^2] \\ &\quad \times (1 - k_{1z}^2 \Omega_e^2/k_1^2 \omega_\pm^2)/\Omega_e^2\} v_{ti}^2\Big)^{-1} \end{aligned}$$

The LH sideband modes are driven by the beating current induced by the LH pump wave field on the density perturbation associated with the low-frequency mode. The low-frequency mode, by contrast, is found to be driven primarily by ion nonlinearity, including the ponderomotive force and the low-frequency beating current. While the ponderomotive force acts as the driving source, the beating current imposes a stabilization effect on the instability.

Substituting the first-order perturbations given in (3.13)–(3.15) and solving (3.9)–(3.12) together with (3.17), we obtain the following dispersion relation

$$a\omega_s^3 + b\omega_s^2 - c\omega_s + d = 0 \tag{3.18}$$

where

$$\begin{aligned} a &= 2\Lambda (k_1 k_s v_{ti}^2/k_{sz}^2 C_s^2)[(1 + k_s^2 C_s^2/\Omega_i^2)/\omega_1 (1 + \omega_{pe}^2/\Omega_e^2)] \\ b &= 1 + \Lambda^2 (1 + k_s^2 C_s^2/\Omega_i^2) k_1^2 (k_s^2 - 4k_1^2) v_{ti}^4/k_{1z}^2 C_s^2 \omega_1^2 (1 + \omega_{pe}^2/\Omega_e^2)^2 \\ c &= [k_{sz}^2 C_s^2/(1 + k_s^2 C_s^2/\Omega_i^2]a \end{aligned}$$

$$
\begin{aligned}
\mathrm{d} &= \tfrac{1}{2}\Lambda[(\mathrm{v}_{\mathrm{ti}}^2/\mathrm{C}_\mathrm{s}^2)/\omega_1^2(1+\omega_{\mathrm{pe}}^2/\Omega_\mathrm{e}^2)^2](\mathrm{k}_\mathrm{s}^2\mathrm{v}_{\phi\mathrm{i}}^2\omega_1^2\{[\eta/\alpha(1-\mathrm{k}_1^2\mathrm{v}_{\mathrm{ti}}^2/\omega_1^2) \\
&\quad -\alpha(\omega_1^2-\mathrm{k}_1^2\mathrm{v}_{\mathrm{ti}}^2)/\Omega_\mathrm{e}\Omega_\mathrm{i}] + 4\eta(\mathrm{k}_1^2\mathrm{v}_{\mathrm{te}}^2/\Omega_\mathrm{e}^2)(\mathrm{k}_\mathrm{s}-2\mathrm{k}_1)/\mathrm{k}_\mathrm{s}(1-\mathrm{k}_1^2\mathrm{v}_{\mathrm{ti}}^2/\omega_1^2)\} \\
&\quad -\tfrac{1}{2}\Lambda\mathrm{k}_\mathrm{s}^2(\mathrm{k}_\mathrm{s}^2-4\mathrm{k}_1^2)\mathrm{C}_\mathrm{s}^2\mathrm{v}_{\mathrm{ti}}^2) \\
\Lambda &= 1+\omega_{\mathrm{pe}}^2/\Omega_\mathrm{e}^2+\eta(\omega_{\mathrm{pe}}^2+10\mathrm{k}_1^2\mathrm{v}_{\mathrm{te}}^2)/\Omega_\mathrm{e}^2 \qquad (3.19) \\
\eta &= 1-\mathrm{k}_{1\mathrm{z}}^2\Omega_\mathrm{e}^2/\mathrm{k}_1^2\omega_1^2 \\
\alpha &= \eta/(1-\mathrm{k}_{1\mathrm{z}}^2\mathrm{v}_{\mathrm{te}}^2/\omega_1^2+\mathrm{k}_1^2\mathrm{v}_{\mathrm{te}}^2/\Omega_\mathrm{e}^2) \\
\mathrm{v}_{\mathrm{te}}^2 &= 3\mathrm{T}_\mathrm{e}/\mathrm{m}_\mathrm{e} \\
\mathrm{v}_{\mathrm{ti}}^2 &= 3\mathrm{T}_\mathrm{i}/\mathrm{m}_\mathrm{i}
\end{aligned}
$$

Substituting $\omega_s = \omega_r + i\gamma$ into (3.18), two equations for the growth rate, γ, and the real frequency, ω_r, are obtained,

$$\gamma^2 = [d/(b+2a\omega_r)] - \omega_r^2 \qquad (3.20)$$

$$(b+2a\omega_r)^3 - b(b+2a\omega_r)^2 - ac(b+2a\omega_r) - a^2d = 0 \qquad (3.21)$$

Setting $\gamma = 0$ to determine the threshold of the instability, (3.20) and (3.21) may be solved for the coefficient, d, giving

$$d = 2a\{[(b/3a)^2+c/3a][(b/3a)^2+c/3a]^{1/2} - [(b/3a)^3+bc/6a^2]\} \qquad (3.22)$$

Equating this result with the expression in (3.19), we find the threshold condition of the instability requires

$$v_{\phi i}^2 \geq v_{thi}^2 \simeq \{\tfrac{4}{3}(\mathrm{k}_{\mathrm{sz}}\mathrm{C}_\mathrm{s}/\omega_1)(2\mathrm{k}_1/\mathrm{k}_\mathrm{s})(1+\omega_{\mathrm{pe}}^2/\Omega_\mathrm{e}^2) \qquad (3.23)$$

$$\times[(1+h)^{3/2} - \tfrac{3}{2}\mathrm{h}^{1/2}(1+2\mathrm{h}/3)]/[3(1+\mathrm{k}_\mathrm{s}^2\mathrm{C}_\mathrm{s}^2/\Omega_\mathrm{i}^2)]^{\frac{1}{2}}\}\mathrm{C}_\mathrm{s}^2 \times [\eta/\alpha - \alpha\omega_1^2/\Omega_\mathrm{e}\Omega_\mathrm{i}]^{-1} \qquad (3.24)$$

where $\mathrm{v}_{\phi\mathrm{i}} = \mathrm{eE}_1/\mathrm{m}_\mathrm{i}\omega_1$ is the ion quiver velocity, $\mathrm{h} = \mathrm{b}^2/3\mathrm{ac}$, and $\mathrm{C}_\mathrm{s} = [(\mathrm{T}_\mathrm{e}+\mathrm{T}_\mathrm{i})/\mathrm{m}_\mathrm{i}]^{1/2}$ is the acoustic speed in the ionospheric plasma. When the lower hybrid pump field strength is sufficient to produce quiver velocities in excess of that required by (3.24), positive growth rates for the instability occur.

Characteristics of the Instability

This mechanism has been analyzed for typical plasma parameters in the topside ionosphere in two different altitude regimes. The first region (Region I) investigated is the atmosphere at or above 1000 km where H^+ is the dominant ion species and densities are relatively low. The specific plasma parameters used are $\omega_{pe}/2\pi = 0.65MHz$; $\Omega_e/2\pi = 0.55MHz$; $\omega_{pi}/2\pi = 15KHz$; $\Omega_i/2\pi = 330Hz$; $m/M_i(H^+) = 5.45 \times 10^{-4}$; $T_e = T_i = 1000°K$. The analysis was carried out in the spectral range about $\mathbf{k_s} \approx 2\mathbf{k_o}$, consistent with previous assumptions.

Illustrated in Figure 3-2 is the spectral dependence of both the growth rate of the instability and the real frequency of the low-frequency field-aligned mode. The real frequency of this mode corresponds to the magnitude of the lower hybrid wave frequency offset from the VLF carrier frequency. The curves in Figure 3-2 were calculated by solving the complete dispersion relation for the instability, (3.20) and (3.21), assuming an electron quiver velocity, $v_{\phi e} \simeq v_{\phi i}(\omega_o/\Omega_i) = C_s$. The electric field required to achieve this quiver velocity is about 25 $m$volts/m. The growth rate, γ, goes to zero near -2ϵ, because the required threshold electron quiver velocity exceeds C_s at this point.

As can be seen in Figure 3-2a, the growth time of the instability is about 100 ms; for pulse lengths of the order of one second, significant growth can occur. The growth rate and spectral range of the instability increase linearly with the pump power as $v_{\phi e} \geq C_s/\sqrt{2}$. This is illustrated in Figure 3-2b, where larger values of $v_{\phi e}$ were assumed. The calculated magnitude of the real frequency shift exhibits a much weaker dependence on the pump wave intensity, increasing by a factor of two for an order of magnitude increase in the electric field strength of the LH pump wave.

The second altitude regime investigated includes the topside ionosphere between 500–750 km (Region II). Here the plasma is dominated by O^+ ions, and the plasma

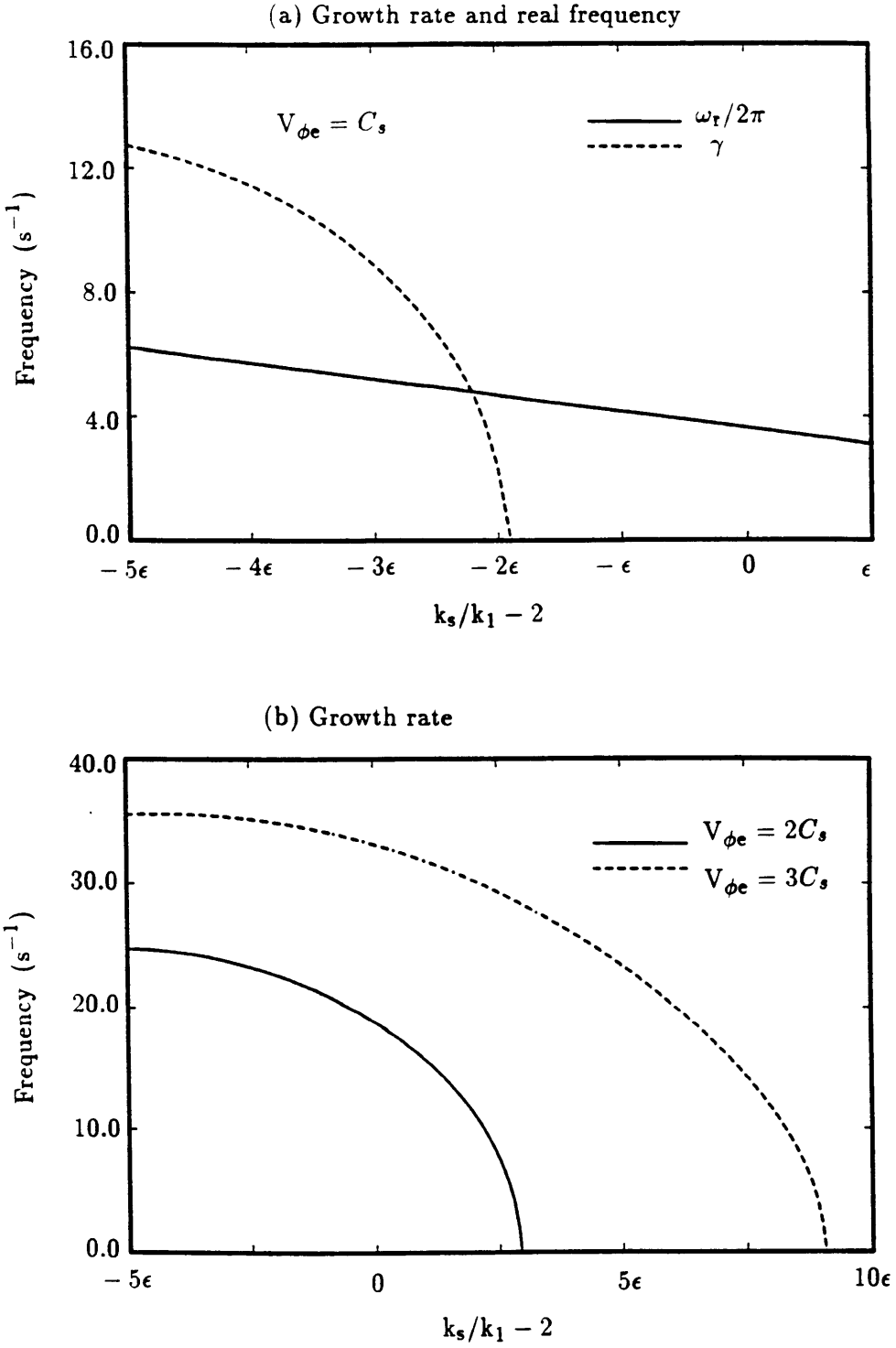

Figure 3-2: (a) Spectral dependence of the growth rate, γ, and the real frequency in Region I. (b) Spectral dependence of the growth rate for two different values of $V_{\phi e}$ ($\epsilon = 10^{-2}$).

densities are considerably higher. The parameters used are $\omega_{pe}/2\pi = 2.8MHz$; $\Omega_e/2\pi = 0.84MHz$; $\omega_{pi}/2\pi = 16.5KHz$; $\Omega_i/2\pi = 30Hz$; $m/M_i(O^+) = 3.41 \times 10^{-5}$; $T_e = T_i = 1000°K$.

The maximum growth rate as a function of electric field strength is plotted in Figure 3-3. Much larger fields are required to achieve growth rates comparable to those found in Region I, where the electric field required for the maximum growth rate, $v_{\phi e} = 3C_s$, case is still less than 1 v/m. Physically, there are two primary factors responsible for the differences in the instability requirements in the two regions.

The first is the transition from H^+ plasma to O^+ plasma as one moves from Region I to Region II. Relatively weak electric fields are needed to accelerate the light H^+ ions supporting the excited waves in Region I; the electric field must be stronger in Region II in order to induce a comparable velocity response in the dominant O^+ ions, which are 16 times more massive.

The second factor increasing the instability threshold in Region II is the higher plasma density. More energy is required to excite the waves in Region II simply because the energy density is greater there. The same energy input at two different levels in the atmosphere invokes a much greater response in the medium at the higher altitude, as is well known from gravity wave theory where the wave amplitude grows exponentially with increasing height to maintain constant energy density.

3.3 Summary of Parametric Instability

We have examined two parametric instabilities which draw energy from an electromagnetic VLF pump wave and excites electrostatic lower hybrid waves and low frequency modes in the ionosphere. The first instability can induce spectral broadening by creating short scale (few tens of meters) density irregularities able to nonlinearly scatter VLF waves when the wave amplitude exceeds a few mvolts/m. The second

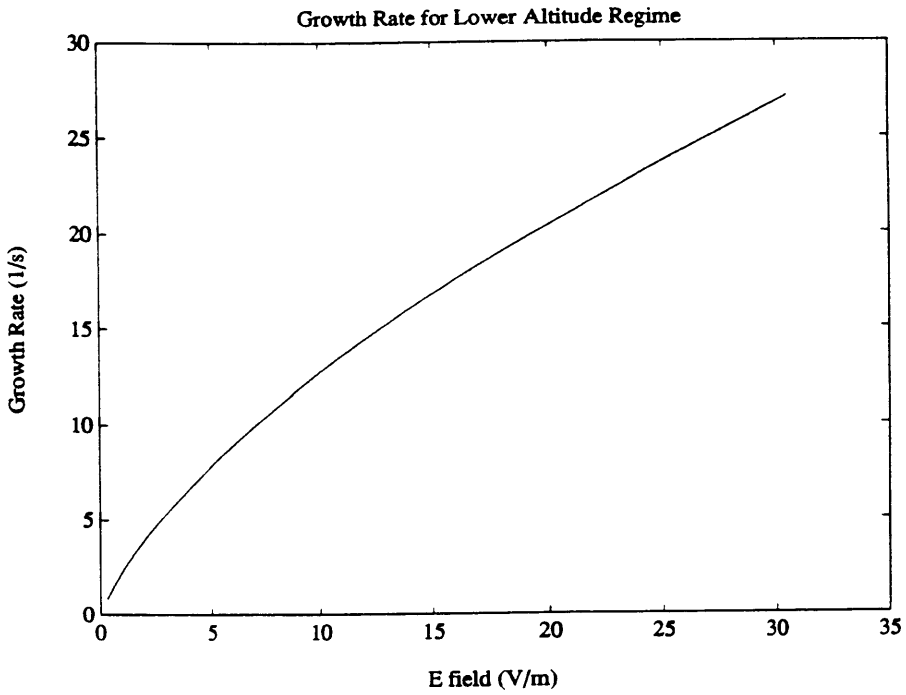

Figure 3-3: Maximum growth rate of the instability as a function of electric field strength in Region II.

instability excites lower hybrid sidebands with a nonzero frequency offset, resulting in a decrease in wave power at the carrier frequency, as has been reported in some spectral broadening observations [*Bell et al.*, 1983]. The electric field threshold of the instability, however, is at least 25 mvolts/m in the ionosphere above 1000 km, which can not be exceeded easily by ground-based VLF transmitters. Thus, this mechanism is not considered a primary candidate to explain some observed spectral broadening events.

The forwardscattered (upshifted) lower hybrid wave excited in the second instability has a phase velocity equal to one third the phase velocity of the parent waves, and the parallel (perpendicular) component is within an order of magnitude of the electron (ion) thermal velocity. Thus, the upshifted LH wave may accelerate bulk electrons and ions along and across the geomagnetic field lines, respectively. The acceleration of the charged particles is important because it induces observable density fluctuations in the space plasma and enhances airglow through impact excitations

with neutral particles.

These processes can only occur if the VLF pump wave amplitude exceeds a threshold value which varies inversely with altitude. At a given altitude, the growth rate increases essentially linearly with the pump wave field strength. Unlike the nonlinear scattering examined in Chapter 2 which required pre-existing irregularities, the instability analyzed here predicts that VLF waves, if sufficiently intense (see Figures 3-2 and 3-3), can potentially stimulate the growth of irregularities from thermal-level fluctuations. Attempts to test this result experimentally with the ACTIVE satellite are presented in the next chapter.

Chapter 4

The ACTIVE Satellite Experiments: Testing Nonlinear VLF Interaction Theories

In June, 1989, a NASA Research Announcement (NRA–89–OSSA–11) described a new research program consisting of joint cooperation with the Soviet Union in conducting active space plasma experiments with a new Soviet intercosmos satellite, ACTIVE. The 10 kW VLF transmitter on board the satellite promised to be an excellent device for testing the hypotheses of VLF interactions with ionospheric plasmas developed in Chapters 2 and 3.

The intensity of the VLF radiation in the vicinity of the satellite was expected to exceed parametric instability thresholds, and incoherent scatter radars at Millstone Hill and Arecibo Observatory were employed to diagnose this region for evidence of VLF-induced density fluctuations. The results of these experiments are inconclusive because the onboard VLF transmitter failed to operate properly.

4.1 The ACTIVE Program

The satellite was equipped with several instruments capable of actively modifying the surrounding space plasma environment, including a powerful (10 kW) VLF transmitter (10 kHz), a plasma beam instrument, and a Xenon neutral gas release device. A full diagnostic instrument package provided information on plasma parameters and electric and magnetic fields. A portion of these instruments was placed aboard a subsatellite, CZAK, to be deployed from the main satellite after an appropriate orbit had been established.

After being launched in September, 1989, the satellite was placed in an elliptical, high inclination orbit with a perigee of 500 km and an apogee of 2500 km (see Figures 4-1 and 4-2). We planned a series of experiments to investigate the effects of powerful VLF waves on the space plasma; because ground-based incoherent scatter (IS) radar was to be the primary diagnostic for the VLF wave effects, perigee passes over the radar sites were chosen to minimize the distance between the perturbed region and the radar. The latitude of perigee for ACTIVE changed by a little more than 2° per day, meaning that approximately every 90 days the point of perigee would return to the same latitude.

Because of the limited field of view of the UHF radar (±20° zenith angle), observations at the Arecibo Observatory were limited to 1–2 good passes occurring during a two week period every three months. The full steerability of the Millstone Hill IS radar (MISA) allowed greater flexibility in selecting passes for near observations from that site (see Figure 4-3). The characteristics of the Millstone Hill and Arecibo radars, as well as those of two other incoherent radar sites utilized in this thesis, are provided in Table 4.1. VLF transmission experiments were conducted at both Arecibo and Millstone Hill in late December 1989, and mid March and late May, 1990. The aim and design of these experiments is explained below.

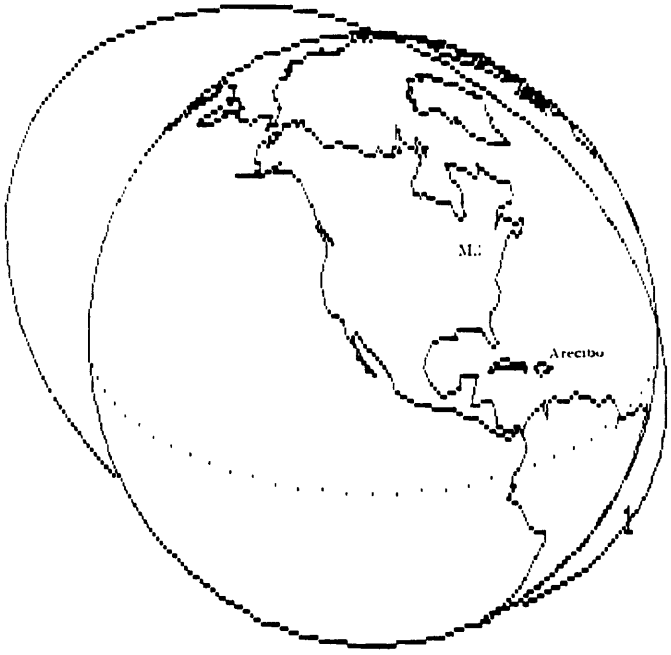

Figure 4-1: ACTIVE's eccentric orbit viewed from space; period is about 116 minutes.

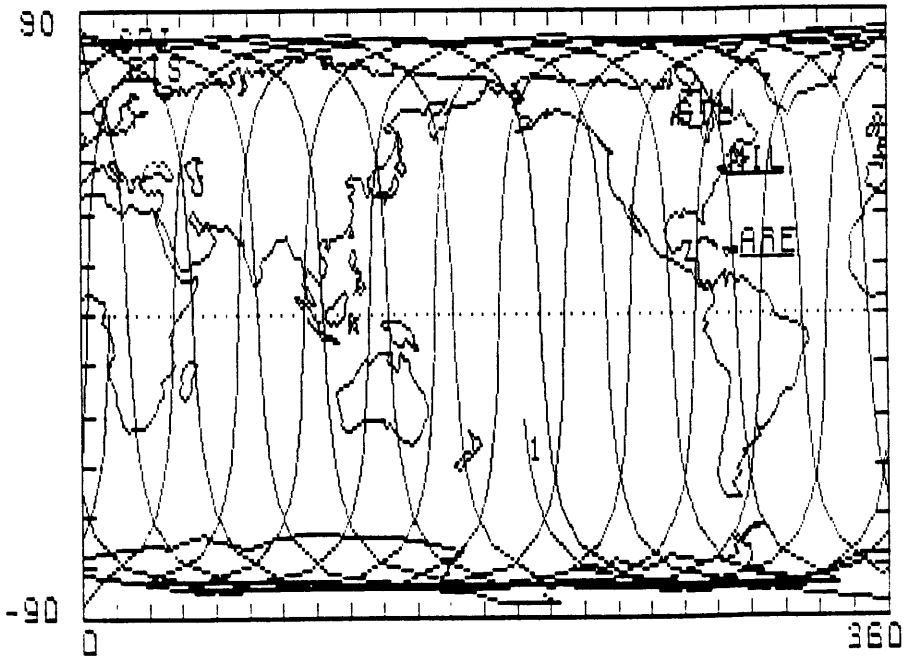

Figure 4-2: Flat map view of ACTIVE's groundtrack over a typical 24 hour period. Despite apparently good coverage, perigee passes over Arecibo were rare.

Table 4.1: Basic operating parameters of four incoherent radar sites

Site	Geo. lat	Geo. lon	Inv. lat	Freq. (MHz)	Dish diam. (m)	Peak Pwr. (MW)	Gain (dB)
Arecibo	18.3	293.2	30	430	270	1.5	61
Millstone	42.6	288.5	53	440	46	4.0	46
Sondreström	67.0	309.0	74	1290	34	4.0	50
Tromsø	69.6	19.2	66	933	32	1.6	48

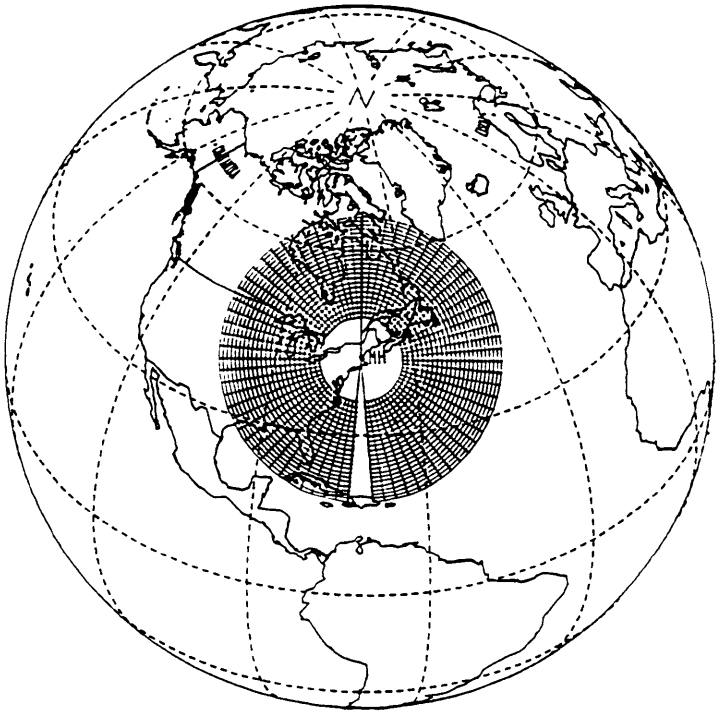

Figure 4-3: The F region field of view of the Millstone Hill radar; ACTIVE overflight experiments could be supported anywhere within the 2000 km radius shown

Table 4.2: VLF Wave–related mechanisms producing enhanced UHF radar backscatter.

No.	Mechanism	Physical Observable
1	Intense nonlinear near field interactions	Enhanced UHF backscatter in satellite vicinity ($r \leq 10$ km); airglow
2	VLF Wave–induced electron precipitation	Increased ionization in the D and E region; airglow
3	Two-step parametric instability	Growth of irregularities along VLF wave path (flux tube); airglow
4	Nonlinear mode coupling of VLF and existing irregularities	Spectral broadening measured by subsatellite; airglow

4.1.1 Experimental Objectives

The first step in developing the experimental plan consisted of identifying those effects which would be potentially observable with the IS radar from the ground and available in-situ diagnostics. The possible observable effects induced by the transmission of VLF waves in the ionosphere were thought to be caused by at least four distinct source mechanisms.

The least understood, but believed most intense effects were expected from turbulence-induced coherent structures in the strong near field ($r \leq 10$ km) of the VLF loop antenna [*USSR Space Research Institute Report*, 1987]. Resonant VLF wave–electron interactions in the far field, causing particle precipitation and subsequent enhanced ionization at lower altitudes constitute a second source of potential observable effects [*Inan, et al.*, 1982; *Koons, et al.*, 1981]. A third source mechanism produces an amplification of the thermal–level electron density fluctuations through parametric instabilities described in Chapter 3. Finally, the intensification of pre-existing irregularities through the nonlinear VLF wave mode coupling elucidated in Chapter 2 was believed to provide a fourth source of detectable radar backscatter and observable spectral broadening. The characteristics of these mechanisms are summarized in Table 4.2.

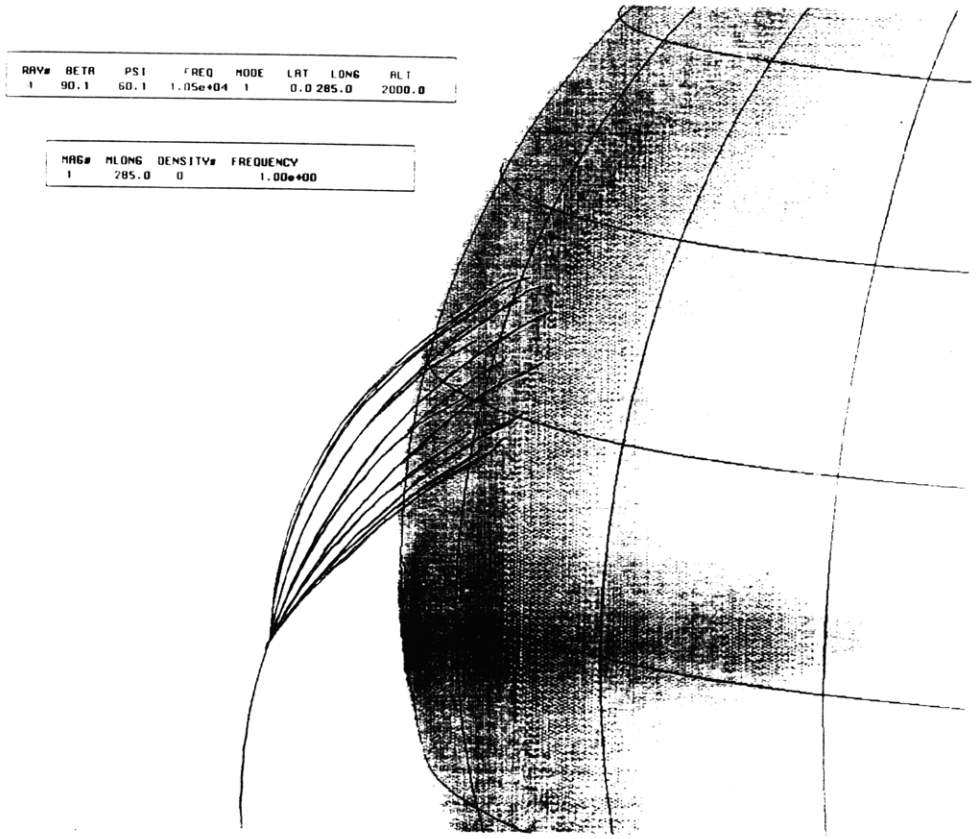

Figure 4-4: Radiation emission cone for 10 kHz ACTIVE transmission from 2000 km altitude to the surface. [after Green, 1990]

4.1.2 Arecibo Experiments Description

Assuming the VLF waves propagate in the far field as ducted whistler modes constrained by geomagnetic field lines, their induced effects will be limited to the magnetic flux tube of the waves' origin. The validity of this assumption can be seen from an examination of the results of VLF ray tracing studies presented in Figures 4-4 and 4-5. Figure 4-4 shows the expansion of the VLF radiation zone along the earth's magnetic field as the waves propagate from the satellite to the ground. While the waves cross magnetic field lines to some extent ($\approx 20°$ cone), close to the source ($r < 500$ km) the spreading effect is minimal. Figure 4-5 shows the emission cone of VLF radiation from ACTIVE at 1000 km altitude over Arecibo mapped to the ground. The wave amplitude is greatest at the center of the emission cone.

The constraint imposed by the ducted propagation assumption, coupled with the

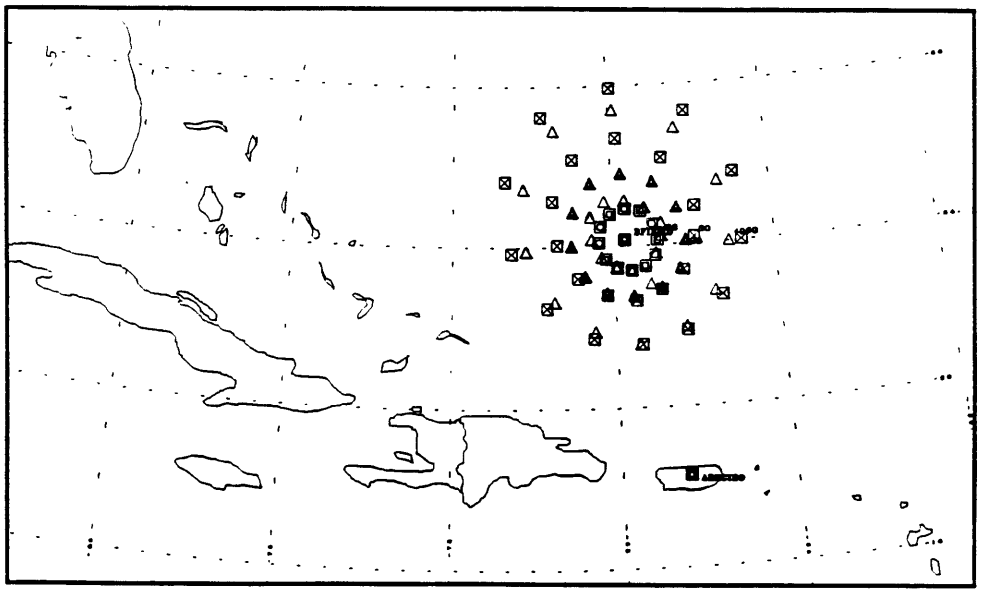

Figure 4-5: Footprint of 10 kHz ACTIVE transmission from 1000 km altitude over Arecibo [after Green, 1990]

knowledge of the source mechanisms in Table 4.2, led to the design of the Arecibo experiments depicted graphically in Figures 4-6 and 4-7. Ideally, both near and far field effects would map into the radar beam volume at different altitudes during a single satellite pass; i.e., waves radiated at latitudes south of Arecibo can propagate down the magnetic field lines (dip angle = 45°) to lower altitudes above the UHF radar. These waves constitute a far field VLF energy source; near field effects are evident during the satellite's passage through the radar beam in the "direct look" experiments. Irregularities created by the HF heater at Arecibo were used as a source for nonlinear scattering of the VLF waves in the far field. Comparing stationary ground based VLF measurements with those obtained on board the moving CZAK subsatellite provides an important test of the results of Chapter 2 (see Figure 4-7).

We conducted a total of four direct look experiments at Arecibo from late December, 1989 to late May, 1990. Specific dates and some of the relevant radar parameters used in making these measurements are summarized in Table 4.3. The slow scan rate of the Arecibo UHF radar required that the beam be parked in a position and kept

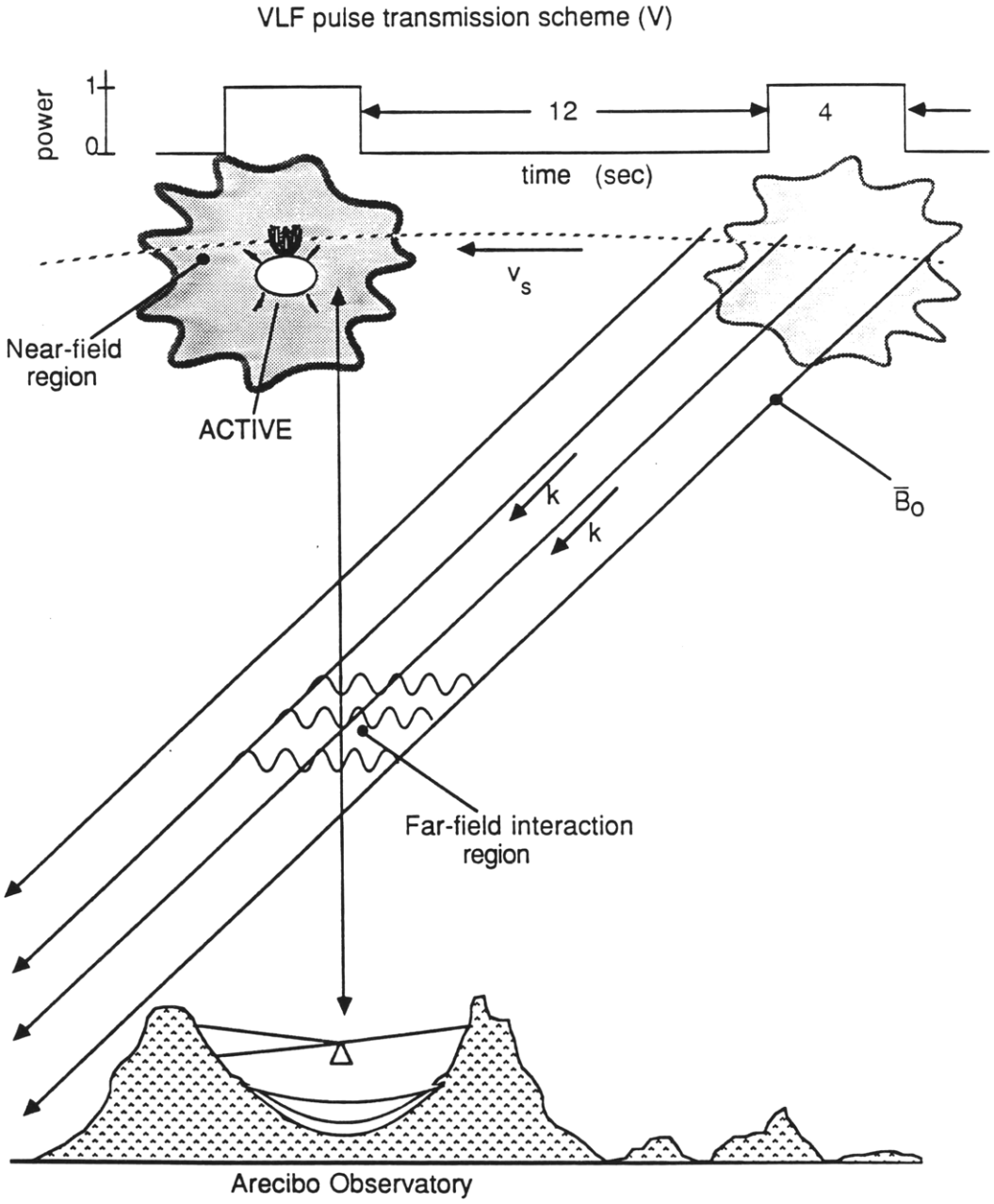

Figure 4-6: Ideal geometry for ACTIVE pass over Arecibo. Consecutive pulses map down the magnetic field lines at different altitudes over the radar allowing detection of various effects.

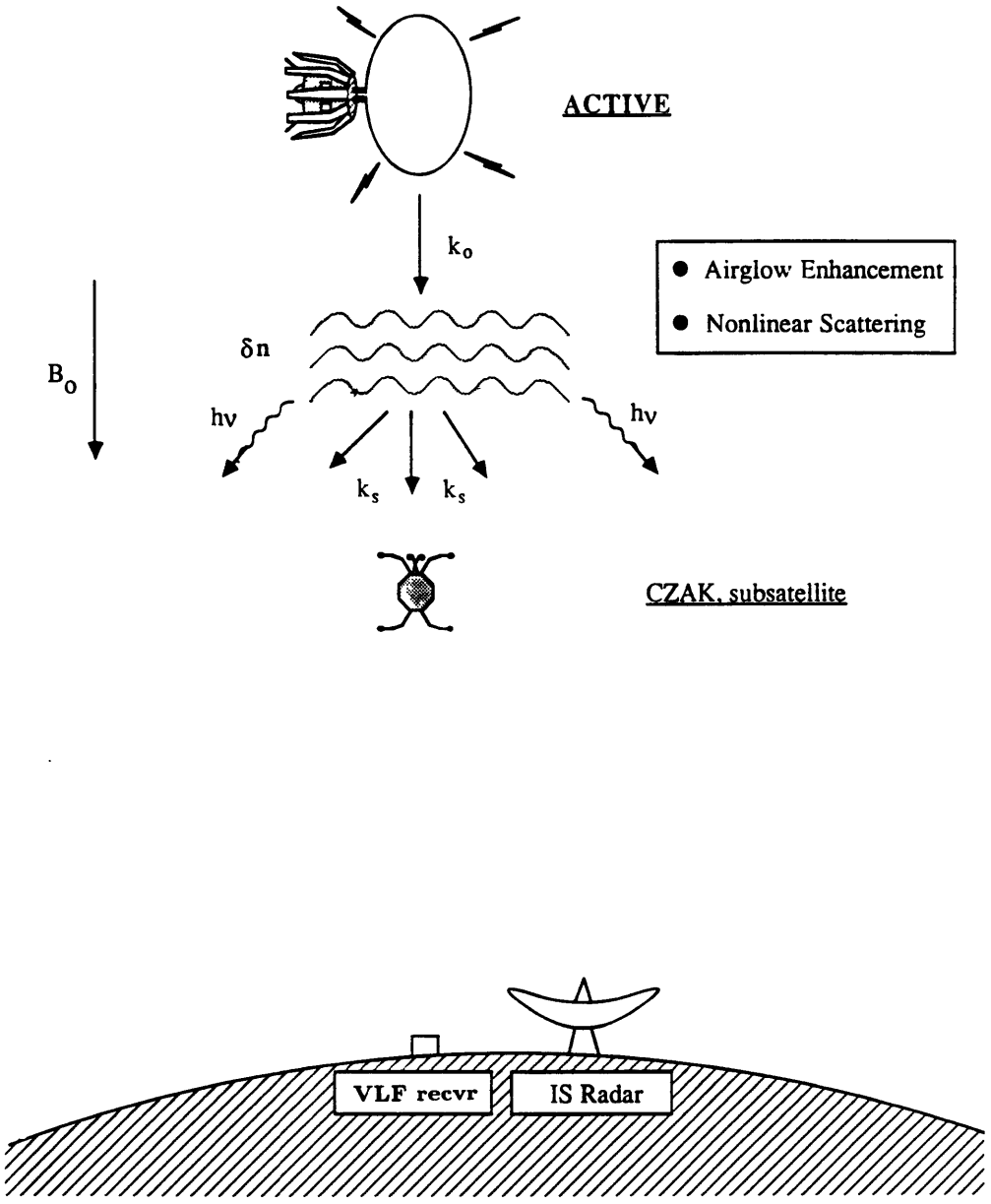

Figure 4-7: Proposed test of nonlinear scattering theory. HF heater induced irregularities scatter VLF waves which are subsequently detected by the CZAK subsatellite and a ground based receiver. The moving subsatellite should record broadened VLF spectra

No.	DATE	AST	AZ	EL	RNG (km)	τ_p (μsec)	τ_s (μsec)	HF Htr (MHz)
1	12/17/89	17:46	275.6	88.1	513	52 (BC)	Analog	8.175
2	12/28/89	16:29	93.6	73.5	548	4	Analog	8.175
3	03/20/90	19:45	272.5	82.9	535	~2	1	N/A
4	05/25/90	00:36	89.6	80.0	525	~2	1	N/A

Table 4.3: Summary of Direct–Look ACTIVE experiments conducted at the Arecibo Observatory.

there until the satellite flew through; the main beam transit time was only .25 seconds. Short radar pulses (τ_p) and rapid sampling rates (τ_s) were employed to provide maximum temporal and spatial data resolution. Unintegrated raw data were stored for a period of a few minutes during each overflight. These data were augmented by thorough diagnoses of ionospheric temperatures, densities, and drifts for extended periods preceding and following the passes.

The VLF transmitter was operated in a 1-sec on/1-sec off full power pulsed mode during each experiment to take advantage of its maximum duty cycle, maintainable for 48 seconds. Additional diagnostics on board ACTIVE were also utilized, including VLF wave detectors, temperature and density probes, and electron and ion particle detectors. A brief summary of the results of these experiments is provided below.

4.1.3 Experimental Results

For simplicity the experiments will be referred to by number in chronological order (see Table 4.3). References to VLF wave interaction mechanisms will correspond to the order in Table 4.2.

Experiment No. 1

This experiment was significant because the satellite passed through the geomagnetic flux tube that mapped into the HF heater volume above the UHF radar, facilitating the detection of both far field and near field effects in a single pass, as idealized

in Figure 4-6 (see Figure 4-8 for ground-track plot of all passes). The HF Heater was operated at 8.175 MHz to produce field aligned irregularities resulting in wave–plasma interactions via Mechanisms 3 & 4 (Table 4.2) and to accelerate electrons up the magnetic field lines to be measured by particle detectors on board the satellite. A tunable VLF receiving system was deployed to monitor VLF transmissions for spectral comparisons with the CZAK subsatellite. The radar beam was parked in a position to intercept ACTIVE at a range of about 514 km, and the ionosphere was monitored from 60–600 km altitude.

An enhanced image of the UHF backscatter power during the satellite's transit is shown in Figure 4-9. The data were recorded analog with a Honeywell 101 2-MHz bandwidth magnetic tape recorder and digitized later at a 1 μsec sampling rate. The lower edge of the satellite appears as a very large signal near the bottom of the plot beginning just after 1920 *m*sec. Because the raw data have not been decoded, subsequent bauds of the 13-bit 52 μsec Barker coded transmitted pulse are resolved as saturated echoes above the first reflected pulse baud. Additional localized echoes are evident occurring before and after the main echoes; these correspond to the satellite's passage through sidelobes of the Arecibo antenna.

Figure 4-9 shows a total of about four seconds of radar data, or two cycles of the ACTIVE VLF transmitter (1-sec on/1-sec off). Each second translates into a horizontal spatial range of about eight kilometers for the orbiting satellite. The intense near field of the the 10 kW VLF transmitter was expected to enhance radar backscatter effectively in a zone of several kilometers radius around the satellite. While the satellite itself leaves a clear signature in the radar beam, no enhanced backscatter in its vicinity is apparent.

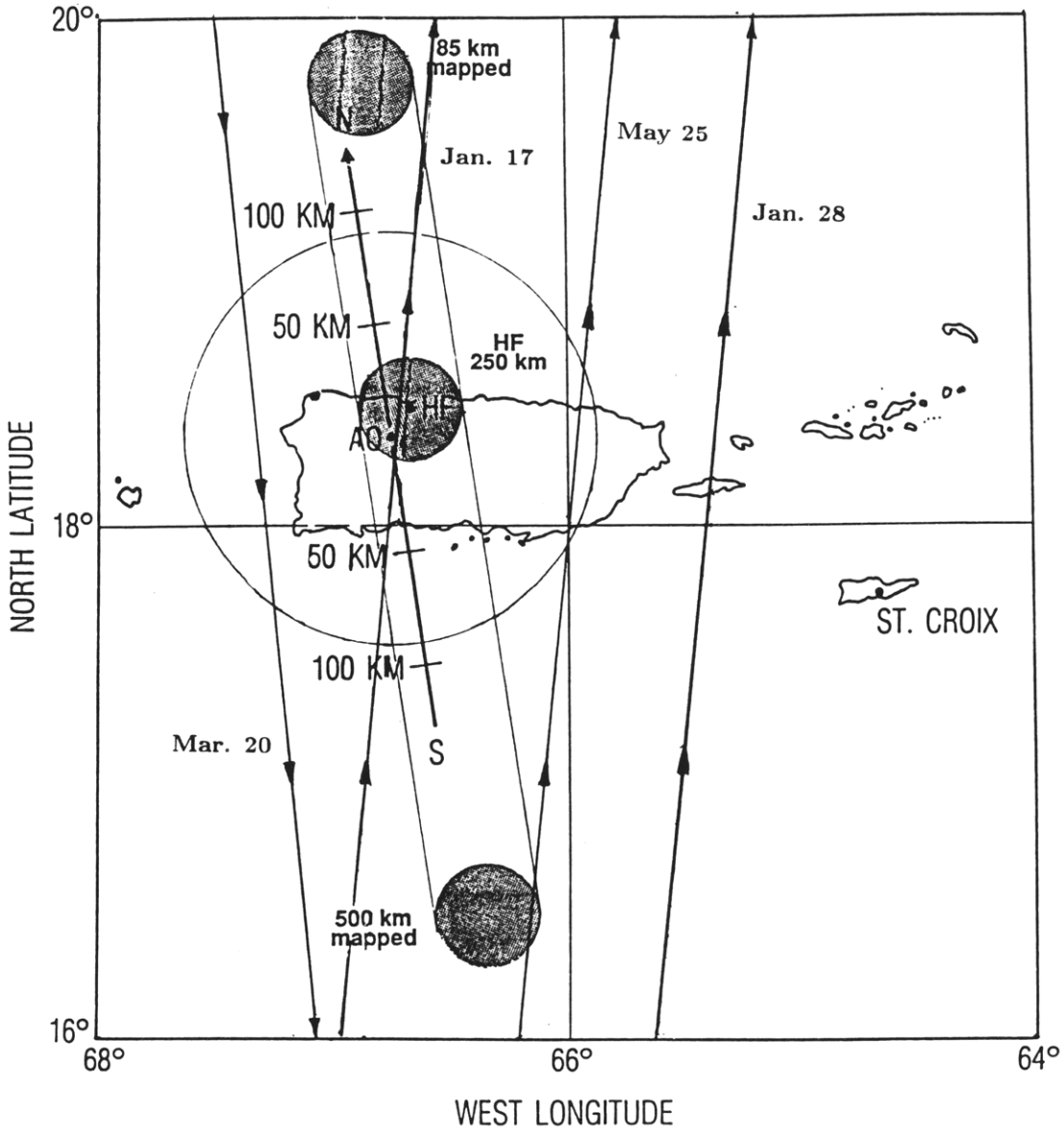

Figure 4-8: Ground track of four direct-look experiments over Arecibo. The heater beam area over Arecibo at 250 km is shaded and mapped along the magnetic field from 85 km to 500 km. The larger outer circle is the UHF radar field of view at 500 km.

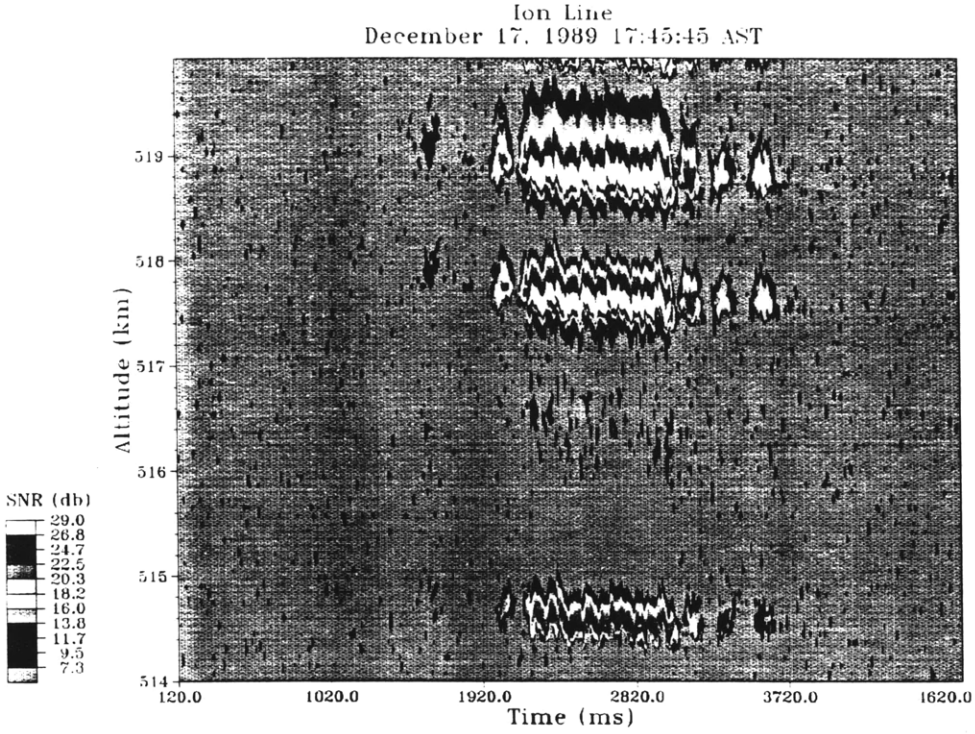

Figure 4-9: Image of backscattered power from ACTIVE pass on December 17, 1989

Experiment No. 2

As can be seen in Figure 4-8, the second overflight experiment was not directly through the HF heater flux tube; thus, far field interactions with existing irregularities could not be expected within the UHF radar field-of-view. Irregularities drifting into the flux tubes energized by the VLF transmissions, however, could induce nonlinear scattering and subsequent spectral broadening when detected by the CZAK subsatellite. The heating facility and the ground based VLF receiver were operated.

This experiment was designed to diagnose only the near field effects in the satellite's vicinity. In the first experiment it was noticed that the 52 μsec Barker coded pulse experienced some spread in range when it was decoded because of the large amplitude of the received signal during the satellite overflight. In other words, the 22 dB suppression of the Barker sidelobes was not sufficient to isolate the individual bauds of the code when the satellite penetrated the radar beam.

To eliminate this loss of range resolution in the second experiment a simple 4 μsec pulse was employed. A much narrower range of altitudes (450–600 km) was diagnosed with higher resolution. An image of the backscattered power as a function of time and altitude is shown in Figure 4-10. The satellite is detected first in the fourth sidelobe of the antenna beam just higher than 551 km altitude at a time of about 11.75 seconds. Four successive sidelobes illuminate the target before ACTIVE enters the main beam approximately one second later, where it remains for about .3 seconds.

The pattern is repeated as the satellite exits the beam, except that the sidelobe separation increases due to the relatively large zenith angle ($\theta \simeq 16.5°$) required to view the target in this experiment. The result is that the slant angle of the trajectory through the beam increases and, thus, both the effective range and time between sidelobe transits increase noticeably as the satellite moves away from the radar. The signal received from ACTIVE's lower edge echoes to higher altitudes due to temporal ringing of the saturated receiver system. As with Experiment No. 1, at least two full cycles of the VLF transmitter occur during the time period shown in the figure. However, there is little evidence of UHF backscatter enhancements due to the VLF transmissions. Neither were the transmissions themselves detected by the ground based VLF receiving system.

Experiment No. 3

In the ACTIVE experiment on 20 March, 1990 a 2 μsec transmitted pulse was oversampled to provide higher resolution measurements of the VLF near field than in the previous experiments. Reports that the CZAK subsatellite was not operational precluded the possibility of performing spectral broadening experiments. A lineplot of the received power integrated over 1.5 km is shown in Figure 4-11. The plot is normalized by the target's backscatter power in the main beam, which saturated the

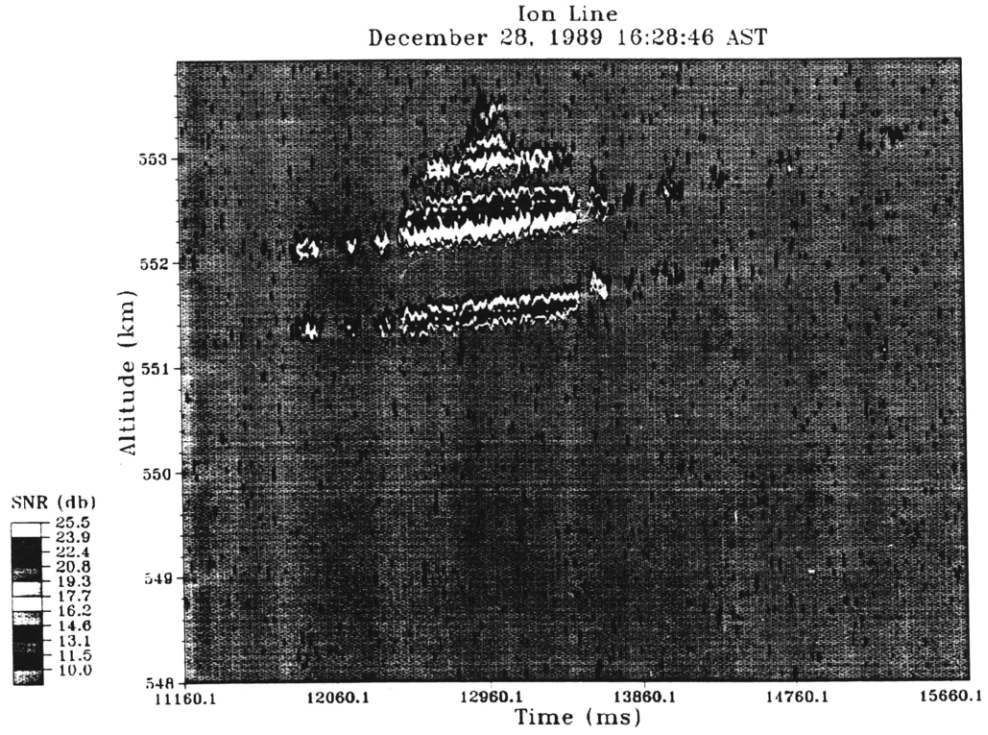

Figure 4-10: Image of backscattered power from ACTIVE pass on December 28, 1989

radar receiver system. The smaller power peaks flanking the main beam return are due to the primary ring sidelobe of the antenna.

Smaller amplitude features are more evident in Figure 4-12, where the backscattered power, averaged over three ranges centered on eight consecutive range gates, is plotted as a function of time. The spatial separation between gates is 150 meters. The satellite's entry into the beam commences at the highest range gate at approximately 250 time units (5 $m$sec/unit). The range to the radar decreases rapidly as the satellite approaches, descending through the beam. Four small sidelobes are evident in gates 592–595 as the target exits. As in the previous experiments, the backscattered power just below the satellite does not appear to be enhanced at any time during the pass, even though the VLF transmitter was activated for 1–2 seconds during the transit.

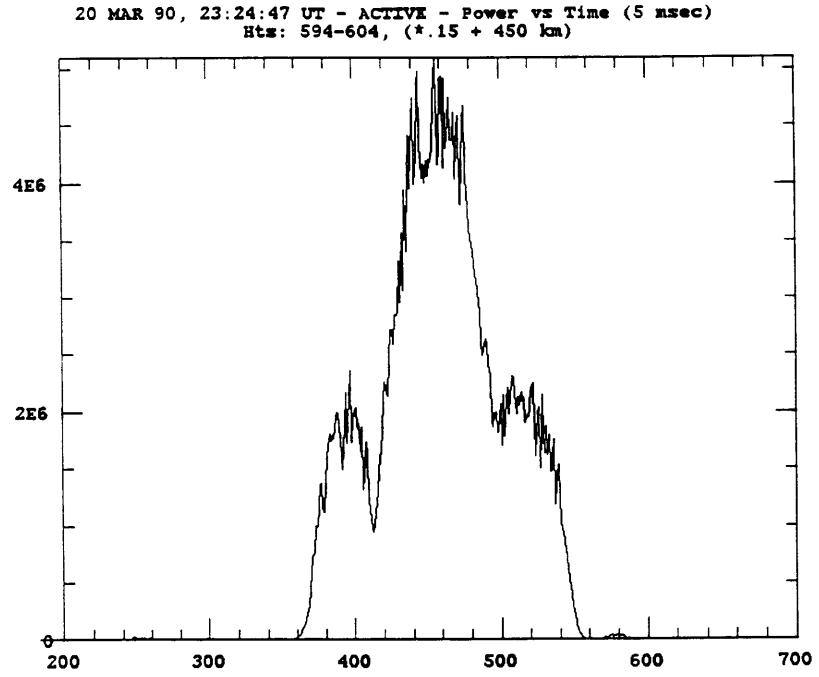

Figure 4-11: Backscattered power from ACTIVE pass integrated over 1.5 km (10 range gates). Higher order sidelobes appear as small bumps before and after the large return from the main beam. The y-axis is linear in relative power.

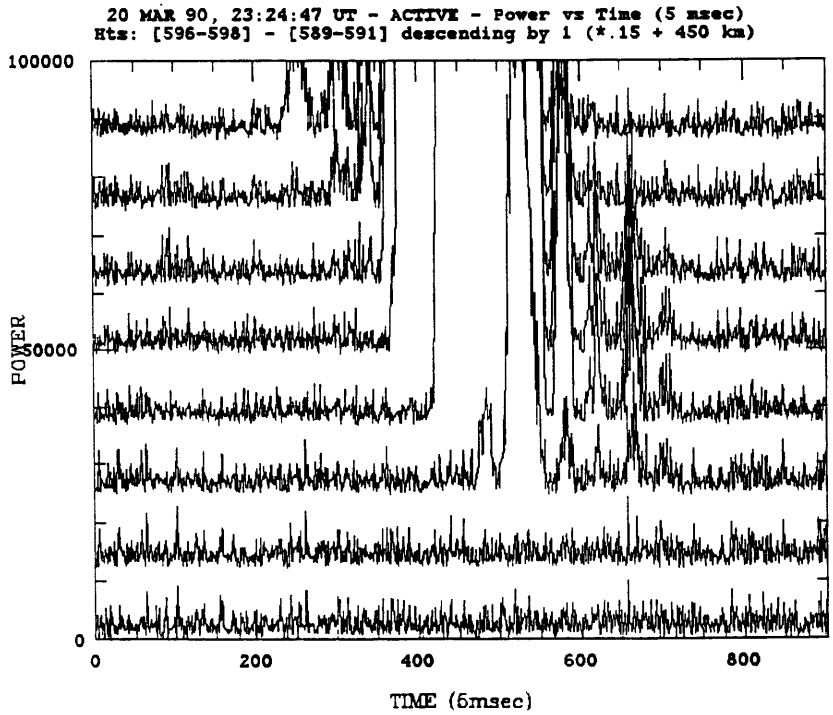

Figure 4-12: Backscatter power from ACTIVE pass showing returns from consecutive range gates. The main beam return is off scale; small maxima in power correspond to the sidelobes. The y-axis is linear in relative power.

Experiment No. 4

Except for the use of the HF heating facility, Experiment No. 4 was conducted much like Experiment No. 3.

Analysis of the Arecibo 430 MHz radar backscatter from the ACTIVE satellite overflight of 25 May, 1990, revealed enhanced power returns apparently beneath the satellite (see Figure 4-13). The total duration of the enhanced return is about .6 seconds, less than the 1–second VLF transmissions. Instabilities excited by the VLF waves may require an appreciable fraction of a second to grow to amplitudes sufficient to enhance radar backscatter. If the satellite began transmitting VLF shortly before entering the main radar beam at about 300 time units (10 *m*sec), the observed enhancements may have been caused by VLF–induced irregularities. Due to imprecise timing control, however, we do not know at exactly what time the transmitter was on or off, only that it was operating in a 1–sec on/1–sec off cycle during the overflight. The sharp localization in range implies that the irregularities occurred within 150 meters or less of the satellite body, and were probably intense only within a smaller radius.

While VLF-induced irregularities could have produced the backscatter evident in Figure 4-13, the discrete sampling technique used in the acquiring the radar data allows for an alternative explanation to the enhanced returns. Because the satellite's altitude decreased about 100 meters during its passage through the radar beam, it is possible the satellite descended to a lower sampling range gate (each gate represents 150 meters; see Figure 4-14). The returns appear beneath the satellite in the main beam and the first sidelobe, S1; if the satellite passed into the lower range gate, however, one would also expect an enhanced power signature in sidelobes 2 (S2), 3 and 4. As is evident in Figure 4-13, however, no enhancement is seen in these lobes at the lower range.

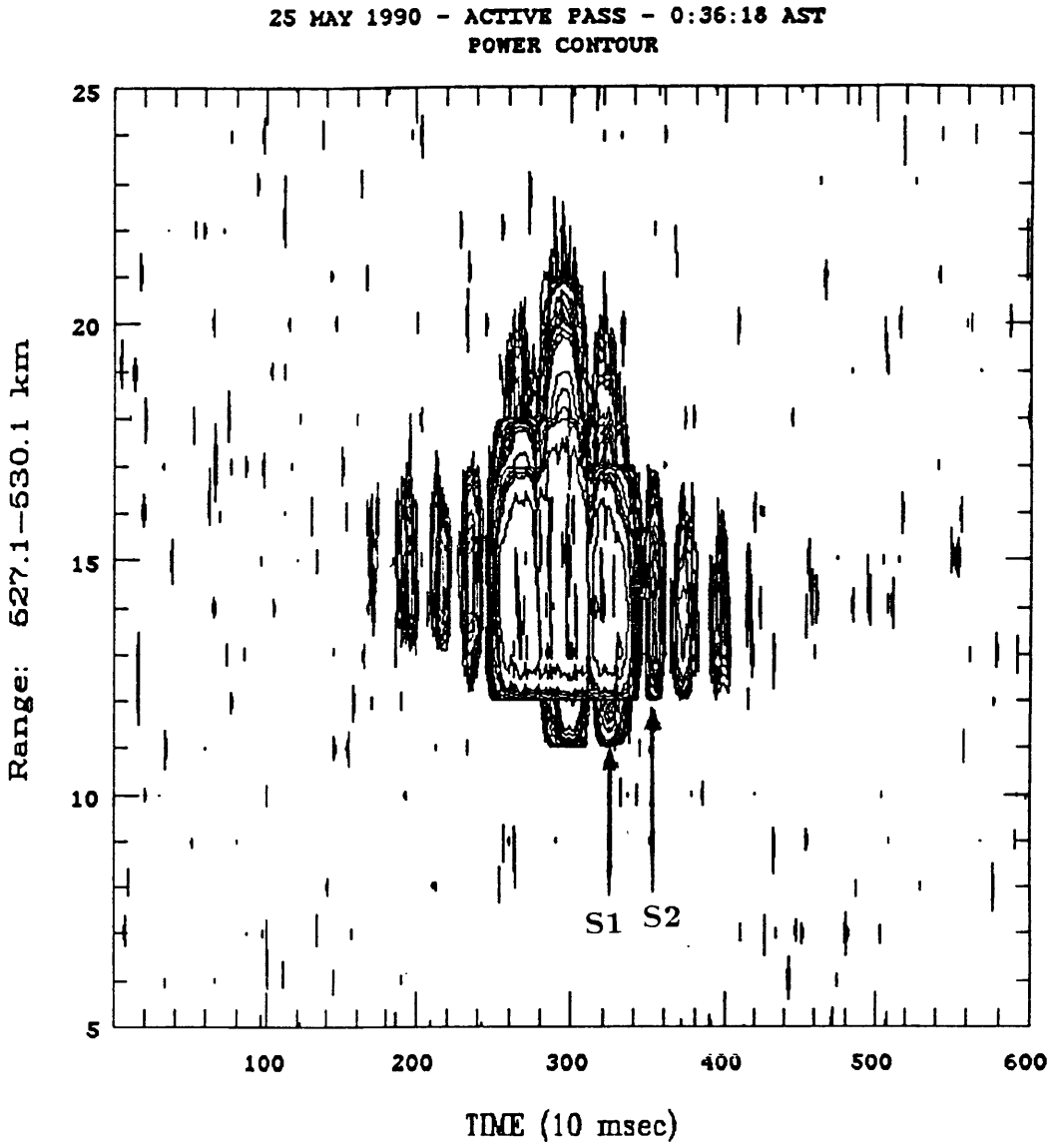

Figure 4-13: Contour plot of relative backscattered power from May 25 ACTIVE pass. S1 indicates 1st sidelobe; S2, the 2nd. Range gates are separated by 150 meters.

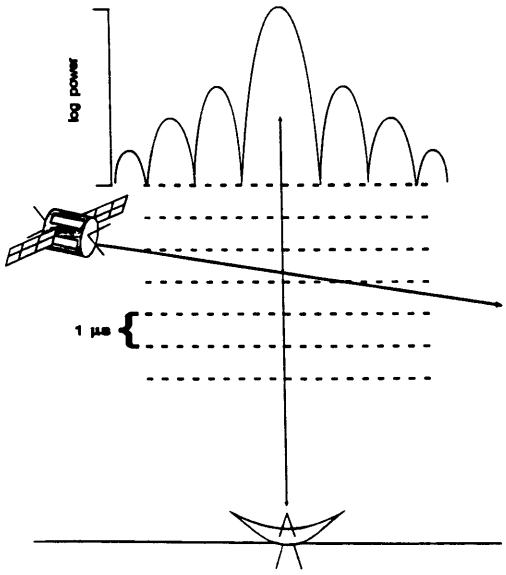

Figure 4-14: Cartoon depicting ACTIVE's transition through descending range gates as a function of the Arecibo antenna pattern. An enhanced return is apparent in the first sidelobe at the lower range gate, but the signal level is too low to be detected in subsequent sidelobes.

Radar data from the 20 March, 1990, ACTIVE pass shows that the power in S2 is at least 17 dB (a factor of 50) less than the power in S1. The peak power in S1 for the pass on 25 May at the lower range gate is 25,000 in arbitrary units. Therefore, we would expect a power return from S2 at this range to be approximately 50 times weaker, giving a level of about 500 in the same units. A return of this magnitude, however, is below the noise level in these experiments ($\approx$ 1000), and therefore undetectable. Thus, we cannot determine if the backscatter from the lower range gates is caused by VLF-induced density fluctuations or the marginal transition of the hard target to a lower range gate during the overflight.

4.1.4 Satellite Position/Radar Pointing Techniques

It is instructive to provide a brief description of the techniques employed to successfully diagnose the near vicinity of the satellite in each overflight experiment attempted. Two main sources of error exist: 1. Uncertainty in the satellite's position,

and 2. Errors in calculating look angles for the radar.

Because the beamwidth of the Arecibo UHF radar is only .15°, very accurate orbital information was necessary to intercept the ACTIVE satellite with the radar beam. Furthermore, this information had to be available at least two weeks prior to the actual pass for scheduling purposes and coordinating satellite control with our Soviet colleagues.

We obtained orbital ephemera for ACTIVE from the Lincoln Laboratory based at Millstone Hill in Westford, Massachusetts. These ephemera were monitored carefully and the most recent "element set", usually less than 24 hours old, was used to calculate several hours in advance the satellite's exact trajectory as it passed over Arecibo.

The pointing direction for the Arecibo UHF radar was calculated using a program called LOOKER at Millstone Hill. LOOKER utilizes coordinate transformations and an NCAR model for geodesy to calculate a range and bearing between any two points specified in common coordinates. Assuming perfect orbital positions, this calculation needed to be accurate to within at least .15° in pointing angle.

More on Satellites

The actual orbital motion of satellites is complicated by a dynamic frictional drag exerted by the earth's tenuous upper atmosphere. This drag force varies as the atmosphere expands and contracts due to fluctuating levels of solar flux. Satellite tracking models usually include only a static ballistic drag term, which is updated each time an orbiting object is actually observed with a Doppler radar system and a new element set is generated. The most recent element set is used to calculate the position of the satellite at a future time; the error in the projection generally increases as the projected time interval is increased.

Satellite orbits are fixed in a sidereal frame of reference, while the earth revolves beneath them at a constant rate. For satellites placed in high inclination polar orbits,

the earth's rotation effectively causes a longitudinal drift of the suborbital ground point. The rate at which the ground track drifts is given by,

$$v_d = R_e \omega \cos\lambda \approx .5\cos\lambda \text{ km/sec}$$

Here, R_e is the earth's radius in kilometers, ω is the earth's spin frequency, and λ is the latitude of the suborbital ground point.

The diameter of the UHF radar beam at ACTIVE's perigee altitude is only about 2.5 km. Therefore, a satellite "arriving" just three seconds "ahead of (or behind) schedule" will have drifted some 1.5 km and miss the parked radar beam. Clearly, small fluctuations in atmospheric drag on the satellite can have significant impact on the success of an experiment.

The amount of longitudinal drift between a projection two weeks in advance and the actual groundtrack can be significant, as shown in Figure 4-15. Trajectories calculated even 24 hours in advance must be accurate to within .003% to perform direct look experiments. Fortunately, element sets for ACTIVE were updated at least once everyday, and the projected positions were apparently accurate enough, since every attempt to hit the target was successful.

4.1.5 Millstone Hill Experiments

Several ACTIVE satellite experiments were conducted using the Millstone Hill 440 MHz steerable radar (MISA) to diagnose the perturbed region. A brief description of some of those experiments involving VLF transmissions is presented below.

The full steerability of the MISA allowed greater flexibility in choosing overflights than existed at Arecibo. The objectives remained the same, however, and the radar was used to look directly at, or slightly offset from, the satellite as it flew over the site. We were able to track the orbiter for up to two minutes continuously, several tens of VLF transmitter cycles, while looking for evidence of enhanced backscatter

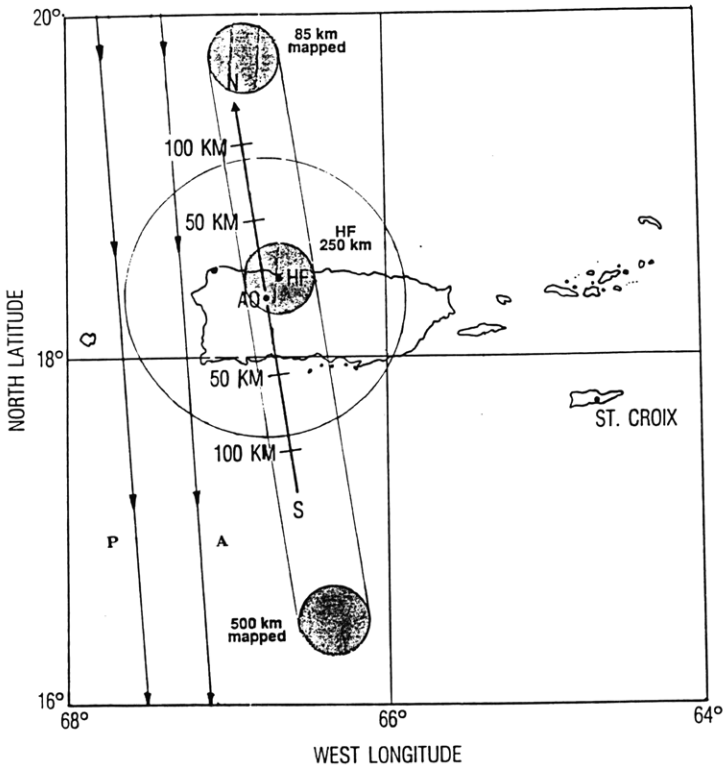

Figure 4-15: Typical change in subsatellite ground track over two week period. (P) marks the track projected from ephemeris two weeks prior to the pass; (A) shows the actual track followed by the satellite.

and/or changes in the spectral characteristics of the received power. Even though the Millstone Hill radar is less sensitive than the Arecibo system, it was hoped that the extended tracking capability might reveal small effects modulated by the VLF transmissions. In addition, the transmitting satellite was monitored over an extensive range of latitude and altitude;

Data for experiments run on 13 December 1989, 27 December 1989 and 20 March 1990 are shown in Figures 4-16–4-18. In Figures 4-16 and 4-17 the echo power from the satellite's location is plotted above a graph showing the "predicted" path used to program the radar pointing angles and the "actual" path followed by the satellite. In the 13 December experiment the echo strength varies significantly, but does not exhibit the 4-sec on/12-sec off modulation radiated by the VLF transmitter. The antenna tracked the satellite with a 2° offset in elevation angle. The received power in the 27 December pass varies more smoothly, but there is still no evidence of VLF

induced effects. The echo power here is plotted in units of the logarithm of the effective electron density (per cm^3). For comparison, an echo power of 5 ($n_e = 10^5/cm^3$) corresponds to a volume reflectivity of 10^{-17} m^2/m^3, or a total cross section of about 10^{-4} m^2.

The variability of the backscattered power is probably due to the changing position of the satellite within the 1° radar beam. This is particularly true in the 13 December experiment, where the 2° offset placed the satellite on the fringe of the main beam where the beam pattern exhibits a strong gradient. It is difficult to program a precise variable track with the MISA while acquiring data at relatively short integration times (~5 sec).

This is primarily because the angular rate of change in the radar's bearing to an orbiting target during a pass varies parabolically, while the antenna controller extrapolates linearly between two assigned look angles. There are also practical engineering limitations to consider. Initiating rapid changes in position and slew velocity with the massive 150 foot dish can introduce inertial overshoots followed by corrections and result in jerky, small amplitude antenna motions.

Under such circumstances, it is difficult to keep the target centered in the beam for an extended time period. Figure 4-18 shows sequential power spectra plots from the 20 March experiment. The satellite, which appears in the spectra as a narrow Doppler spike moving closer to the center frequency in time as the line-of-sight velocity decreases, remains in the beam for a total of about two minutes. Recognizing that the return power from the ionosphere (the ion line) is essentially constant over this time period and that each spectrum is self normalized, one can see that the signal from the target fluctuates substantially.

Unfortunately, this fluctuation is probably not related to VLF transmissions, but instead results from varying target positions within the radar beam for reasons de-

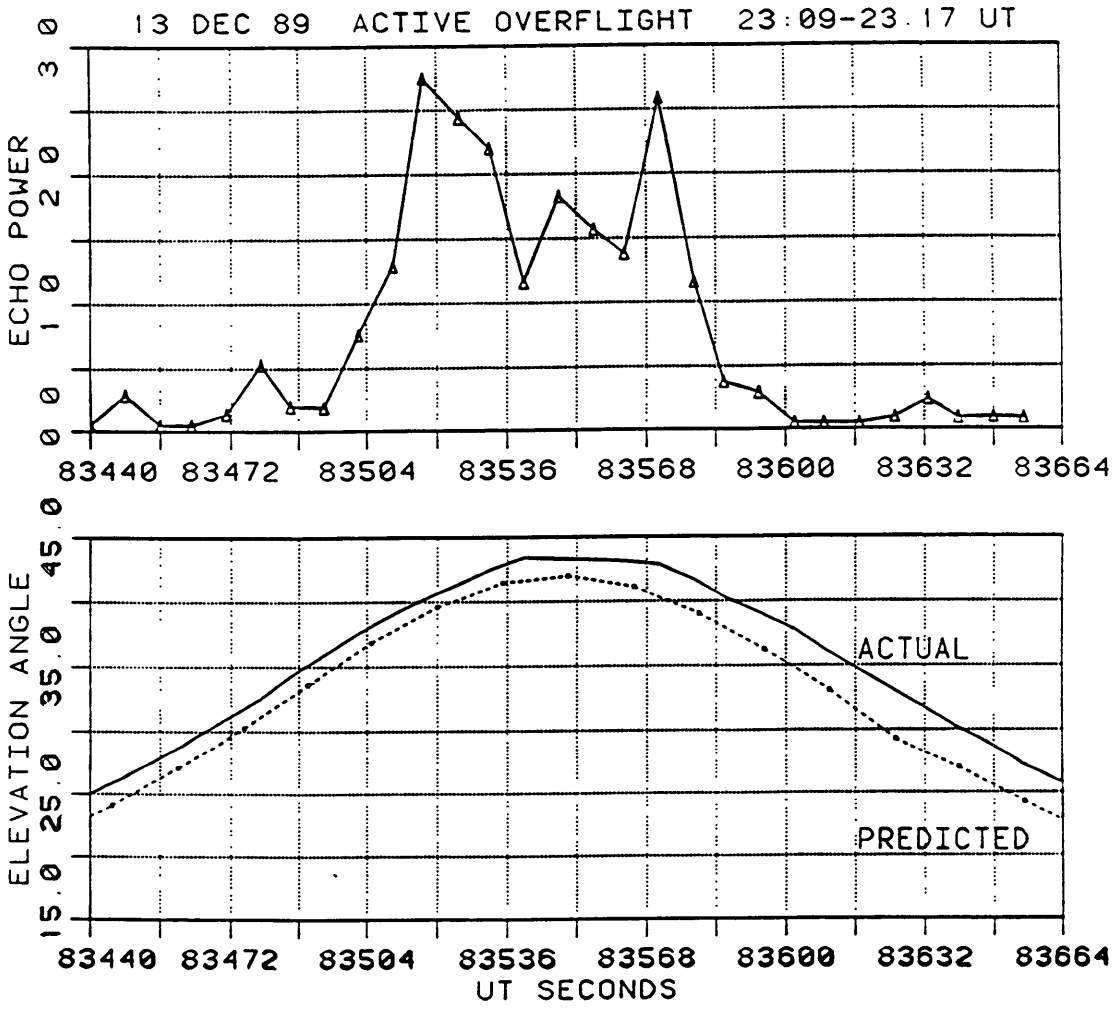

Figure 4-16: Echo power and antenna track for ACTIVE pass over Millstone Hill. The antenna tracked the satellite at an elevation angle offset of 2°; The satellite was in the radar beam from 83500 sec to 83585 sec. Echo power is in units of the logarithm of 10^{-3} times the effective electron density.

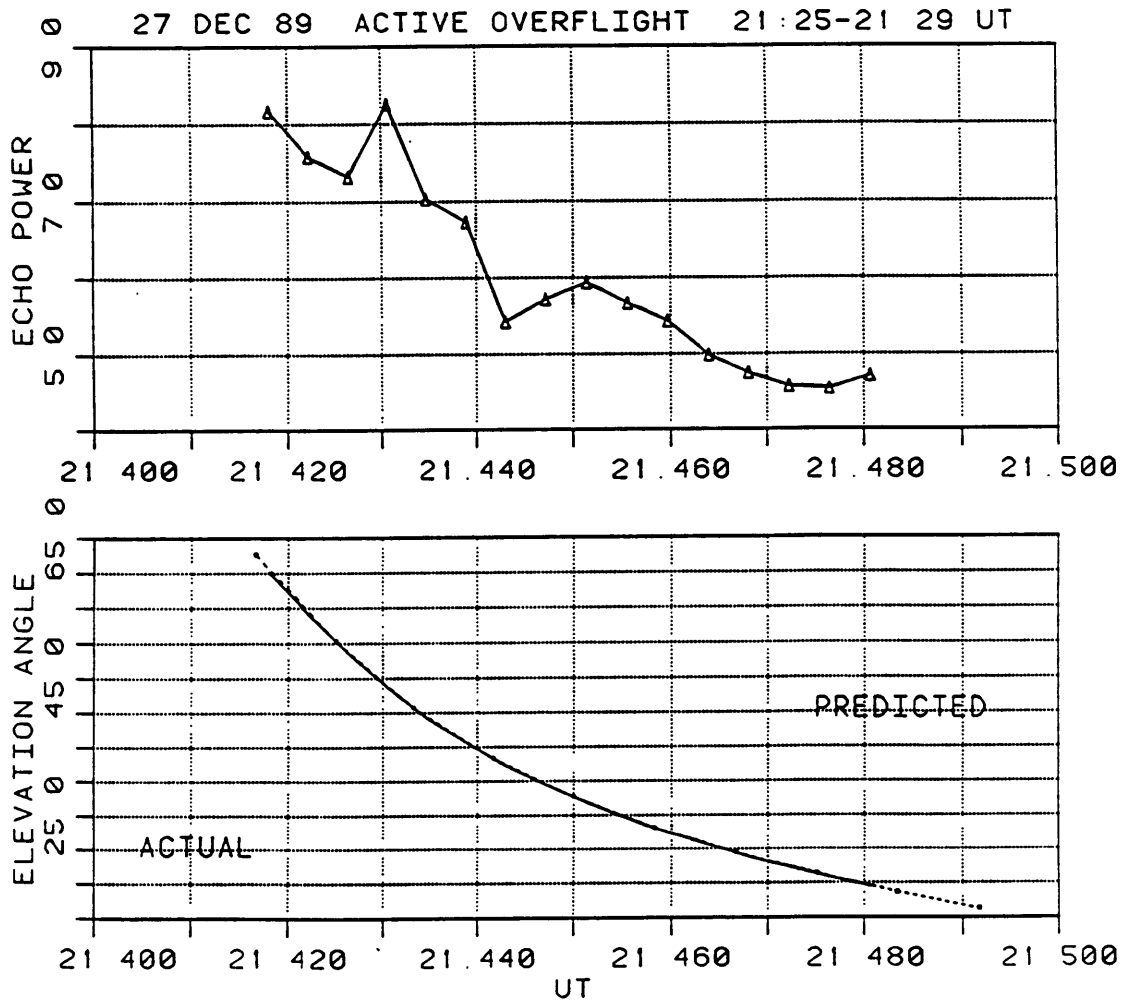

Figure 4-17: Echo power and antenna track for ACTIVE pass over Millstone Hill. The antenna was pointed directly at the satellite. Echo power variations probably are due to fluctuations in the target's position in the beam. Echo power is in units of the logarithm of effective electron density.

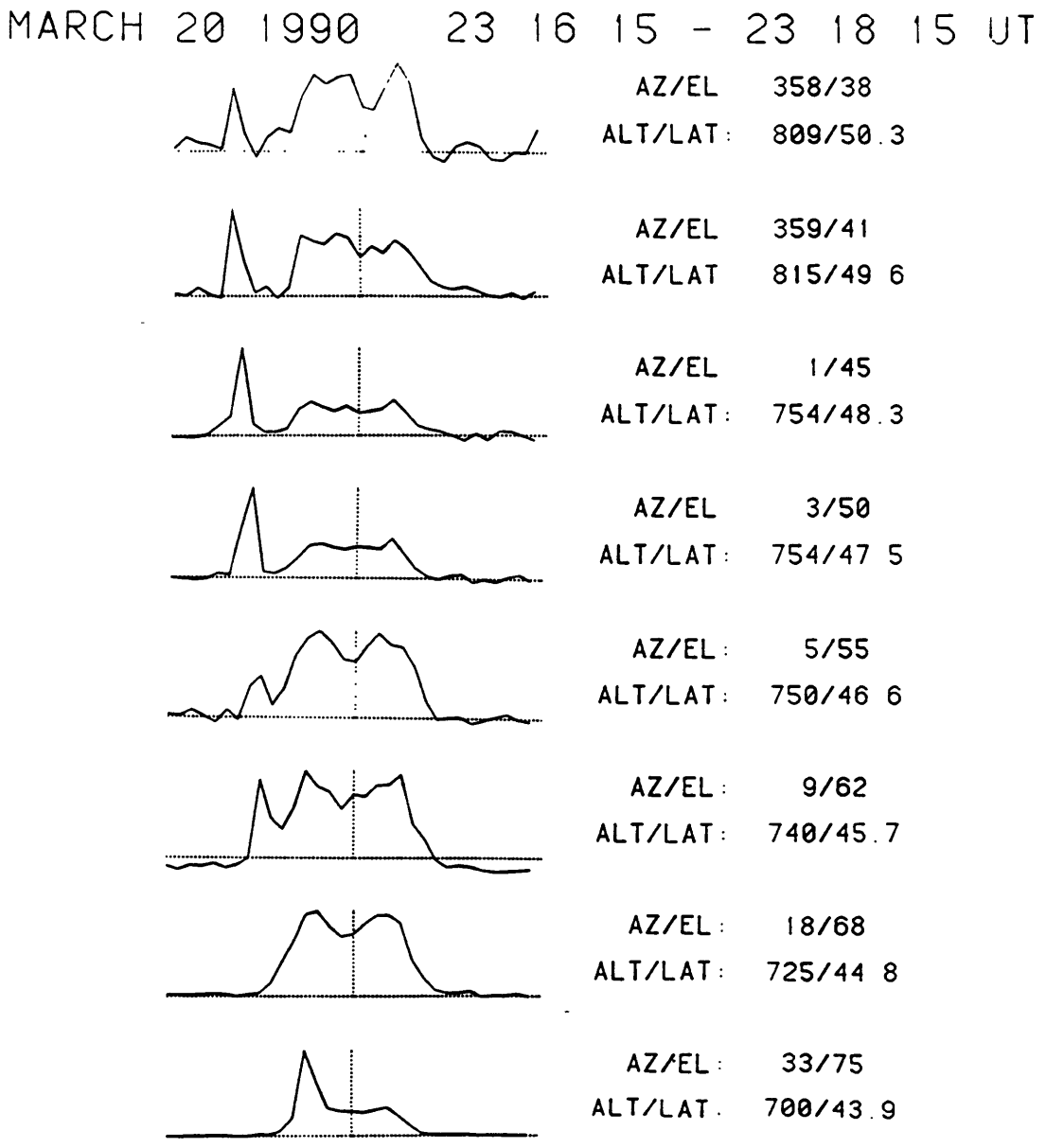

Figure 4-18: Consecutive power spectra showing the approach of the ACTIVE satellite from Millstone Hill. The spectra are computed from 30–sec integrations and plotted self-normalized. There is no evidence the power variations are caused by VLF transmissions.

scribed above. Like their counterparts at Arecibo, none of the Millstone Hill ACTIVE experiments showed evidence of VLF wave enhanced radar backscatter.

Summary of Experiments

The ACTIVE satellite promised investigators in the Soviet Union and the United States an opportunity to perform exciting new in situ modification experiments in space. However, with very sensitive ground diagnostics we were unable to successfully detect the ionospheric effects expected from powerful VLF transmissions, or even the actual transmissions. To determine why such effects were not seen, the relevance of the VLF parametric instability described in Chapter 3 to the ACTIVE experiments had to be considered carefully.

4.1.6 The Role of Parametric Excitation in the ACTIVE Experiments

Reviewing the parametric excitation mechanism, we recall the VLF pump wave induces observable effects in the plasma in two steps. In the first step, the VLF wave (whistler mode) excites lower hybrid waves and a zero frequency (purely growing) mode in the plasma. The daughter lower hybrid waves generated by the whistler wave act as pump waves driving additional lower hybrid sidebands in the second step. The reduced phase velocity of the upshifted sideband mode enables it to interact with thermal particles and cause observable density fluctuations and airglow.

The parametric instability predicts significant growth ($\gamma \geq 10$ sec^{-1}) of the lower hybrid modes for pulses of 1–sec duration or longer for electric field amplitudes of the order of 1 (10) V/m at an altitude of 1000 (500) km. The passes over the Arecibo Observatory were observed at altitudes from 500–650 km, requiring a relatively large electric field (10–30 V/m) to achieve detectable effects. Soviet scientists' analysis of

the near zone indicated that the field amplitudes of whistler mode waves generated by the VLF transmissions from the satellite would probably not reach such high values [*U.S.S.R. Space Research Inst.*, 1987]. However, within a few kilometers of the spacecraft, they expected the 10 kW transmitter to generate electrostatic fields in excess of a 100 V/m due to self focusing of the waves caused by locally intense radiation pressure.

These fields would excite lower hybrid oscillations directly, effectively bypassing the first step of the instability, providing an intense lower hybrid pump wave which should drive lower hybrid sidebands as described in the second step, and subsequently enhance the backscatter from the probing UHF radar. Radar measurements were made with a spatial resolution of at least 150 meters in the immediate vicinity of the transmitting satellite; nevertheless, the anticipated enhancements were not seen.

The ACTIVE experiments conducted from Millstone Hill were similar to those at Arecibo. The lower sensitivity of the Millstone Radar compared to Arecibo was partially compensated for by the tracking capability which enabled us to use longer VLF pulse lengths and monitor the satellite through an extensive range of altitudes, varying geophysical conditions. The four second VLF pulses employed in some of the experiments provided longer periods for wave growth compared to the one second pulses used in the Arecibo experiments. At higher altitudes the threshold for instability decreases significantly and should have been easily exceeded by the powerful transmitter.

Despite the predictions of apparently sound calculations and the careful acquisition of seemingly high quality data, no evidence of enhanced radar backscatter was seen in the experiments. The probable cause for the lack of concrete results was not due to negligence in either our calculations or our experimental techniques, however; as we were informed by our Soviet colleagues, a problem with the VLF antenna had

been detected.

Antenna Deployment Problems

The VLF antenna was originally designed to be "unrolled" from the ACTIVE satellite in orbit to form a 20 meter loop as shown in Figure 4-19a. Once deployed, the antenna should have drawn a current of 150 amps from the VLF transmitter, radiating 10 kW at full power. Shortly after deployment, Soviet scientists discovered that the antenna was drawing no more than 15 amps from the transmitter, implying a loss in output power of at least 20 dB.

The problem was identified as a gross mismatch in impedance between the antenna and the transmitter, probably due to a modified antenna configuration, such as that shown in Figure 4-19b. In any case, estimates of radiated VLF power fell from 10 kW to about 100 W to perhaps a few tens of watts. At such power levels, radiation pressure would be too weak to induce wave focusing and electric fields would be too small to exceed instability thresholds at low altitudes, and probably, except perhaps within a few tens of meters from the spacecraft, at high altitudes as well.

This disappointing development in the ACTIVE satellite program underscores the risks associated with space-based instrument platforms. Nevertheless, the experiment had valuable scientific merits in-principle, promising investigators an opportunity to explore the interactions of VLF waves with plasmas, which cannot be studied in laboratory settings on earth, and generating renewed theoretical interest in VLF wave propagation. Furthermore, the program established communications protocol for collaboration with Soviet colleagues from which future US/USSR joint programs are sure to benefit.

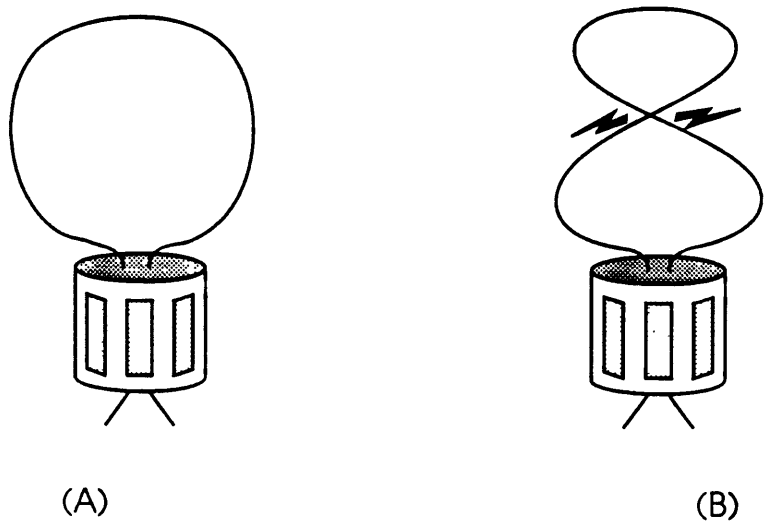

Figure 4-19: (A) The deployment of the 20 meter VLF loop antenna as designed. (B) The suspected actual deployment of the antenna in orbit. The figure–8 configuration seriously degraded antenna performance.

Chapter 5

Observations of Enhanced Radar Backscatter (ERB) from Millstone Hill

Intense ($\simeq$ 20 dB) enhancements of the incoherent radar backscatter spectrum from the topside ionosphere have been observed with the Millstone Hill UHF radar. Enhancements occurring at the local ion acoustic frequency causing large asymmetries in the measured ion line may be produced by current-driven instabilities [*Foster et al.*, 1988] (henceforth, FOS88). These enhancements pose a practical problem for space surveillance systems because their cross section and spectral width are characteristic of satellites.

Conversely, their hard target signature complicates the study of naturally occurring ERB events; it is nearly impossible to distinguish them from satellites based on a single measurement. Statistical comparisons of observed coherent echo distributions with predictions from a satellite catalog have been used to broadly identify periods of ERB activity. A series of experiments using multiple diagnostics, including satellite instruments, for simultaneous observations have established the association of ERB

with large fluxes of soft suprathermal electrons carrying field-aligned currents. Zenith data are also presented which show the asymmetric growth of ion acoustic waves directly above Millstone Hill. Zenith measurements filter out satellite contamination because the geometry constrains the Doppler shift from orbiting bodies to velocities significantly less than the ion sound speed in the F region.

Details of these results are presented in this chapter. First, however, a brief description of the normal incoherent scatter spectrum is reviewed, followed by a description of the characteristics of the ERB spectra.

5.1 Incoherent (Thomson) Scatter Process

The radar technique for studying the earth's upper atmosphere typically employs a (HF, VHF or UHF) radar to transmit a powerful pulse of electromagnetic radiation into the atmosphere. Following transmission, the radar is used to receive the radiation scattered by the atmosphere back to the antenna. If the details of the scattering process are understood, meaningful information about the medium can be extracted through the appropriate processing of the weak received signal. For the partially ionized upper atmosphere above about 60 km altitude, the electromagnetic waves are scattered by electrons in a process known as *incoherent* or *Thomson* scatter, named after J. J. Thomson who first showed that individual electrons can scatter electromagnetic radiation [1906].

5.1.1 Relationship Between Density Fluctuations and Scattering Properties

The frequency spectrum of the high frequency radiation scattered by the ionosphere is directly related to the power spectrum of the electron density fluctuations in the

plasma. Mathematically the cross section of the plasma as a function of radar carrier offset frequency, ω, may be expressed as

$$\sigma_\omega = \sigma_e V \langle |n(\mathbf{k},\omega)|^2 \rangle \tag{5.1}$$

Here, $\sigma_e \approx 10^{-28}\mathrm{m}^2$ is the scattering cross section of a single electron, V is the scattering volume, $\langle\ \rangle$ indicate a time average; $\mathbf{k}$ and ω are the difference of the incident and scattered wave vectors and frequencies, respectively, *viz.* $\mathbf{k} = \mathbf{k}_i - \mathbf{k}_s$ and $\omega = \omega_i - \omega_s$. For the usual backscatter radar geometry, $\mathbf{k} = 2\mathbf{k}_i$; thus, the incident radar wavelength, $2\pi/|\mathbf{k}_i|$, determines the scale size of density fluctuations sampled. Here, $n(\mathbf{k},\omega)$ is the space–time Fourier transform of the usual number density in the plasma, $n(\mathbf{r},t)$, defined by

$$n(\mathbf{k},\omega) = \frac{1}{VT}\int_V d\mathbf{r} \int_{-T/2}^{T/2} dt\ n(\mathbf{r},t) \exp[i\mathbf{k}\cdot\mathbf{r} - i\omega t] \tag{5.2}$$

T in this equation represents a time greater than the correlation time of the plasma medium. The total cross section of the plasma can be obtained by integrating (5.1) over ω,

$$\sigma_{tot} = \int_{-\infty}^{\infty} \sigma_\omega\ d\omega \tag{5.3}$$

Spectrum of Density Fluctuations

The key to determining the characteristics of the received scattered wave, then, lies in calculating the power spectrum of density fluctuations in the space plasma.

When only the random thermal motions of the scattering particles are considered, the spectrum exhibits a broad peak centered on the carrier frequency and a characteristic width of the electron thermal velocity, $\Delta\omega \approx kv_{te}$ [*Fejer*, 1960]. The total cross section as determined by (5.3) is found to be simply $N\sigma_e$, where N represents the total number of electrons in the scattering volume. This result has a straightforward physical interpretation as follows.

The electrons are assumed to undergo random thermal motions, implying that each electron will scatter signals of random phase relative to the other electrons. At the radar receiver the signal powers rather than the signal voltages will add, and the resulting cross section will be equal to the sum of the individual contributions of each electron, $N\sigma_e$. The random phase of the scattered signals suggests the use of the name *incoherent scatter* to describe this process.

However, as more detailed calculations show, the presence of ions in the plasma does introduce a degree of coherence between the electrons' motions [*e.g.*, *Hagfors*, 1961; *Salpeter*, 1960, 1961; *Dougherty and Farley*, 1960; and others]. The influence of the ions is found to be important when the incident radar wavelength is much larger than the so-called *Debye length* in the plasma, given by

$$\lambda_D = \left(\frac{\epsilon_o K T_e}{ne^2}\right)^{1/2} = \left(\frac{v_{te}}{\omega_p}\right) \tag{5.4}$$

where ϵ_o is the permittivity of free space, K is Boltzmann's constant, and T_e, n, e, v_{te}, and ω_p are the electron temperature, density, charge, thermal velocity and plasma frequency, respectively.

The Debye length is measure of the distance over which the plasma can shield out electric fields; in the ionospheric F region, $\lambda_d \approx .003$ meters. For distances greater than this length the plasma dynamics are characterized by collective processes rather than the random thermal interactions of individual electrons. The resulting scattering can best be thought of as arising from density fluctuations associated with electrostatic oscillations in the plasma[1]. The idealized power spectrum of density fluctuations under these conditions is shown in Figure 5-1.

[1]The term *incoherent* is not strictly accurate in this case and an alternative name, *Thomson scatter*, has also been applied to this phenomenon.

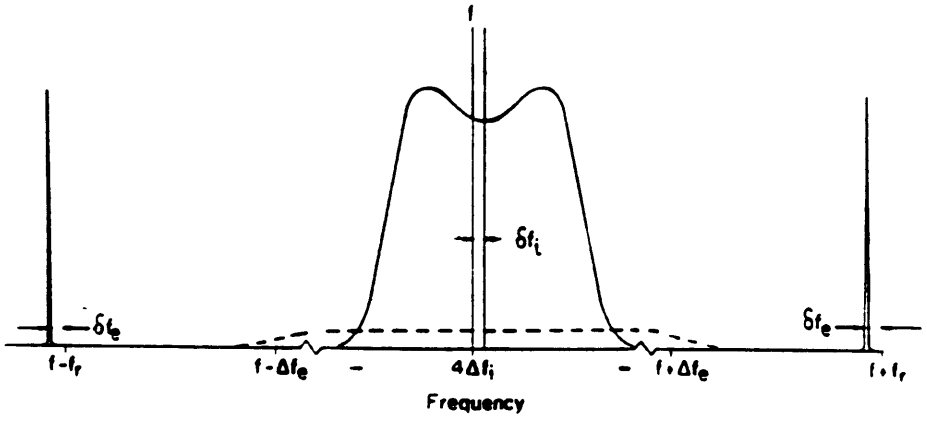

Figure 5-1: Incoherent scatter power spectrum when $\lambda \gg \lambda_d$. [after *Rishbeth*, 1989]

5.1.2 The Incoherent Scatter Radar Spectrum

The power spectrum in Figure 5-1 consists of two components. The double–humped central spectrum results from density fluctuations associated with ion waves and is correspondingly known as the *ion line.* The sharp peaks flanking the ion line are caused by high frequency electron density fluctuations called plasma waves; this component is therefore known as the *plasma line.*

The Ion Line

The ion waves that give rise to the ion line in the incoherent scatter spectrum are longitudinal oscillations with a phase velocity given by the "sound" speed in the plasma. The dispersion relation for these ion acoustic waves is given here,

$$\frac{\omega}{k} = \left(\frac{KT_e + KT_i}{M_i}\right)^{1/2} \equiv C_s \tag{5.5}$$

where M_i is the ion mass and C_s is defined as the ion sound speed in the plasma, typically 1–2 km/sec in the ionospheric F region. While these waves are ion oscillations,

the electrons follow the motion because of their electrostatic attraction to the massive ions. The two peaks in the ion line power spectrum may be thought of as reflections from ion acoustic waves travelling towards (upshifted peak) and away (downshifted peak) from the radar. The peaks are broadened due to ion thermal motions. Analysis of the shape and magnitude of the spectrum yields several important ionospheric parameters [see, *e.g.*, *Evans*, 1969].

The spectral width corresponds to the ion acoustic phase velocity, which from Equation (5.5) depends primarily on the electron temperature and the mass of the dominant ion species. The offset, δf_i, of the entire spectrum relative to the radar center frequency yields the line-of-sight bulk plasma drift. The electron–ion temperature ratio determines the sharpness of the spectrum's peaks. The area under the ion line curve is directly related to the electron density. These parameters are usually derived through a numerical model which adjusts their values to achieve a best fit to the observed power spectrum.

The Plasma Line

The plasma line component of the incoherent scatter spectrum is usually much weaker than the ion line and more difficult to measure. The sharp peaks result from electron oscillations near the plasma frequency. The dispersion relation for these waves in a magnetized plasma is given by,

$$\omega^2 = \omega_p^2 + \frac{3}{2}k^2 v_{te}^2 + \Omega_e^2 \sin^2\theta \tag{5.6}$$

where Ω_e is the electron cyclotron frequency and θ is the angle between the wave and the geomagnetic field. Usually the dominant term in (5.6), the electron plasma frequency, $\omega_p \propto n^{1/2}$, provides a very accurate indicator of the electron density. The intensity of the plasma line is dependent on the electron temperature. The difference in the relative offset frequency between the upshifted and downshifted lines allows a

determination of the bulk electron drift velocity. This velocity can be compared with the bulk velocity estimated from the ion line measurement to calculate the relative drift between the electrons and ions (*i.e.*, current).

In summary, we have presented the characteristics of the normal incoherent scatter power spectrum. The spectral features of the recently observed enhanced radar backscatter, examined in the next section, exhibit significant departures from the normal spectrum.

5.2 Characteristics of Enhanced Radar Backscatter (ERB)

Intense coherent radar returns from the topside of the ionospheric F region have been a regular feature of the Millstone Hill UHF incoherent scatter radar data for many years. Because these returns are characterized by the large radar cross sections and narrow spectral widths which can result from satellite penetration of the 1° radar beam, they have, until recently, been dismissed solely as hard target contamination of the incoherent scatter data. Foster et. al [1987] noted an anomalously high occurrence of intense radar echoes in the vicinity of the mid-latitude ionospheric trough. The unique geophysical conditions associated with the trough, such as field-aligned current activity and steep plasma density gradients, suggest that some of the coherent returns may be caused by enhanced ionospheric plasma density fluctuations, rather than orbiting objects intersecting the radar beam [FOS88].

The generation of such spectra may be attributed to current-driven ionospheric plasma processes [FOS88]. The processes described by Kindel and Kennel [1971] and Rosenbluth and Rostoker [1962], for example, predict the amplification of ion acoustic waves in the presence of intense currents and explain several features of the

observed enhancements, as discussed in Chapter 7. Here we present evidence derived from several sources for the observation of stimulated ion acoustic wave growth with the Millstone Hill UHF radar. These include statistical analyses of large data sets, multi-diagnostic measurements, and the observation of ERB in zenith experiments.

5.2.1 Satellite Contamination and Statistical Analyses of ERB

The task of separating satellite returns from true ionospheric coherent echoes is difficult because the integrated spectral features of both are essentially identical. This is illustrated in Figure 5-2, where the power spectra of the normal incoherent scatter ion line, an intense return from an enhanced ion line, and spherical satellite number 9636 are plotted on the same frequency scale for comparison; each plot is self-normalized. Even on a pulse-to-pulse basis satellite returns may vary by as much as 20 dB due to reflecting surface irregularities and rotation effects [*S. Sridharan*, private communication, 1988]; the size of this variation is comparable to the magnitude of the largest geophysical ERB events. Thus, the similarity between geophysical ERB spectra and satellite spectra makes unambiguous classification of individual ERB events difficult. Several approaches to the resolution of this problem have been employed; the most successful involves the statistical reduction of large data sets, as described below.

The Satellite Catalog

A large number of satellites pass through the Millstone I.S. Radar field of view during any particular experiment; their spectral signatures constitute the primary source of coherent echo contamination in the topside ionosphere. At Millstone Hill we are fortunate to have access to a complete catalog of the known orbiting space objects. An altitude distribution of orbiting objects generated from this catalog is shown in

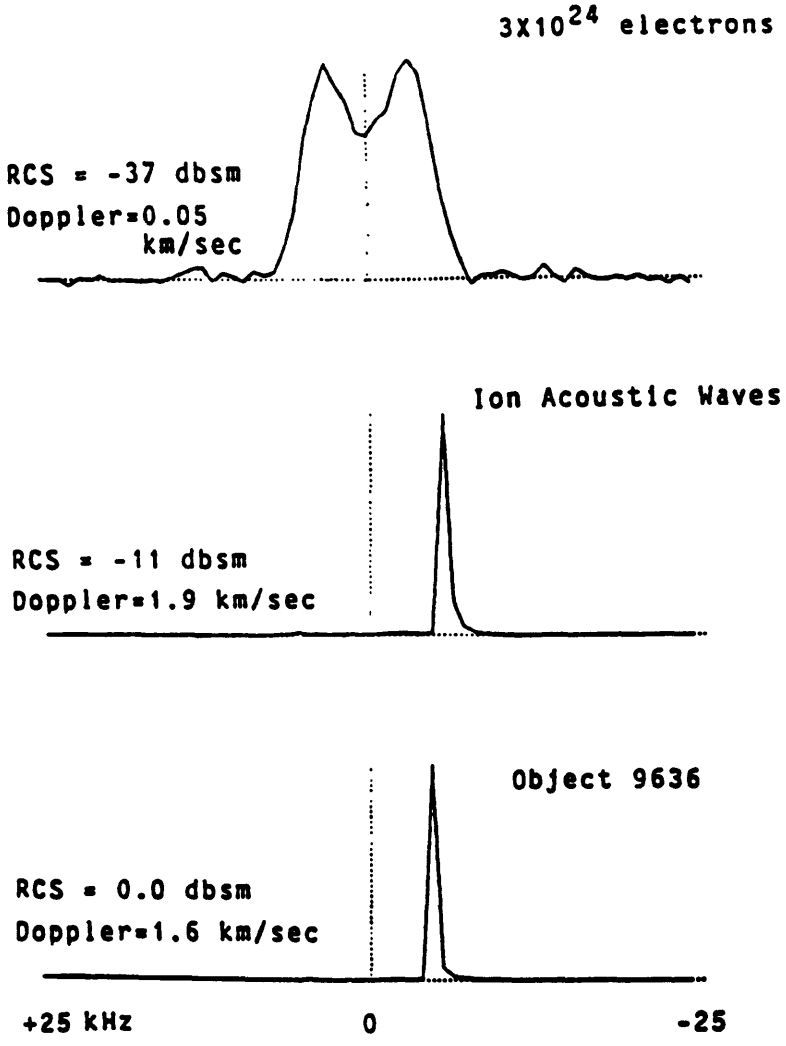

Figure 5-2: UHF Power spectrum of a) Normal incoherent scatter ion line; b) Enhanced ion line; and c) Spherical satellite #9636. The amplitude on each plot is self-normalized.

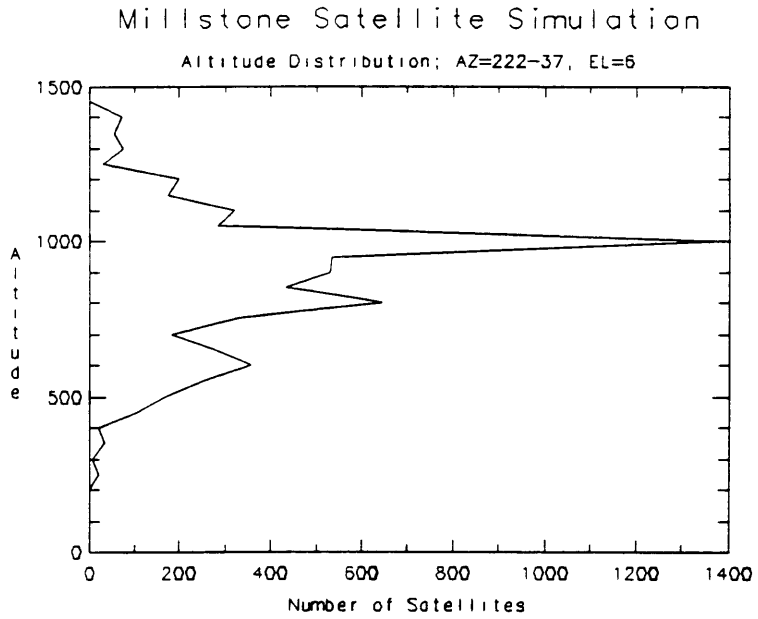

Figure 5-3: Altitude distribution of satellites in the Millstone Hill radar field-of-view for a 6° elevation angle.

Figure 5-3.

The majority of the satellite population exists at altitudes above about 500 km; layers of debris can be identified near 600 km and 800 km, with a well defined maximum near 1000 km. The distribution underscores the problem of removing hard target contamination: The Millstone Radar cannot diagnose the active auroral regions north of 60° latitude at altitudes less than 500 km. Thus we are forced to sample the active region of interest at altitudes where the greatest number of contaminants are located. A number of techniques utilizing the satellite catalog have been employed to distinguish satellite echoes from those of geophysical origin.

Specific Events One way to employ the catalog is to simply check specific records of the radar data containing coherent peaks suspected to be geophysical ERB returns. The time and location of a peak's occurrence can be checked against the catalog to determine if a satellite with the appropriate Doppler velocity was present. In applying this method one must be careful to properly define the uncertainty in the space-time window which must be specified for the coherent echo's location.

A single Millstone data record is typically constructed of power measurements which are integrated for 15–30 seconds, during which time the radar may scan up to five degrees in azimuth. Spatial range smearing due to the radar pulse length adds up to 150 km uncertainty in range. Additional error is introduced by the finite radar beamwidth; the large radar cross section of many satellites requires one to define the "effective beamwidth" as including the sidelobe pattern well beyond the common definition of the half-power width. For the Millstone Hill steerable UHF antenna, this means expanding the traditionally defined 1° beamwidth to some 2°–3°. The largest uncertainties in the azimuth, range, and time of the space-time window specified for a given echo are then, respectively, ± 5°, 150 km, and 30 seconds, enough time for a satellite to travel some 250 kilometers.

In reality, of course, the radar beam occupies only a small fraction of the total window at a given moment in time; to insure a fair check, however, the entire window must be specified for the satellite catalog to check a particular data record. The result is that the catalog often predicts the penetration of the relatively large space window by several hard targets within the 30 second record interval, even when no evidence of a corresponding coherent peak is seen in the data.

If the catalog predicts that no suitable satellites were present, one can at least be confident that the assumption of the peak's ionospheric origin has not been ruled out. While this use of the satellite catalog is perhaps the most obvious, the technique cannot provide definitive proof that a given radar echo was generated by the ionosphere because the satellite catalog is not 100% reliable.

The catalog is not completely reliable for several reasons. The large number of objects cataloged (over 7000 presently) makes it very difficult to provide frequent element set updates on all objects. The low altitude orbits occupied by the satellites penetrating the Millstone Hill radar beam degrade fairly rapidly, so that catalog

projections of the locations of some objects may be significantly inaccurate. Furthermore, there are numerous classified satellites not included in the catalog used for these studies. Finally, there is a population of uncataloged small orbiting debris.

Statistical Studies The uncertainties involved in applying the satellite catalog to check specific events limit the usefulness of that technique, as noted above. The factors that render the catalog fallible for selected records, however, become unimportant if one applies the catalog in a temporally statistical manner. A calculation of the distribution of low altitude targets ($\tau_{orbit} < 110$ minutes) passing through a defined space window over a period of 24 hours or so, will not depend significantly on the accuracy of a particular satellite's ephemeris data. Assuming they represent a small percentage of the total satellite population and exhibit a similar altitude distribution, classified objects no longer constitute a serious source of error, either. The contamination due to the uncataloged debris must be examined in more detail.

Only about five percent of the over 7000 space objects cataloged are active or working satellites. About 50% of the known objects orbiting the earth consist of fragments resulting from the breakup of artificial satellites. The primary causes of satellite breakups are propulsion related malfunctions and intentional detonation, although collisions are suspected for unexplained breakups as well [*Johnson*, 1985]. It is believed that the uncataloged population of fragments from these breakups may be up to 2.5 times greater than the total cataloged population [*Kessler*, 1985].

Statistical studies, however, will not be modified significantly by the presence of the orbiting debris for two reasons. The first is that the uncataloged population consists of fragments smaller than about 10 centimeters diameter. Objects of this size in the topside of the ionosphere are too small to cause greatly enhanced coherent echoes, particularly for radar wavelengths much greater than the fragment diameter. The second reason is that the distribution of fragments generated by a breakup re-

mains centered in height at the original orbit altitude. Thus the shape of the altitude distribution changes very little; only the number of objects varies.

Doppler Shift Discrimination The catalog has been employed to calculate the passage of satellites through an azimuth window which is left "open" for a sufficient period of time to allow several orbital revolutions, typically 24 hours. In Figure 5-4a a histogram of the number of cataloged objects is plotted as a function of their line-of-sight velocity to the Millstone radar for a low elevation azimuth scan between 342°–27° over a 24 hour period. The spikes located at about ±6 km/sec are due to the large population of satellites in so-called "polar" orbits, high inclination orbits between 800–1000 kilometers altitude. The radar measures a large line-of-sight velocity as it scans to the north and detects these objects as they pass over the polar cap. The velocity measured by the radar is actually determined from the Doppler shift of the scattered signal received by the antenna. For the backscatter geometry employed here, the shift in kHz is given by $\Delta f = 2v/\lambda$, where v is the satellite velocity in km/sec and λ the radar wavelength in meters. A simple conversion for the 68 cm wavelength used by Millstone Hill is $\Delta f \simeq 3v$.

Figure 5-4b shows the distribution of coherent peaks observed at Millstone Hill for an experiment run 13–15 January, 1988 scanning through the same azimuths as the simulation 5-4a. A comparison of the two nearly identical distributions suggests that many, if not all, of the peaks observed during this experiment were caused by satellites penetrating the scanning radar beam. Magnetic conditions during 48 of the 72 hours of data analyzed were very disturbed; Kp values of 7 or higher were registered for a 9 hour period, and remained at or above 6 for 15 consecutive hours during the middle period of the experiment.

The consideration of magnetic activity is important because of its correlation with field-aligned currents. The Kp indices referred to here are global classifiers of the am-

plitudes of magnetic variations derived every three hours based on observations from a number of stations located over a wide range of latitudes. The quasi-logarithmic scale varies from 0 to 9 in 27 increments; the scale is skewed towards the low end of these values in that magnetic fluctuations corresponding to 3 or less occur 90% of the time, whereas fluctuations of Kp=6 or greater represent less than 1% of the total distribution [*Mayaud*, 1980]. Given the sustained periods of very high activity occurring during the experiment of JAN88, we might expect a correspondingly high intensity of field-aligned currents, producing significant numbers of ERB events. Reasons for the apparent lack of observed ERB in this experiment will be discussed shortly.

A second experimental simulation and corresponding observations are presented in Figure 5-5. As in Figure 5-4, the signature of the polar orbiters at ± 6 km/sec is evident in both 5-5a and b. However, in Figure 5-5 an even larger number of peaks were observed between ± 1–2 km/sec, the ion sound speed regime in topside ionospheric plasmas. This remarkable feature has not been observed in velocity distributions constructed from other Millstone Hill radar experiments. Clearly the satellite catalog does not predict the large population of peaks observed at these Doppler velocities. If this data set represents a statistical average, we can feel confident that a portion of the observed ion acoustic peaks were generated by ionospheric processes.

The satellite simulations shown in Figures 5-4a and 5-5a were generated by continuously monitoring all azimuths within a defined window simultaneously, in so-called *open window* simulations. Because the simulated coverage area is large, 12 hours ($t \geq 6\tau_{orbit}$) is a sufficient time to run the open window simulation. Simulating longer periods of time does not affect the shape of the calculated distribution of detected hard targets; it only increases the number of "hits" in the radar beam.

In an actual experiment, of course, the beam scans through the window and monitors only a small fraction of the total azimuth extent at any moment in time. The

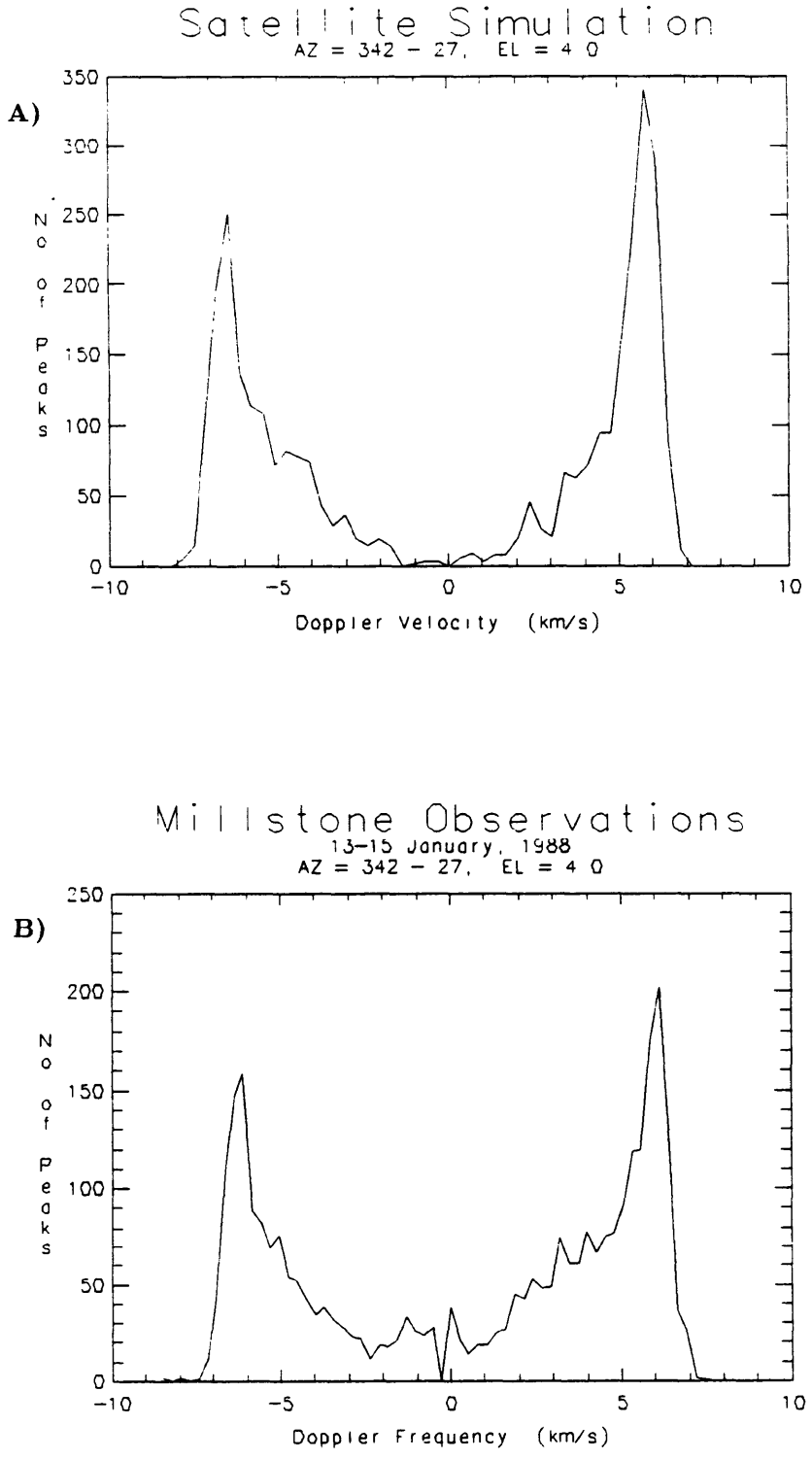

Figure 5-4: Distribution of Doppler velocities for a) satellites penetrating the radar beam between 342°–27° AZ, 4° EL, and b) Actual observations from 13–15 Jan. 1988 for the same pointing angles.

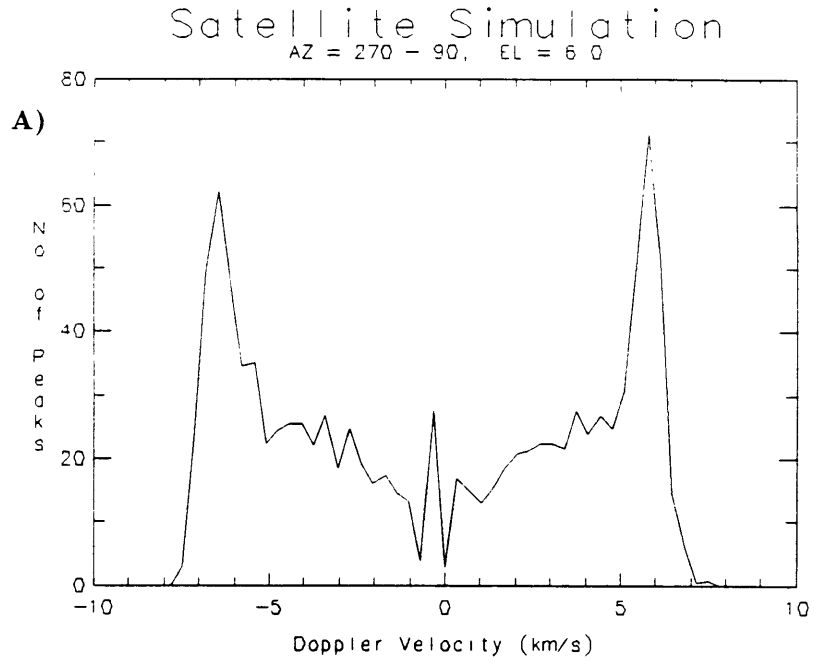

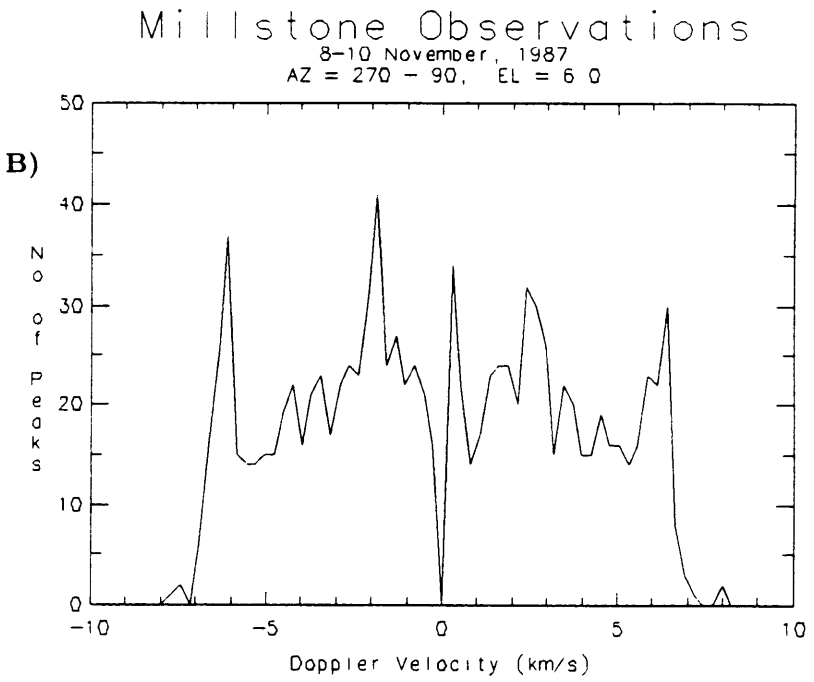

Figure 5-5: Distribution of Doppler velocities for a) satellites penetrating the radar beam between 270°–90° AZ, 6° EL, and b) Actual observations from 8–10 November 1987 for the same pointing angles. The large number of peaks observed at ion acoustic velocities is not predicted.

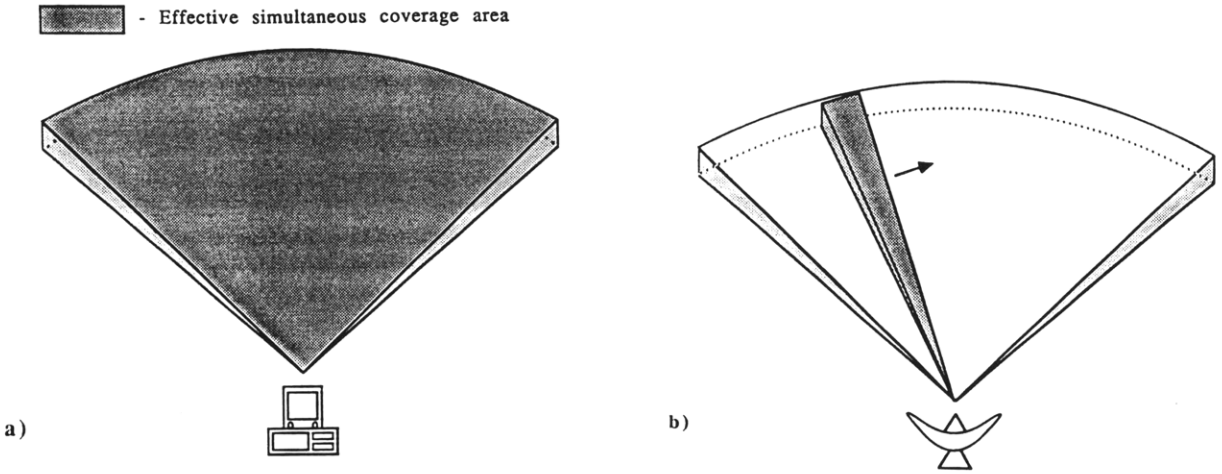

Figure 5-6: Graphical illustration of procedures used for a) satellite simulations where the entire space window is continuously monitored, and b) actual data acquisition via scanning radar beam in experiment.

difference between the simulations shown thus far and actual experiments is illustrated graphically in Figure 5-6. Hence, the number of satellites actually detected in a 12 hour observational period is much smaller than the number "seen" by the catalog for the same 12 hours, and a comparison of the corresponding observed distribution may not be statistically valid.

The minimum time required for a valid statistical comparison of observed and simulated coherent peak velocity distributions was determined by simulating a computer radar beam scanning through a dynamic satellite field. In the simulations, the table of satellites passing through the azimuth window were sorted according to time, and a radar scan was initiated at a given time and starting position to sample the satellite data base. The simulated scan consisted of a $2° \times 2°$ wide beam which was swept $10°$/min in azimuth, the same azimuth scan rate used in most experiments at Millstone Hill. This process was repeated several times using different initialization

parameters for periods of 12, 24, and 48 hours.

It took 4–5 times more scanning hours to acquire as many targets as the corresponding open window simulation. The 12 hour simulations produced distributions which were usually similar to the open window distribution, but in some cases relatively large disparities were evident. The 24 hour simulations improved results. None of the 24 hour distributions, for example, predicted more peaks at ion acoustic velocities than at polar orbiter velocities, as was observed in the NOV87 experiment. Nevertheless, deviations from the open window distribution were large enough to discourage quantitative comparison. After 48 hours, however, the scan simulations matched the shape of the open window results nicely, regardless of starting time or position within the satellite data base; increasing the time further simply produced more events without noticeable distortion of the distribution.

The data sets used to produce the observed distributions presented in Figures 5-4b and 5-5b contain at least 60 continuous hours of radar observations, and should therefore satisfy the statistics of the satellite catalog simulations. Comparing the simulations with the observed distributions we conclude that a number of the coherent peaks observed at ion acoustic velocities between 1–2 km/sec in the NOV87 experiment result from geophysically induced ERB. The levels of global magnetic activity during the period varied from quiet to unsettled to moderately disturbed ($0 < Kp \leq 5^-$). Extrapolating the number of ERB events occurring during this moderate activity to the extremely disturbed periods of the JAN88 experiment, we would expect to find much stronger evidence for geophysical ERB in the January velocity distribution. The lack of such evidence can be explained by considering the results of a statistical analysis of a third experiment.

Altitude Discrimination Coherent echo distributions were constructed from approximately 80 hours of data acquired during an experiment on 6–10 March 89, which

was known to contain magnetically disturbed periods. The velocity distribution of the enhanced echoes observed during the experiment, however, very nearly matched the corresponding distribution generated by the satellite catalog. The observed altitude distribution of the enhanced returns, shown in Figure 5-7, also looks quite similar to the simulated satellite distribution shown in Figure 5-3, except at the lowest altitudes, where a surprisingly large number of peaks are observed in range gate 10, corresponding to 330 km altitude.

The number of orbiting objects at altitudes of about 300 km or less represents less than .5% of the total satellite population. In the observed distribution, however, such events account for nearly 1.5%. For this experiment that translates into precisely 18 events, a small number which is perhaps not statistically robust, despite 80+ hours of observations. The significance of the low altitude anomaly increases when one recognizes that the number of events near 300 km is comparable to, or greater than the number of peaks detected at altitudes of 500 and 540 kilometers, respectively. An examination of the spectral characteristics of each low altitude enhancement provided further evidence of a geophysical source for some of the enhancements.

Satellites at low altitudes must travel faster than orbiting objects at higher altitudes; a satellite simulation for the 6–10 March azimuth scans shows that about 85% of the time, the line-of-sight Doppler velocity detected by the radar from these objects exceeds 4 km/sec, and is often higher than 7 km/sec. In the March experiment, however, 5 of the 18 low altitude enhanced peaks exhibited Doppler velocities at the local ion acoustic speed, usually between 1 and 2 km/sec in the F region. This is almost double the expected percentage of ion acoustic enhancements, and seems unlikely to be a random occurrence caused by hard targets. The occurrence of these events with regard to magnetic activity and other geophysical considerations is also indicative of ion acoustic enhancements through natural processes.

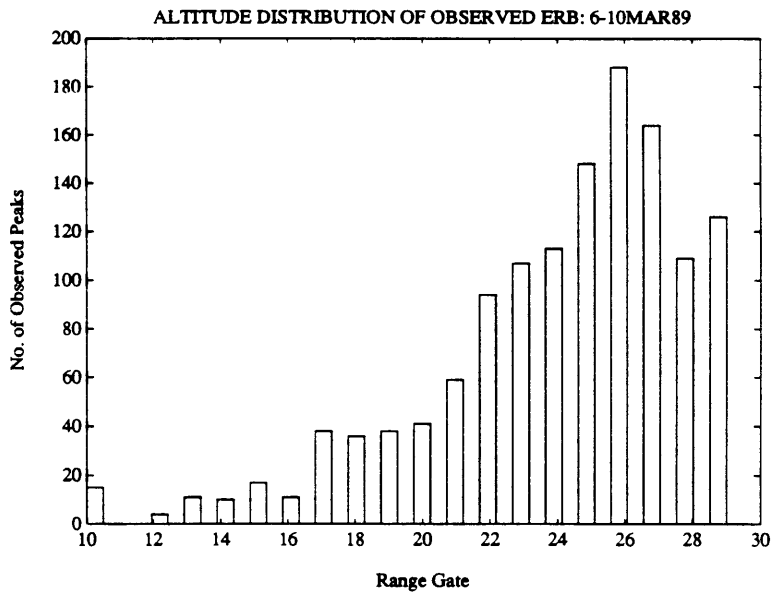

Figure 5-7: The altitude distribution of observed coherent echoes from the Millstone 6–10 March 1989 experiment. Altitude is scaled by range gates, which are separated by 40–50 kilometers. Some gate numbers followed by their corresponding altitude are: 10/330, 15/500, 20/700, and 25/975.

This March experiment time period was very interesting magnetically, being more disturbed than the 8–10 NOV87 period, but significantly less disturbed than the monster storm levels recorded during 13–15 JAN88. The hourly AE index is plotted for the duration of the experiment in Figure 5-8. The AE index provides a useful measure of auroral magnetic activity. The figure shows that March 6–7 were moderately disturbed before activity decreased steadily through the latter part of the 7th and March 8. At 18:00 UT on the 8th a major storm commenced; disturbance levels decreased soon after the major impulse, but remained active throughout most of March 9 when another surge of activity occurred, lasting just til 24:00 UT.

The height of the maximum density in the F region, $hmF2$, is closely related to the magnetic activity (see Figure 5-9). Under quiet conditions, $hmF2$ exhibits a regular diurnal variation, descending during daylight hours as photoionization builds up the plasma density at lower altitudes, and ascending again after dusk when recombination processes neutralize the low altitude plasma more rapidly. A typical variation

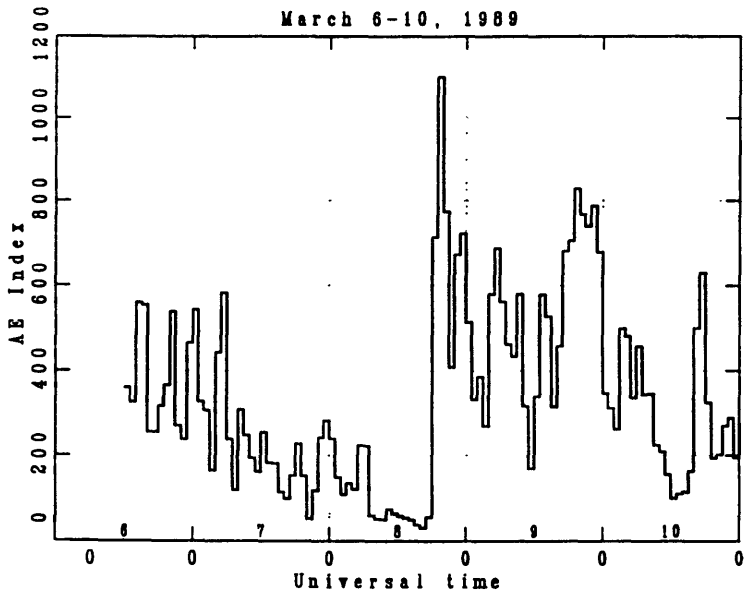

Figure 5-8: Values of magnetic index AE during the magnetic disturbances of 6–10 March, 1989. Note the sudden storm commencement at 18:00 UT on March 8 [after *Buonsanto et al.*, 1990].

of this nature is evident during the period of decreasing magnetic activity spanning March 7–8. Under magnetically disturbed conditions $hmF2$ serves as an excellent indicator of the passage of the mid-latitude electron density trough and the equatorward expansion of the auroral oval [*Buonsanto, et al.*, 1990]. In the trough itself, the $hmF2$ value increases sharply, as occurs in the early morning hours of March 7, March 9, and March 10.

The low altitude ion acoustic enhancements occurred at 7MAR-1:44 UT, 9MAR-3:34 UT, 9MAR-11:52 UT and 10MAR-3:00 UT. Their positions are indicated on Figure 5-10, which is a plot showing the variation of the peak ionospheric density, *NMF2*, as a function of time and latitude. All the enhanced peaks occur either in the ionospheric trough or on the trough's equatorward edge in a region of strong density gradients associated with field-aligned Birkeland currents [*Ungstrup, et al.*, 1986]. Except for the event at 11:52 UT on March 9, all the events occur just prior to the arrival of the trough over Millstone Hill. The event at 11:52 UT is actually occurring under similar geophysical conditions, except that it is located on the edge

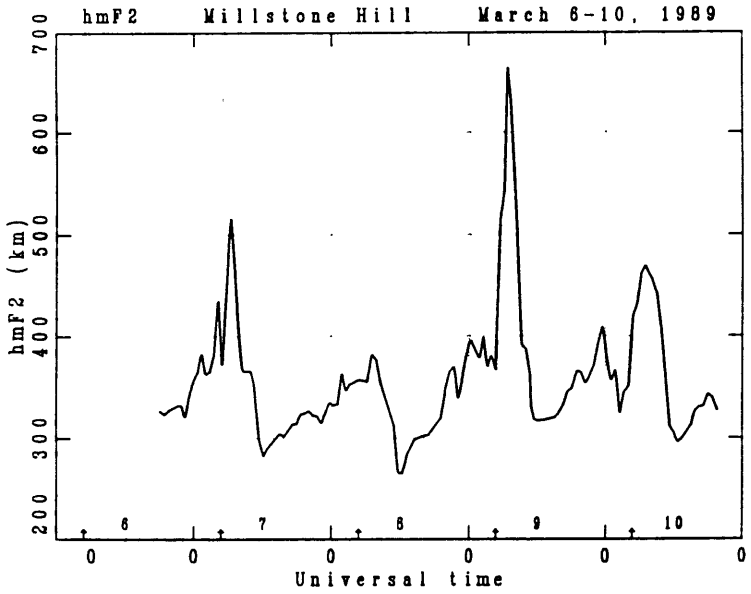

Figure 5-9: The height of maximum electron density in the ionosphere for the 6–10 March period. The sharp increases in altitude correspond to the approach of the mid-latitude trough [after *Buonsanto et al.*, 1990].

of a receding, rather than approaching, density depletion.

The approach of the trough signals the expansion of the auroral oval and the penetration of large electric fields to lower latitudes. These fields are responsible for the very large westward $\mathbf{E} \times \mathbf{B}$ plasma drifts observed in the early morning on March 9. The enhanced low altitude ion line detected at 3:34 UT on March 9 is shown in Figure 5-11; the large shifts evident in the normal IS spectra at higher altitudes correspond to westward drifts of up to 1.3 km/sec. All-sky images revealed that prominent red aurora were present north of the Millstone Hill radar at this time, in the same location where the ERB occurred; later in the morning a stable red auroral (SAR) arc persisted to the north for about two hours [*M. Buonsanto*, private communication, 1991]. These geophysical signatures verify the presence of auroral features at latitudes as low as 44° on March 9. Similar features, though not as intense, were present during the early morning hours of March 7 and 10 as well. By contrast, the post-dusk period on March 7/8 did not display a well-defined trough or auroral characteristics. The density depletion evident after midnight on this day

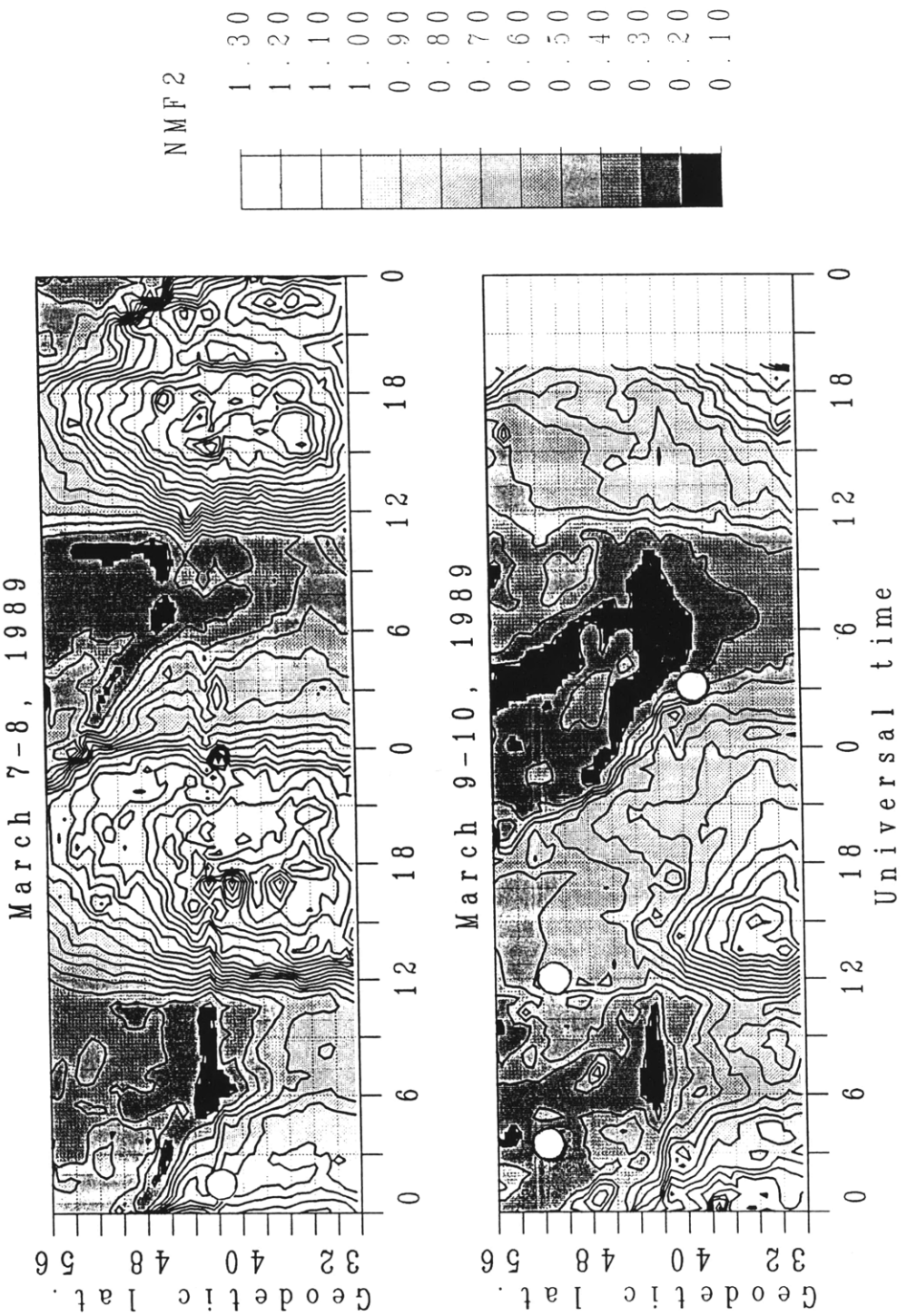

Figure 5-10: Variation of peak electron density with latitude. Low altitude ERB events are indicated with white dots. Low density regions are shaded black [after *Buonsanto et al.*, 1990].

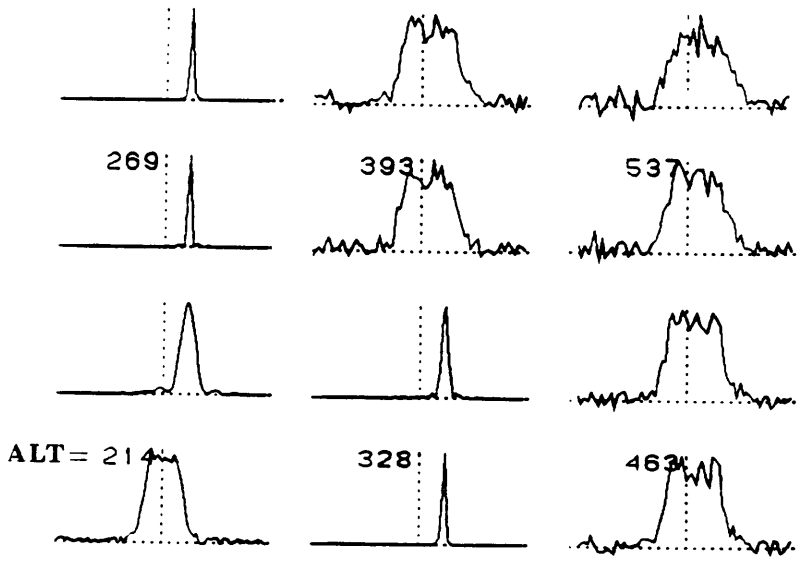

Figure 5-11: Ion line enhancement observed with the Millstone Hill UHF radar at 03:34 UT on 9 March 89. At higher altitudes the shifted spectra give evidence of large westward $\mathbf{E} \times \mathbf{B}$ drifts.

is associated only with the normal diurnal decrease occurring after sunset. No low altitude ion acoustic ERB events were recorded during this time period.

We have established the presence of active auroral features during the periods when low altitude ERB events were observed in the 6–10 March experiment. These events are attributed to the enhancements of ion acoustic waves in the presence of naturally occurring intense field-aligned currents. Normally the Millstone Hill Radar can diagnose these remote high latitude active regions only at altitudes above 500 km, where the large satellite population makes unambiguous identification of ERB events difficult. During the magnetic disturbances of March 6/7, March 8/9 and March 10, the equatorward expansion of the auroral oval carried it to within a few degrees of Millstone's latitude. This made it possible for low elevation-angle azimuth scans to sample the active region at much closer ranges, and correspondingly lower altitudes, than normal. The low altitude ERB events were then relatively easy to separate from hard targets because so few satellites occupy these very low altitude orbits. The variability of the ionosphere played an important role in interpreting the results of

the distribution studies for this experiment.

The level of variability in the 13–15 JAN88 experiment was about an order of magnitude greater than that experienced during 6–10 MAR89. By extending the auroral dynamics arguments used to explain the results of the MAR89 experiment, we can arrive at a rational explanation for the total lack of statistical evidence of geophysical ERB during the JAN88 experiment. In MAR89, ionospheric variations were characterized by brief periods of intense magnetic activity resulting in the equatorward expansion of the the auroral oval to latitudes slightly north of Millstone Hill. The periods of intense activity were then followed by somewhat longer periods of decreased activity, providing a relaxation period for the ionosphere to nearly return to its normal structure.

After the first day of the 13–15 JAN88 experiment, however, periods of extreme activity were sustained for many hours. The auroral region, containing the intense current activity critical for ERB excitation, actually passed to the south of Millstone Hill and did not recover to its usual latitudes during the duration of the experiment. The radar scan cycle employed, a 4° elevation-angle, limited azimuth scan to the north, was not advantageous to the detection of ERB under these circumstances. Zenith measurements or even scans to the south of Millstone are appropriate for such studies under very disturbed conditions. In conclusion, ERB events were not detected in the JAN88 experiment because the auroral zone passed to the south of Millstone Hill due to extreme levels of magnetic activity, while the radar continued to scan at low elevation angles to the far north.

Finally, a large data set acquired on 6–10 October 86 was analyzed by the same statistical technique. The observed velocity distribution closely resembled the satellite distribution, similar to the comparison shown in Figure 5-4. Furthermore, an analysis of the altitude distributions yielded no evidence of anomalous ERB events. The global

Kp index indicated that the period was one of the most quiet imaginable, with 60 of the 87 observing hours having Kp of 1^+ or less and a maximum Kp of 3^- occurring for one 3-hour period. Under these conditions, intense current activity is not expected at any latitude within Millstone Hill's field-of-view. Consistent with that interpretation, we conclude that the lack of evidence of ERB events in the statistical analyses for this experiment indicates simply that no appreciable ERB events occurred during this time period because of the very low levels of magnetic activity.

5.2.2 MICAD Experiments

Beginning in April 1989, a series of multi-diagnostic experiments, known as MICAD, involving the MIllstone Hill UHF radar, a subset of the CANOPUS system of instruments (BARS radar, magnetometer array, meridian photometers) and the DE-1 satellite was conducted to provide additional information about ion acoustic radar backscatter enhancements due to ionospheric processes. In these experiments, as illustrated in Figure 5-12, the Millstone Hill radar was used to track the geomagnetic field line above the DE-1 satellite as it flew through perigee within the radar's field of view; CANOPUS instruments were utilized as diagnostics of the background ionosphere. Ultimately, the goal was to simultaneously detect the signature of large, field-aligned ionospheric currents with remote sensors (radars, etc.) and in situ instruments aboard DE-1.

Beginning in April 1989, a total of seven MICAD overflight experiments were conducted on 4/9, 5/2, 5/22, 6/5, 6/19, 8/8, and 8/29. During the MICAD experiment on 22 May 1989, the Millstone Radar detected a 7 dB enhanced backscatter return at the ion acoustic frequency at 23:57:46 UT; the power enhancement at 1000 km is shown in Figure 5-13. The power plot shows a distinct F region trough at the latitude of the ERB event. In the scan shown in the figure the radar moved

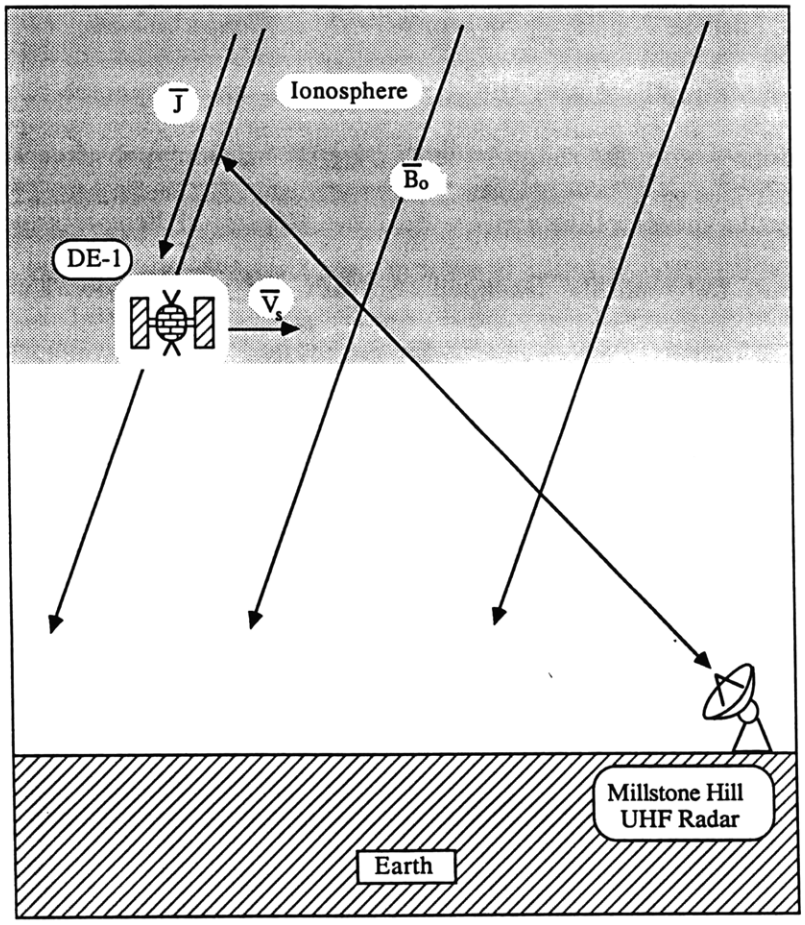

Figure 5-12: Conceptual design of MICAD experiments. Remote diagnostics and in situ instruments were to obtain simultaneous measurements on the same magnetic field line.

from AZ=289° at 23:54:52 UT to AZ=343° at 23:59:08 UT. The enhancement occurred at an azimuth of 332°. The DE-1 satellite passed through the same region 30 seconds later and recorded an in situ magnetometer fluctuation corresponding to a field-aligned current density ≥ 50 μamps/m^2 [*J. Slavin*, private communicaton, 1989]. The magnetometer trace and the enhanced UHF radar spectra are shown in Figure 5-14. The decrease in the magnitude of DBPHI evident just after 23:57:00 UT in the figure indicates the satellite's entry into the Region II field-aligned current system. The boundary between the Region I currents and the Region II currents is reached at about 23:58:10 UT, when the $\sim$ 50 μamps/m^2 current spike was detected. The onboard magnetometer continued to exhibit large fluctuations until about 23:59:00 UT; two of the additional fluctuations at 23:58:20 UT and 23:58:40 UT correspond to current densities in excess of 25 μamps/m^2. Because the radar was actually tracking about 30 seconds ahead of the satellite's position, the measurements cannot be classified as truly simultaneous. However, this experiment gives firm evidence of intense field-aligned currents associated with the occurrence of ERB near the ionospheric trough as was suggested by FOS88.

An examination of data from two consecutive passes of the DMSP-F8 satellite (the first 42 minutes prior to, and the second 56 minutes after the DE-1 overflight in the same longitude band) reveal that the region producing the enhanced radar backscatter was characterized by localized intense, soft (E $\leq$ 1 keV) electron precipitation features. Comparison of the measured electron and ion fluxes show that current densities in excess of 60 μamps/m^2 were detected on the first pass [*W. Denig*, private communication, 1989]. Data from this pass formed the basis for deriving the suprathermal contribution to the electron distribution function utilized in numerical calculations in Chapter 7 (see Figure 7-7).

Particle flux spectrograms from a northern polar pass of the NOAA-10 satellite

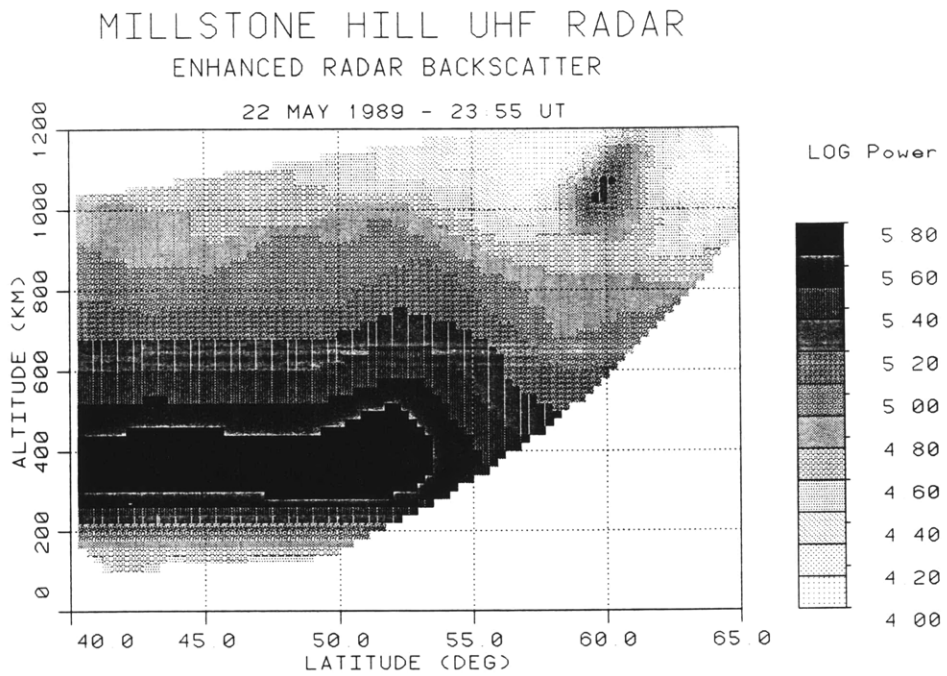

Figure 5-13: Power enhancement observed during May 22 MICAD experiment. The 7 dB enhancement is located at 1000 km altitude on the edge of the ionospheric trough. A two msec radar pulse was used in the scan.

exhibit a sharp local maximum in the low energy electron flux at the same latitude and only 8 minutes prior to the DE-1 satellite and Millstone Hill radar observations. A map illustrating the geographic and temporal relationship of the various measurements is shown in Figure 5-15. These in situ data establish the presence of discrete low energy particle precipitation events carrying large current densities in the region of enhanced UHF radar backscatter.

It should be noted that limited particle flux information is available from the DE-1 satellite. The electron flux instrument onboard is no longer functional. The energy spectrum of ions was monitored, but no signature was evident in association with the large magnetometer variations [*W. K. Peterson*, private communication, 1989]. This is consistent with the DMSP data, where the energy flux of the electron population increases dramatically while the ion flux remains essentially unchanged. Both measurements indicate that the currents are being carried by suprathermal

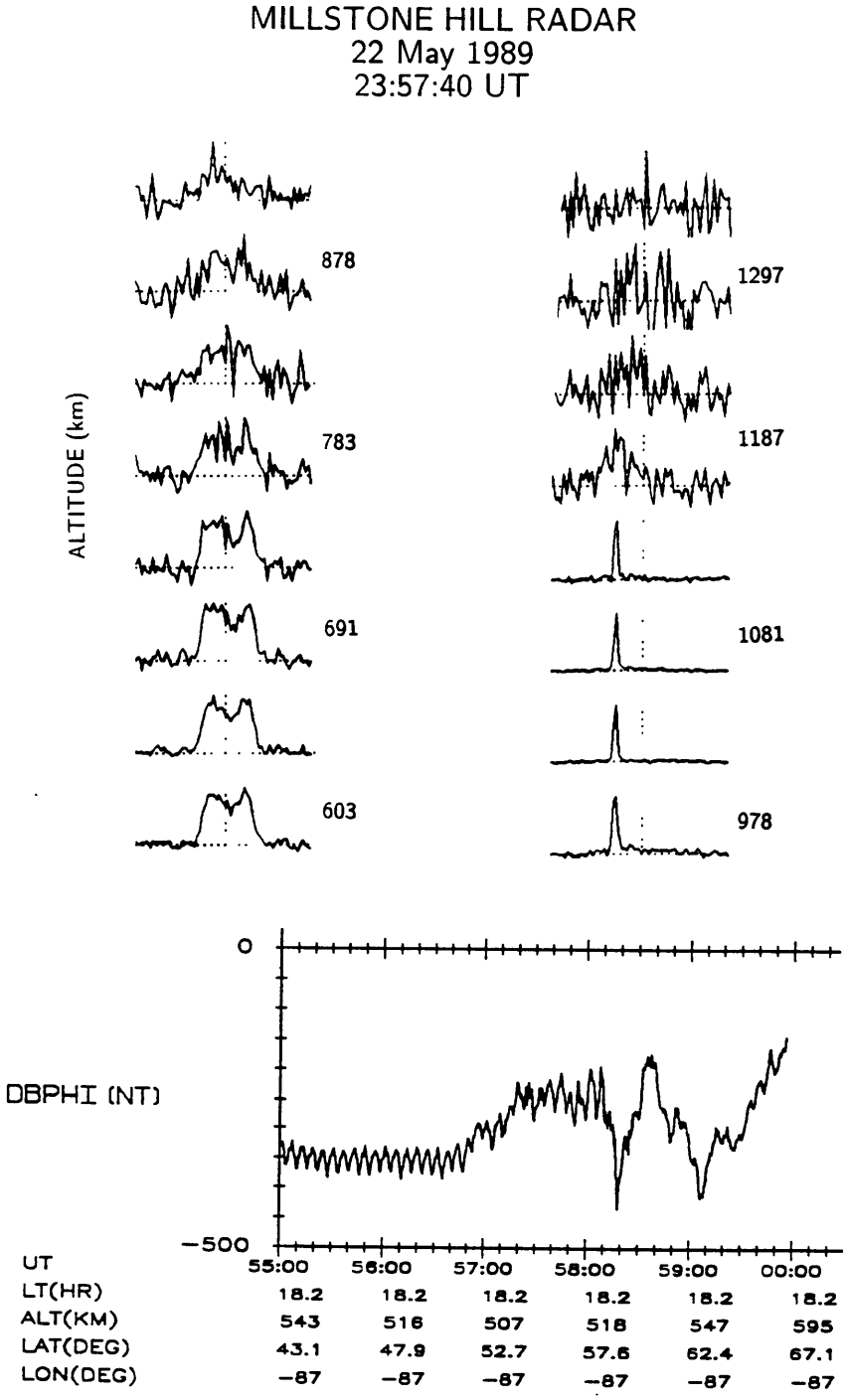

Figure 5-14: Power spectra of ion acoustic ERB observed with the Millstone Hill UHF radar and the corresponding magnetometer trace of the DE-1 satellite. Magnetic fluctuations (DBPHI) are in units of nanotesla.

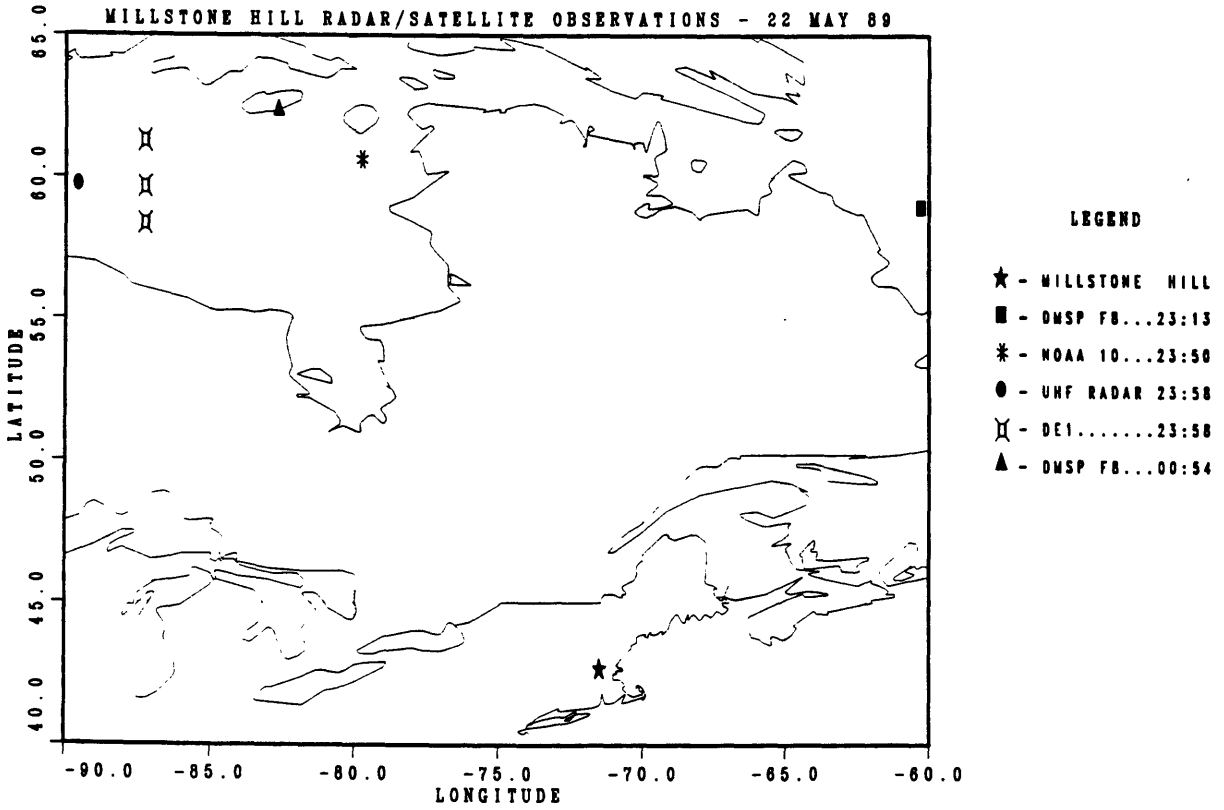

Figure 5-15: Map showing geographic relationship of multiple satellite measurements of intense field-aligned current activity, UHF ion acoustic ERB, and the Millstone Hill radar.

electrons rather than ions.

Measurements from the CANOPUS diagnostic group of instruments were of limited application in this particular MICAD experiment. The observations were outside the field-of-view of the BARS radar system, and the local time was too early to acquire all sky camera images of visible airglow or photometer data. The meridional magnetometer chain (MARIA) approximately 320 km west of the UHF ERB observation was operating, and the magnetometer traces from the nearest stations are shown in Figure 5-16. The ground stations show a reasonable level of activity (Kp=4) prior to the Millstone/DE-1 observations, but conditions are relatively quiet during the actual overflight (about 2 hours after start time). Global magnetic activity usually serves as an indicator of intense field-aligned currents, but it does not constitute a prerequisite for their occurrence. Johnstone and Winningham [1982] reported several

satellite observations of suprathermal electron bursts carrying field-aligned currents in the auroral zone during very quiet magnetic conditions.

The satellite catalog was consulted for the presence of hard targets in the scattering volume during the 30-second integration period in which the ion acoustic ERB event was recorded. A generous scattering volume was assumed, using the actual elevation and azimuth angles of the radar $\pm 2°$, to minimize the uncertainties due to errors in the catalog predicts. Three candidates were found. Of these three, two were expected to produce large line-of-sight Doppler shifts of about 6 km/sec. The other possible candidate's Doppler velocity was in the opposite direction of the observed phase velocity of the enhanced ion acoustic peak. Clearly, none of the predicted hard targets could have caused the asymmetric UHF power spectrum observed in this MICAD experiment.

5.2.3 Observation of ERB in Zenith Experiments

As has been established, the contamination due to satellites in the investigation of ERB is a serious problem in general. However, hard target signatures can be filtered out effectively by pointing the radar directly overhead. In the zenith position the beam is nearly transverse to the direction of motion of satellites penetrating the scattering volume, and their associated Doppler shifts are thus restricted to nearly zero magnitude. Satellite catalog simulations based on a $2° \times 2°$ wide beam show that the maximum observable line-of-sight velocity possible in such experiments does not exceed 250 m/sec. Zenith observations of spectral peaks with greater Doppler shifts (*e.g.*, F-region ion acoustic speed: $C_s \sim$1-2 km/sec) can then be attributed to geophysical sources.

Figure 5-17 shows an observation of ion acoustic wave growth acquired with the Millstone Hill 67-meter fixed position zenith antenna. The Doppler shift of the peak

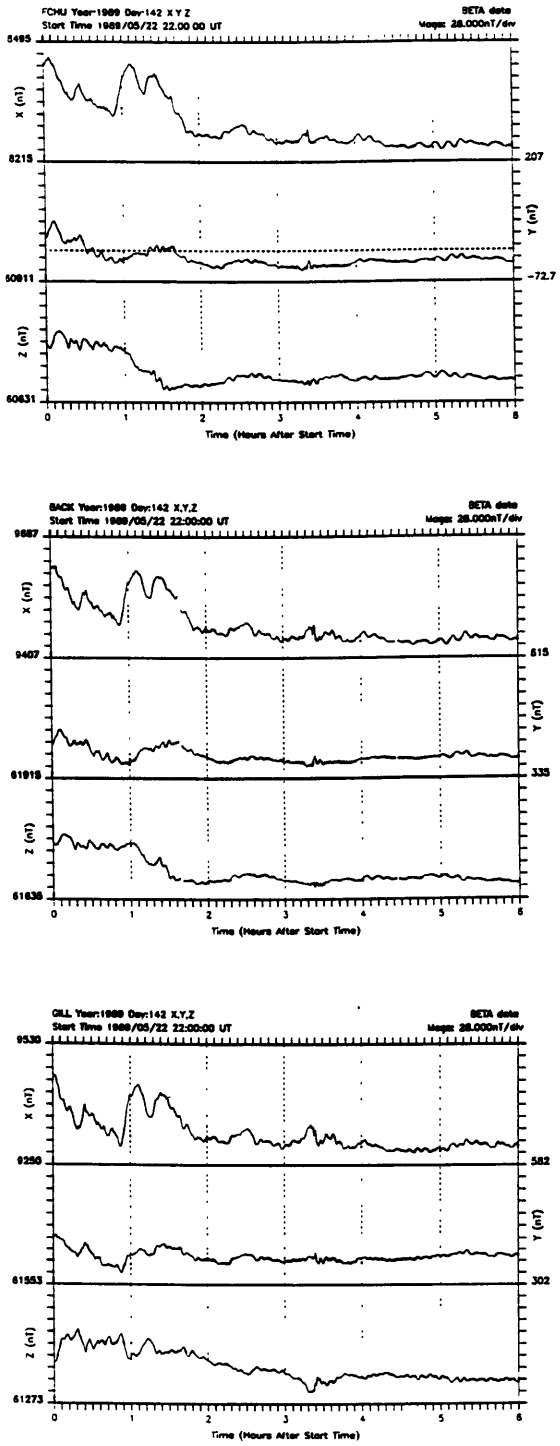

Figure 5-16: Magnetic variations recorded by the CANOPUS chain of magnetometers during the May 22, 1989 MICAD experiment. The DE-1 and Millstone Hill observations of ERB were recorded at 23:58 UT, during the relatively quiet period nearly two hours after the start time on the plots.

corresponds to a 1 km/sec velocity, about four times greater than the maximum observable shift from actual satellites. In addition, the enhanced return is distributed in altitude to a greater extent than is possible for an orbiting object given the 150 km pulse smearing along the radar beam. This zenith observation, reported by FOS88, was taken as proof that a portion of the Millstone ERB returns cannot be caused by orbiting objects.

The scan cycle for the radar in this experiment consisted of 4 consecutive zenith measurements followed by a complete elevation scan, 2 more zenith records, and a 180° low elevation-angle azimuth scan. Only six minutes out of every hour are spent in the zenith position, and only half that time is used to diagnose the high altitude region above 700 km. Unfortunately, the spectra shown in Figure 5-17 represent the last zenith measurement preceding the beginning of an elevation scan lasting six minutes. When the radar returned to the zenith position, the echoes were gone.

Observations like this at Millstone Hill are rare for two reasons. As was noted previously, the enhancements are thought to be associated with intense field-aligned currents. While such events are not extraordinary at auroral latitudes, they occur at mid-latitudes very infrequently, approximately 10–15 days a year based on the Kp magnetic index during the event shown here [*Mayaud*, 1980]. On those days when the general levels of disturbance are sufficient, the phenomenon directly over the radar may last for only minutes or seconds and be missed entirely [*Rietveld et al.*,1991], as was nearly the case in this experiment.

Typically only a small amount of Millstone's total data acquisition time is used for zenith observations. Few dedicated zenith experiments have been conducted at Millstone Hill in the past; two separate 24-hour experiments run recently yielded no significant results. The zenith data obtained in most previous experiments consists of a few local measurements made once or twice per hour in between azimuth and/or

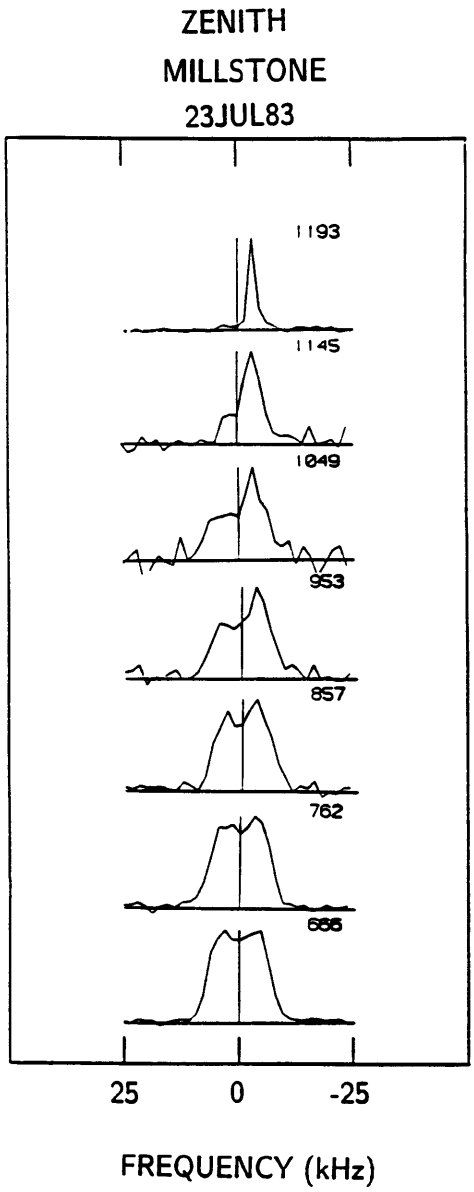

Figure 5-17: Millstone Hill zenith observation of ion acoustic ERB. The frequency offset corresponds to a velocity of 1 km/sec. [after FOS88].

elevation scans. Considering the low occurrence frequency of the geophysical event and the sparse number of zenith observations, the probability of detecting ion acoustic enhancements directly above Millstone Hill is small; zenith experiments conducted solely for that purpose may not provide an effective approach for investigating ERB at mid-latitudes.

5.3 Summary

An attempt has been made to provide conclusive evidence of geophysically-produced enhanced ion acoustic radar backscatter observed at Millstone Hill.

Because of the spectral similarities of satellites and enhanced ion acoustic waves, it is difficult to distinguish individual measurements unambiguously. Satellite simulations have been employed to make statistical comparisons with large data sets. Results from four types of experiments have been presented. Under extremely disturbed and extremely quiet conditions no ERB events were detected by the statistical analysis. In the quiet case there are most likely no occurrences of ERB. In the very disturbed case, however, pointing the radar to the north proved ineffective because of the auroral region's passage to the south of Millstone. ERB events were found at low altitudes during a lesser storm period when the auroral oval expanded to within a few degrees north of Millstone. These events have been attributed to the current-driven enhancements of ion acoustic waves in the temporarily nearby auroral zone. Finally, a moderately disturbed period was examined. The velocity distribution exhibited many more peaks at ion acoustic frequencies than predicted by the satellite catalog. These peaks are believed to represent geophysical ERB events occurring at relatively high latitudes in the usual auroral zone.

Through a series of multiple diagnostic experiments, we have established the association of enhanced backscatter events with intense field-aligned currents. In one case,

a nearly simultaneous measurement of UHF ERB and a field-aligned current carried by suprathermal electrons were obtained. Data from other satellites confirmed that the region contained large fluxes of low energy electrons, and that such conditions persisted for tens of minutes. These soft precipitating electrons are believed to play an important role in the generation of ion acoustic ERB.

Finally, the utility of zenith-pointing experiments was exploited to filter out hard target contamination while acquiring ion acoustic ERB. A single event has been identified with a Doppler shift of 1 km/sec, the local ion sound speed in the plasma. Satellites passing through the beam exhibit Doppler shifts of less than 250 m/sec. These measurements are rare at mid-latitudes because intense field-aligned currents occur there very infrequently (perhaps briefly on 10–15 days/year during solar maximum), and the radar is not usually pointed in the zenith direction while acquiring data. Results from two 24-hour zenith experiments yielded no evidence of ion acoustic ERB.

Chapter 6

ERB Observations from Other Radar Sites

The existence of geophysically induced enhanced coherent radar backscatter from the topside ionosphere was first reported by FOS88 based on a study of "hard target" like returns observed with the Millstone Hill UHF Radar as described in Chapter 5. The enhancements are believed to be associated with intense field-aligned currents in the high latitude ionosphere. This high-latitude region is normally accessible to the Millstone Hill radar beam at very large aspect angles relative to the geomagnetic field, effectively limiting the range extent over which the field-aligned echoes may be observed and leading to ambiguities (with actual hard targets) in the data interpretation for individual coherent echo events. The locations of the EISCAT and Sondreström radars (see Table 4.1) suggest that more favorable ERB observing conditions may exist at those sites. Presented here is a brief overview of significant observations and experiments involving these radars which confirm and extend the known characteristics of ERB first recognized at Millstone Hill.

6.1 Observations at EISCAT

The EISCAT (European Incoherent SCATter) Scientific Association operates a tristatic UHF radar system consisting of a 933 MHz 2.5 MW radar located at Tromsø, Norway (69.7°N lat, 19.2°E.long) and two remote receivers at Kiruna, Sweden (67.8°, 20.4°) and Sodankylä, Finland (67.4°, 26.6°) . The three sites utilize identical parabolic antennas 32 meters in diameter to simultaneously determine full three-dimensional vector velocities at selected heights in the ionosphere. In addition to the UHF radar, a 224 MHz radar using a 40×120 m parabolic cylinder antenna is located at Tromsø, providing multi-wavelength measurement capability locally.

6.1.1 Initial Statistical Approach

The investigation of ERB at EISCAT was first undertaken by Schlegel and Moorcroft [1989] who applied a statistical approach, similar to that used at Millstone Hill, to 73 hours of data acquired with the radar pointed up the local magnetic field line (AZ=182°, EL=77.5°). EISCAT regularly runs so called *Common Programs* for data acquisition which employ this radar look angle for geophysical reasons; such data constitute a majority of the available data base. Attempting to discriminate geophysical events from hard targets, Schlegel and Moorcroft's analysis identified and correlated 209 enhanced events with various combinations of occurrence time, altitude, velocity, intensity, and spectral characteristics. Achieving ambiguous results, they concluded that the ERB observed at EISCAT was probably due to a combination of satellites and system effects not clearly understood.

The satellite explanation was supported in part by a comparison of the distribution of observed peak velocities with the distribution predicted for hard targets by a satellite catalog. While this comparison was employed successfully with the Millstone Hill data, it fails to discriminate ERB events in this case because the field-aligned

pointing direction at EISCAT produces radar line-of-sight Doppler velocities from the large population of polar orbiting satellites in the range of typical ion acoustic velocities between 1–2 km/sec (see Figure 6-1).

However, a marked difference in the respective height distributions of satellites and the observed peaks was discovered. Shown in Figure 6-2 is the unexpectedly large population of observed low altitude events. Aware that reports of Millstone Hill ERB were restricted to the topside ionosphere above 400 km [FOS88] and lacking additional evidence of geophysical processes, Schlegel and Moorcroft were unable to resolve the disparity in the altitude distributions, leaving the question open for further interpretation. Recently, data reported by Rietveld et al. [1991] (henceforth RD91) unambiguously verified the detection of geophysically induced ERB with the EISCAT radar system.

6.1.2 Range Extended UHF Echoes

Like their counterparts observed at Millstone Hill, the geophysical ERB echoes detected at EISCAT were also characterized by large cross section enhancements (up to 20 dB) and narrow spectral widths similar to those caused by hard targets. These grossly asymmetric spectra cannot be fitted to derive ionospheric parameters by the standard incoherent scatter analysis programs. When the radar is pointed up the magnetic field line both satellite and geophysical ERB echoes appear at the same frequency shift in the power spectra. While this feature renders the field-aligned pointing direction ineffective for a statistical discrimination approach, it actually provides unambiguous geophysical ERB identification when events are considered individually for the following reason.

Enhanced echoes of geophysical origin were believed to be associated with intense electron drifts or currents [FOS88]. The most intense currents are also field-aligned

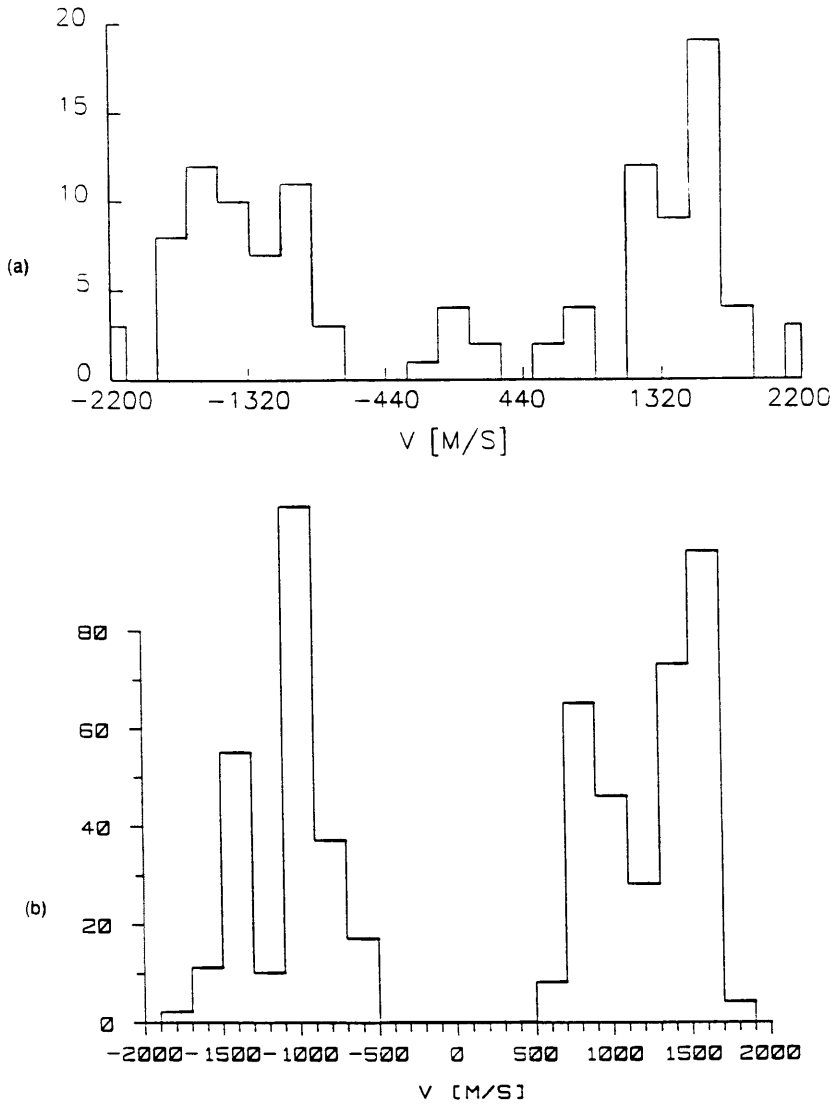

Figure 6-1: Histograms of velocity distribution of a) observed peaks, and b) satellite population. At this look angle geophysical enhancements and polar orbiting satellites share the same velocity range. [after *Schlegel and Moorcroft*, 1989].

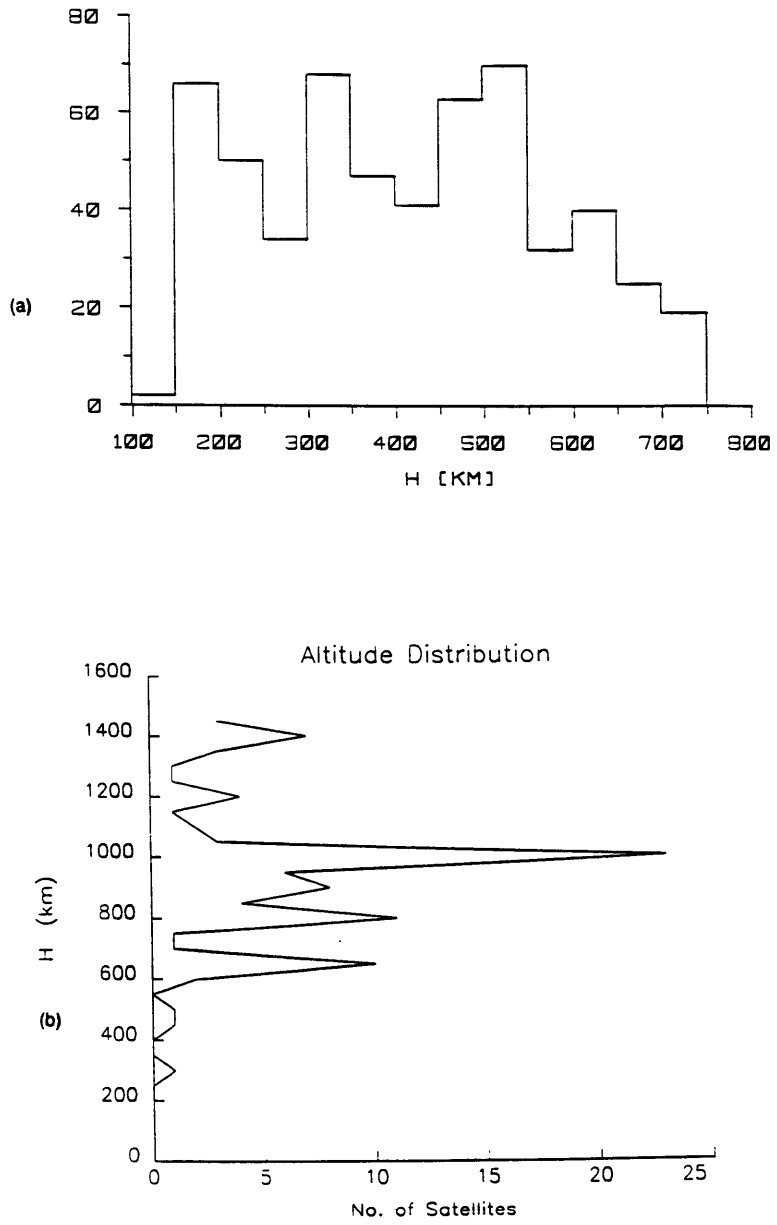

Figure 6-2: Histograms of altitude distribution of a) all observed coherent peaks, and b) satellite population. Note large number of observed peaks below 300 km. [after *Schlegel and Moorcroft*, 1989].

and extend for many kilometers along the magnetic field direction. Enhanced echoes driven by these currents are therefore stimulated over the same extent along the field lines and can be observed with a radar pointed parallel to the same line. (The altitude extent of the Millstone Hill zenith observations is attributed to this effect; see Figure 5-17). Range extended echoes were discovered by RD91 when investigating the details of a cluster of spectra which caused correlator errors due to overflows in the A/D converters of the radar receiver. Two experiments were analyzed (Feb. 14, 1990; Oct. 25, 1989), in which 24 ten–second integration periods were found to contain enhanced echoes. The following summary of those observations is adapted from RD91 and private communication with M. Rietveld, 1991.

A sample of the data is shown in Figure 6-3, where five consecutive 10-sec integration periods are shown which illustrate the transition from normal incoherent spectra to enhanced spectra and back again. The enhanced echoes are extended over a wide range of altitudes; a satellite penetrating the radar beam would appear in at most three range gates in the sampling technique used here. The frequency shift of the anomalous spectra also increases smoothly with altitude, corresponding to the increase in the ion acoustic speed with height, further evidence of the echoes' geophysical origins.

The spectra in Figure 6-3 vary dramatically during the 30 seconds in which the anomalous echoes appear. The spectra are enhanced at altitudes as low as 130 km and as high as 600 km by as much as 17 dB during the 04:49:50–04:50:00 period. The enhancements can be very asymmetric in either the upshifted or downshifted peak, or relatively symmetric with both ion acoustic peaks amplified by nearly the same amount. A transition in the sign of the frequency shift of the asymmetric peak enhancements can occur within a single 10 second integration period over several tens of kilometers. The statistics of which type of enhancement (asymmetric upshift,

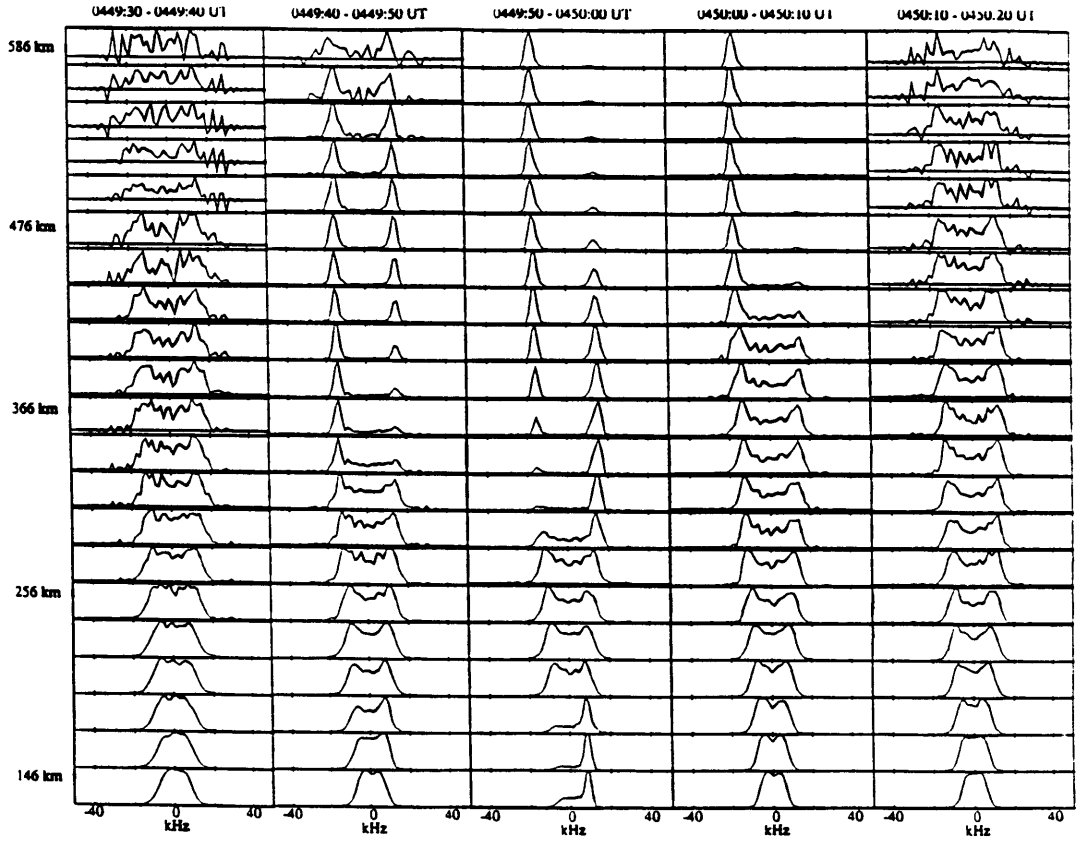

Figure 6-3: Five consecutive 10-sec integration periods observed with the EISCAT UHF radar. Within the 50-sec time period the ion lines change from normal to enhanced and back again [after RD91].

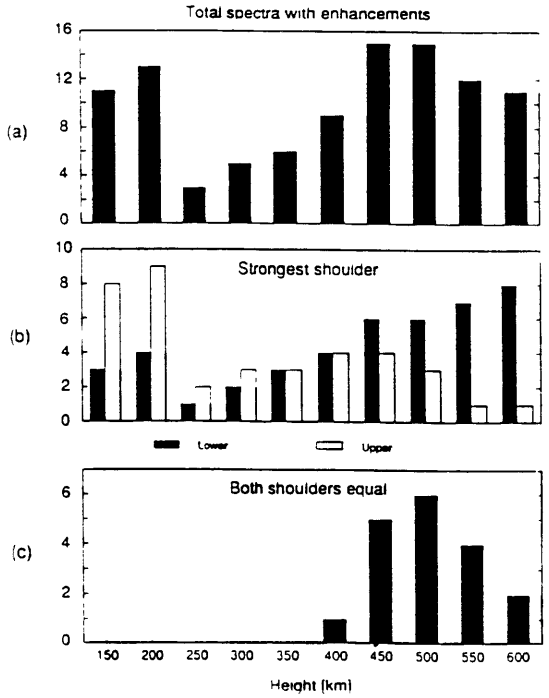

Figure 6-4: Histograms showing the height distribution of enhanced ion acoustic spectra categorized by a) total enhanced spectra; b) upshifted or downshifted peak enhancement; and c) both peaks enhanced symmetrically [after RD91].

asymmetric downshift, or symmetric) was observed in the two experiments under discussion are presented in histograms in Figure 6-4.

The figure indicates that there appear to be two main altitude regimes favoring the spectral enhancements, with a minimum rate of occurrence at around 250 km. In the higher altitude regime, the enhancements are primarily asymmetrically downshifted or symmetric; at lower altitudes upshifted asymmetric spectra are more common. The enhancements are found to be largest in the topside ionosphere above 250 km, and have lasted as long as 50 seconds continuously; shorter sporadic bursts distributed over a period of a few tens of minutes are seen more frequently. As more anomalous echoes from other experiments have been found, it appears that the low altitude enhancements are rare. Additionally, several ERB events have been observed when the radar was not pointed field-aligned, at was directed at aspect angles up to 20°. The echoes are then found to be localized rather than extended in range, as in the observations reported from Millstone Hill.

Geophysical Conditions

Geophysically, the events occur in the presence of sharp fluctuations in the local magnetic field ($\sim$ 500 nT N–S), auroral particle precipitation evidenced by airglow, elevated electron temperatures (T_e up to 8000°K), and electron-to-ion temperature ratios greater than two, though not extremely high (typically, $2 \leq T_e/T_i \leq 3$). Several more ERB events have been discovered in EISCAT data since RD91; some of these cases were more closely correlated with elevated ion temperatures, strong perpendicular electric fields, and little, if any, auroral precipitation [*Wahlund et al.*, 1991]. Based on an evaluation of the sparse existing data, the physical mechanisms responsible for the observed enhancements are explored in Chapter 7. A recently conducted experiment to obtain better data is described in the next section.

6.1.3 Dedicated ERB Experiment Performed at EISCAT

In late November 1990, EISCAT radar time to acquire new data was provided by Dr. Kristian Schlegel of the Max Planck Institute for Aeronomy, and a single experiment designed to measure ERB with the highest possible resolution in time and space was conducted. The methods and results of the experiment are presented below.

Experimental Description

Experimental considerations for conclusively obtaining good quality enhanced echoes were determined by our understanding of the phenomenon. The experiment was designed to provide high resolution (in frequency and time) power spectra over a large altitude extent, primarily at field aligned and vertical look angles. The field-aligned position facilitates observing enhancements over a large altitude extent, while the vertical position constrains the possible line-of-sight satellite velocities to subsonic speeds in the ionosphere and shares common scattering volume with the VHF radar.

Experimental Description

SP-GE-SAT
11/29/90, 16:00 UT - 11/30/90, 08:00 UT

Radar Parameters (Block 1)
- pulse length 500 μs
- sampling interval 10 μs
- gate separation 75 km
- number of scatter gates 13
- total range 225-1175 km

Scan Cycle
- field-aligned 15 min
- vertical 5 min

Channels 5 and 6 were used to monitor plasma lines. All other channels were used to record the ion line.

Radar Parameters (Block 2)
- Same as CP-3

Scan Cycle
- 20 min elev. scan, 11 points (abbreviated version of CP-3 elev. scan)
  $\pm$ 28° elev.scan in north-south plane through Tromsø and Kiruna

Block 2 run approximately every two hours for background diagnostics. The VHF antenna was pointed vertical throughout the experiment.

Figure 6-5: Radar operating parameters employed in experiment to investigate ERB at EISCAT on November 30, 1990.

Ideally we hoped to obtain simultaneous UHF and VHF measurements for radar cross section measurements at two frequencies.

A 20-minute elevation scan was performed approximately every two hours for diagnosis of background ionospheric parameters. Two plasma line receiver channels were also recorded to deduce ionospheric currents directly. A complete description of the radar parameters and scan cycles employed in the experiment is given in Figure 6-5.

To distinguish the enhanced echoes from actual hard targets we relied on the multi-static capability of the EISCAT UHF system to obtain full 3-D Doppler information. Coherent echoes detected within the common scattering volume which did not exhibit velocities consistent with hard targets could be attributed to geophysical effects. In addition to hard target discrimination, the tri-static system can provide

the aspect angle dependence of the enhanced radar cross section, an important clue to understanding the physics of this phenomenon. To better facilitate the task of acquiring coherent echoes in the common scattering volume, a "smart" real-time radar control program was employed.

This control program, named MONITOR, was written by Anthony van Eyken utilizing an "ERB detection" algorithm developed by Keith Groves and Mike Rietveld. The received ion line spectra were monitored in real-time to detect enhancements. When enhanced spectra were detected, the remote receiving antennas were automatically repositioned to observe the altitude of maximum enhancement along the transmitted radar beam, as depicted in Figure 6-6. This process was usually completed within 10 seconds, considerably less than the time scales over which the echoes can persist (a few tens of seconds). The program was tested by looking at satellites to simulate ERB. An additional valuable feature of MONITOR is the capability to automatically reduce the integration period when enhanced power levels are detected, acquiring high time resolution measurements with adequate signal-to-noise.

Initially, the 30-hour allotment of radar time was scheduled as a single time block beginning at 08:00 UT on November 29, 1990. Because the most promising periods for enhanced echo observations are believed to begin in the early evening and continue into the early morning hours, however, we chose to use only half the allotted time for the first experiment, beginning at 16:00 UT, and save the remaining time for additional observations on the evening of December 1.

From a technical standpoint, the experiment was executed smoothly; unfortunately, it appears that enhanced radar backscatter was not observed. This is undoubtedly due to the lack of appropriate geophysical conditions during the entire observational period. Magnetically, the ionosphere was very quiet; the magnetogram at the Tromsø site showed only weak, gradual variations, and the Ap index for the

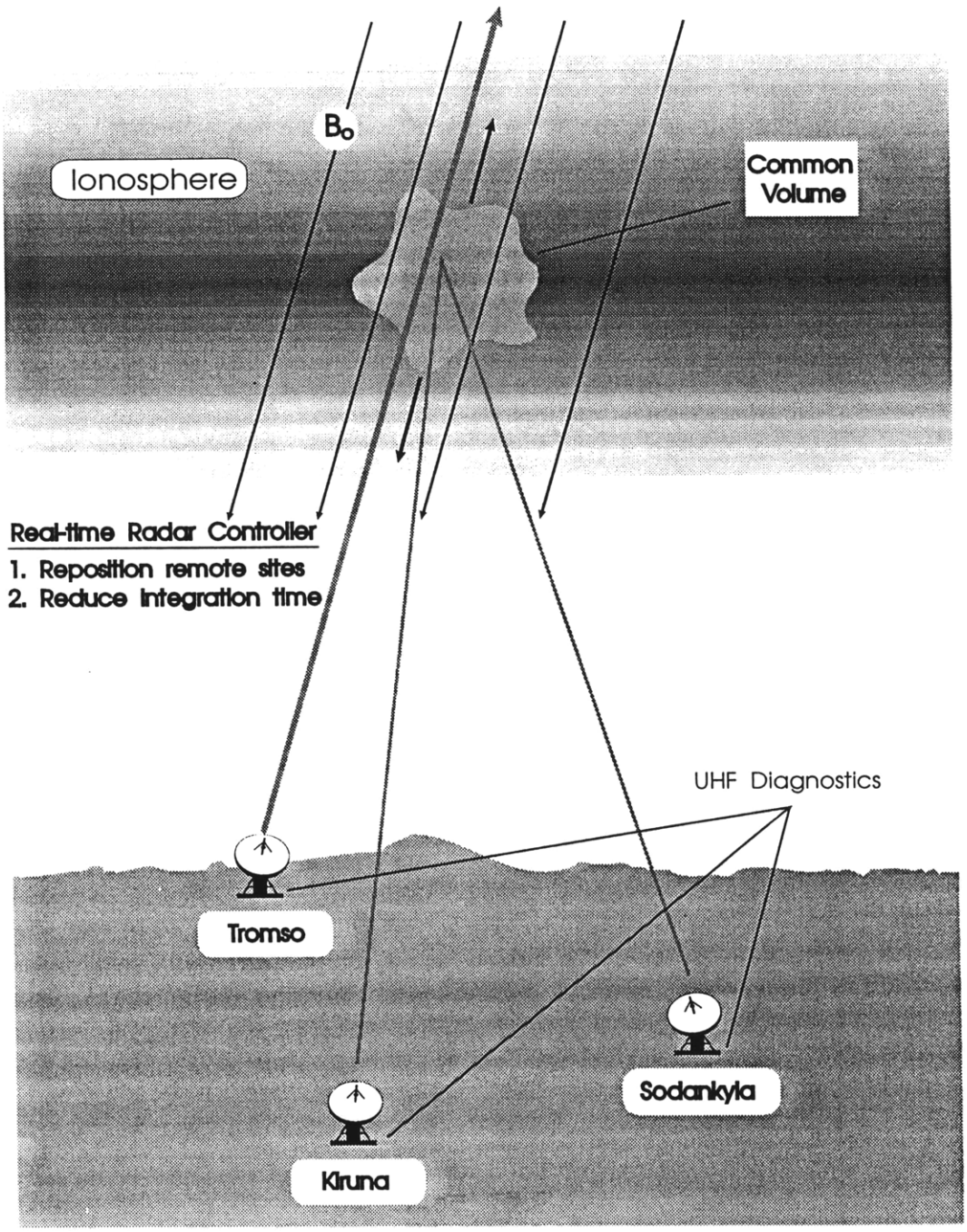

Figure 6-6: Conceptual drawing of the ERB experiment performed at EISCAT in November, 1990. A realtime monitor program was employed to detect and locate ERB; the remote receiving antennas were then repositioned to sample the same volume.

period was a meager five. Also, there was no evidence of particle precipitation, and electron temperatures remained below 3000°K. Additional observing periods were tentatively planned for the evenings of December 1 and 4. On the basis of the latest forecasts for very quiet conditions on both days, however, it was decided not to run dedicated coherent echoes experiments. A search through existing data was believed a more efficient means of locating additional ERB events.

6.1.4 UHF Common Program Data

The computer algorithm used to detect enhanced power spectra in real-time can also be used to analyze existing raw data tapes. Each spectra is checked, and those that exceed predetermined levels of asymmetry and/or overall power enhancement are recorded for later analysis. For these analyses, a 3 dB asymmetry threshold was used to reduce the large number of false detections due to low SNR, even though using the algorithm at this sensitivity level probably results in failure to detect some weak enhancements. I decided to look at CP-2 data initially, hoping to find enhanced UHF echoes in the vertical antenna position which could be compared with the VHF returns from the same scattering volume. CP-2 designates *Common Program 2*, a standard operation mode which includes both field-aligned and vertical radar look-angles. A total of 111 hours of Tromsø CP-2 data and 318 hours of data from the remote sites was reduced and analyzed for additional evidence of enhanced radar backscatter. The actual experiments analyzed are shown in Table 6.1.

Despite the relatively large amount of data analyzed, significant occurrences of ERB were not found. As with the experiment, the probable cause for the lack of enhanced echoes is the low level of magnetic activity present during the time periods analyzed. In addition, only a small volume of space is monitored by the stationary radar beam which requires that ERB processes occur in very specific locations. While

Table 6.1: Table of Analyzed Common Program Experiments. T, K, and S denote Tromsø, Kiruna, and Sodankylä.

STRT. DATE–UT	END DATE–UT	MODE	SITES
87/10/20–09:30	87/10/21–14:00	CP-2-D	K,S
87/10/21–14:00	87/10/22–23:30	CP-2-D	T,K,S
88/08/09–08:00	88/08/10–08:30	CP-2-D	K,S
88/08/16–08:00	88/08/18–23:00	CP-2-D	T,K,S
89/10/23–18:00	89/10/25–14:30	CP-2-D	K,S
89/10/24–17:00	89/10/25–07:30	CP-2-D	T
90/11/27–17:00	90/11/27–18:00	CP-2-D	T

not indicative of all localized auroral processes, the Ap index for magnetic activity does provide an estimate of the general level of magnetic disturbance globally. This index was less than 15 (quiet) on all but one of the nine days investigated, and less than 10 on all but two. These periods were chosen for analysis initially because they were available at the Tromsø site. Later, due to several reasons (primarily computer failure), it was possible to process only half the data originally slated for analysis at EISCAT Headquarters in Kiruna, Sweden. In addition, 24 hours of data processed from disturbed time periods was lost due to a faulty data transfer.

Tromsø Data

About 2.5% of the Tromsø spectra surveyed were determined to be asymmetrically enhanced; more than 95% of the selected spectra are not geophysically significant. Most result from satellites penetrating the radar beam; some are asymmetric because of random noise spikes in low SNR data from high altitudes. Only two cases of interest were found in the data examined thus far.

The first, shown in Figure 6-7, is comprised of enhanced spectra previously found by Mike Rietveld and proves the value of this method of analysis. The data quality for the October 24/25 experiment was quite good, and only 42 spectra were computer-selected from 14 hours of data. Of these 42, 16 are clearly enhanced by geophysical

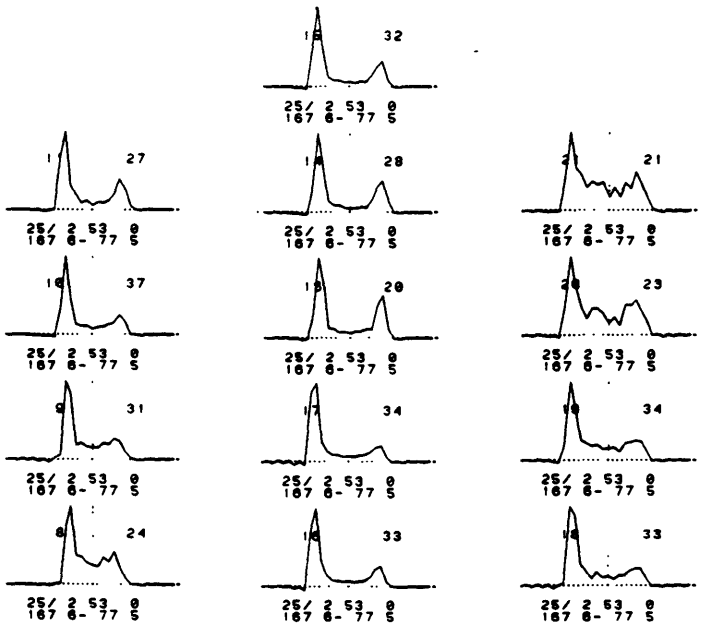

Figure 6-7: Asymmetric enhanced UHF spectra from October 1990 extended over 13 consecutive range gates. The range gate number is on the upper left of each plot; the number on the upper right is the asymmetry index assigned by the MONITOR detection algorithm.

mechanisms as evidenced by their sequential extent in range. This data set is the exception with regard to geomagnetic activity noted above. It was recorded three days after the peak of one of the largest magnetic storms on record. Actual conditions for the day and hour of the enhanced echoes occurrence are characterized by an Ap index of 23 and a 3-hr Kp of 5.

Data from August 18, 1988 form the second interesting case (see Figure 6-8), when weakly enhanced spectra were observed in the UHF radar beam continuously for more than 30 seconds at ranges varying from 520 - 600 km along the magnetic field. The localized nature of the enhancements does allow the possibility that the spectra may be a hard target signature in the beam. Figure 6-9, however, indicates that a satellite at 600 km range could remain in the stationary radar beam for no more than a few seconds, and direct measurements of satellites with the EISCAT system support this

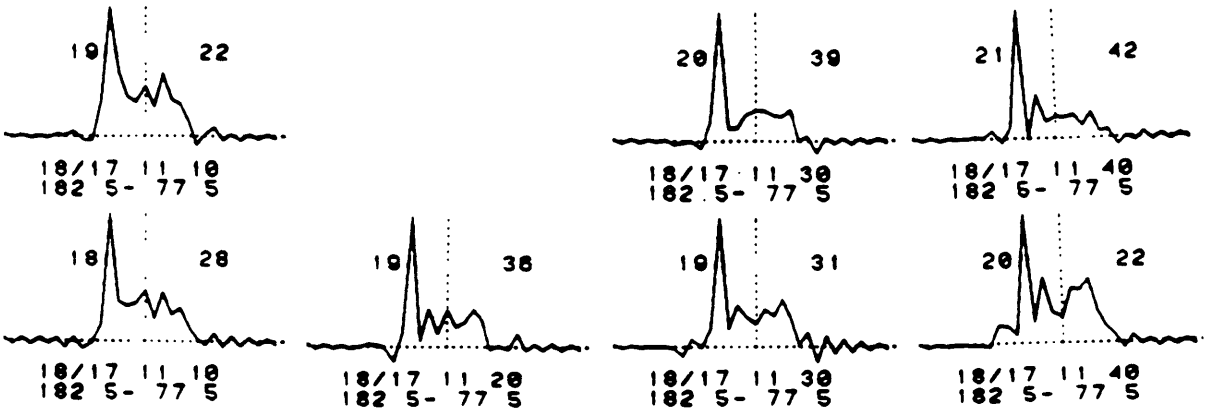

Figure 6-8: Weakly enhanced ion acoustic spectra seen in four consecutive 10-second integration periods. The range varies from 520 km to 600 km; a satellite at this range would pass through the radar beam in less than five seconds.

conclusion.

These spectra were selected by the MONITOR program and represent the interesting data I have from this time period. It is entirely possible that there are other spectra recorded during this time period which, while not detected by MONITOR (and therefore not recorded), contain meaningful levels of asymmetric enhancement.

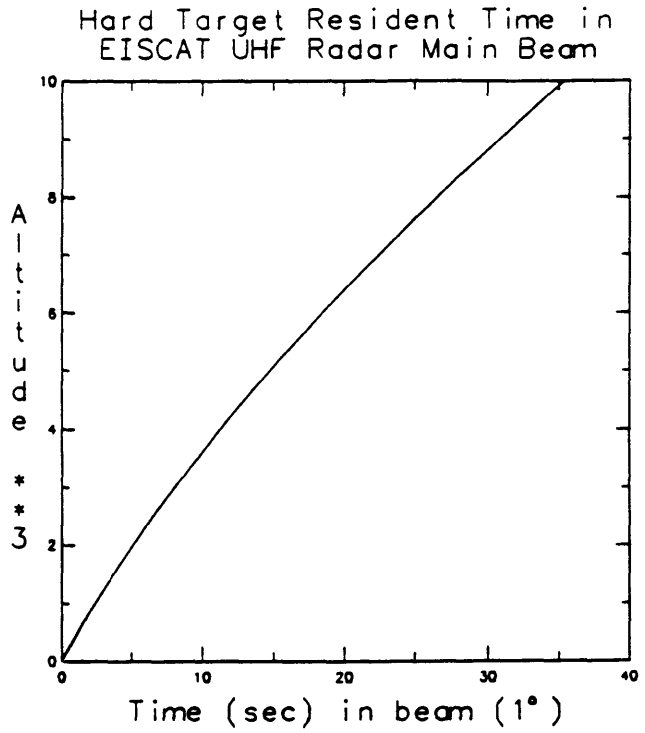

Figure 6-9: Approximate main beam satellite transit time as a function of altitude for the 1° EISCAT UHF radar beam. Targets below 1000 km remain in the beam for less than five seconds. Circular orbits are assumed.

Remote Sites Data

As pointed out previously, enhanced echoes observed by all sites can be conclusively attributed to geophysical sources if they do not exhibit a 3-dimensional Doppler velocity consistent with orbiting bodies. Motivated by the promise of unambiguous classification, a large amount of data from the remote receiving sites at Kiruna and Sodankylä was examined. However, not a single case of ERB was detected by MONITOR in more than 300 hours of remote site data.

The lack of detections is somewhat puzzling, particularly because during the October 24/25 experiment moderately enhanced spectra were observed at Tromsø from the common volume scattering height of 278 km. Unfortunately, the remote sites were not pointed at this altitude during the period of observed ERB; in fact, no coincident measurements of ERB have been discovered thus far. This can be partially explained by the fact that the remote sites monitor altitudes at 278 km or below, where very

few enhancements have been seen.

The aspect angle sensitivity of ERB processes may prove important, as well, because the remote sites are not able to view the F region common scattering volume at small aspect angles. Because the enhancement phenomenon is associated with field-aligned processes, it is possible that it produces a much weaker signature when diagnosed by the remote sites at large aspect angles. A final consideration is that the scattering volume available to the remote sites is determined by the intersection of their receiving antenna beam and the radar beam transmitted from Tromsø. The respective radar beams are only about five kilometers in diameter at the intersection altitude of 275 km. This provides a relatively small scattering volume, and the power received by the remote sites is considerably less than that received from direct backscatter at Tromsø. Nevertheless, the continuing effort to find more cases of ERB in the EISCAT data will probably uncover some events diagnosed simultaneously by both the Tromsø receiver and the remote sites, providing new insights into the physics of these events as discussed in Chapter 7.

6.1.5 EISCAT VHF Observations of ERB

Evidence of ERB events detected with the EISCAT VHF radar were recently reported by *Collis et al.*, [1991] (henceforth, COLL91). The enhanced spectra are similar in appearance to those recorded by the UHF radar discussed previously. A summary of their characteristics follows.

Summary of VHF Observations

VHF ERB was observed during experiments in January 1989 and February 1990 [COLL91]. Both cases were associated with unusually strong visible red aurora as indicated by all-sky imagers and scanning photometers. The auroral signatures are

believed to be caused by low energy ($E \leq 100$ eV) precipitating electrons. A sample of the VHF echoes is shown in Figure 6-10, where the altitude variation of the enhancements over a three minute period in the February experiment is evident.

The apparent downward motion of the ERB is interpreted by COLL91 to represent the equatorward motion of a field-aligned structure (*e.g.*, auroral arc) passing over the radar. The VHF echoes shown in Figure 6-10 are not extended in range because the antenna is pointed to the zenith, rather than field-aligned as in the case of the UHF enhancements. Further consideration of the data indicates other differences between the VHF and UHF enhancements. The VHF events are found at much higher altitudes (up to 1350 km) and persist for much longer, up to four minutes in the example shown here. In the February 1990 experiment VLF spectra were enhanced sporadically for more than one hour. By comparison, UHF events at EISCAT have not been found above 600 km, and 50 seconds represents the longest period of uninterrupted enhancement, while the duration of sporadic enhancement periods does not exceed about ten minutes. These facts indicate that the enhancements may be more easily excited at VHF frequencies [COLL91].

The frequency shift of the enhanced peak was seen to change from upshifted to downshifted during the course of about a minute in the January 1989 experiment. ERB data acquired during the February 1990 event, however, are characterized by a consistent dominant enhancement of the downshifted peak for up to four minutes, though at times both peaks were enhanced in the same integration period. This is in contrast to the UHF measurements where the asymmetry seems to fluctuate more rapidly in both time and space between downshifted and upshifted frequencies.

The total cross section enhancement for the VHF spectra ranges from factors of 4–5 during the January experiment to greater than 25 in the February events. Measurements of ERB by both the UHF and VHF radars have been recorded during

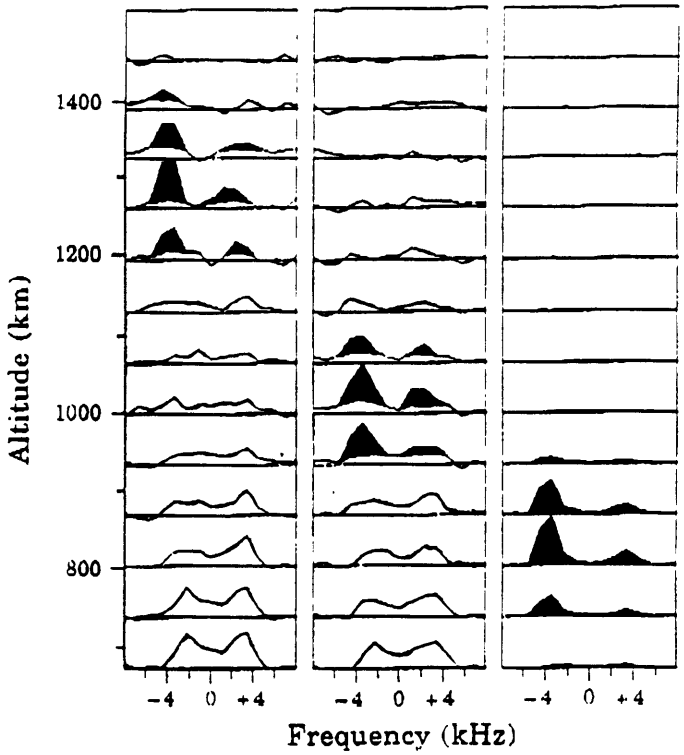

Figure 6-10: Enhanced zenith VHF spectra from 20 February, 1990. The three 10-second integrations shown were recorded 1 minute apart beginning at 18:03:00 UT; the altitude of the enhancement varies smoothly. Enhancements above normal incoherent scatter are shaded black [after COLL91].

the same time period, confirming that both are associated with elevated electron temperatures, large magnetic field fluctuations, and, when optical data is available, with red aurora. Unfortunately, comparisons of simultaneous UHF/VHF spectra from the same scattering volume have not been reported. This is because the VHF antenna is nearly always pointed vertical during experiments, while the UHF dish acquires data at other look-angles a majority of the observing time. The comparison of spectral characteristics at two frequencies would provide important information on the scale size dependence of the physical mechanism responsible for the ERB.

6.2 ERB Observations at Sondreström

The incoherent radar located at Sondreströmfjord, Greenland operates at 1290 MHz and offers an ideal location (≈74° Inv.lat.) for the excitation and detection of ERB at

a wavelength shorter than that of both the EISCAT and Millstone Hill systems. The data base available for such studies is, at present, much more limited than either of the latter sites. Frequent low energy electron precipitation occurring at this latitude increases the likelihood of backscatter enhancements locally.

6.2.1 Zenith Experiments at Sondrestöm

As explained previously, acquiring data with the radar antenna pointed to zenith effectively filters out hard target contamination by limiting the line-of-sight velocity to subsonic magnitudes. Accordingly, attempts to identify ERB events at Sondreström have employed this approach.

Analysis of four hours of zenith data taken in August, 1988 revealed that two of the 20 coherent echoes observed occurred at frequency shifts corresponding to ion acoustic waves; the remainder of the enhanced peaks had essentially no Doppler shift and are presumed to be caused by hard targets passing through the radar beam. The two events at the ion acoustic frequency showed backscattered power enhanced by factors of 2 and 5, respectively; smaller asymmetries were evident in several other spectra. The spectrum enhanced by a factor of 5 is shown in Figure 6-11. The range gates shown in the figure do not overlap, so that a localized target appears in only one gate. This is consistent with EISCAT and Millstone Hill observations of ERB for nonzero aspect angles.

Six more zenith experiments were run at Sondreström in May, September, and October, 1989 and October, 1990 providing 44 additional hours of observations. These data, however, show little evidence of ERB at ion acoustic frequencies; asymmetric enhancements are at most 1.5 times greater than the normal background spectra, not considered statistically significant. No extended periods of ERB occurrence have been found in Sondreström data yet. The lack of ion acoustic ERB in these ex-

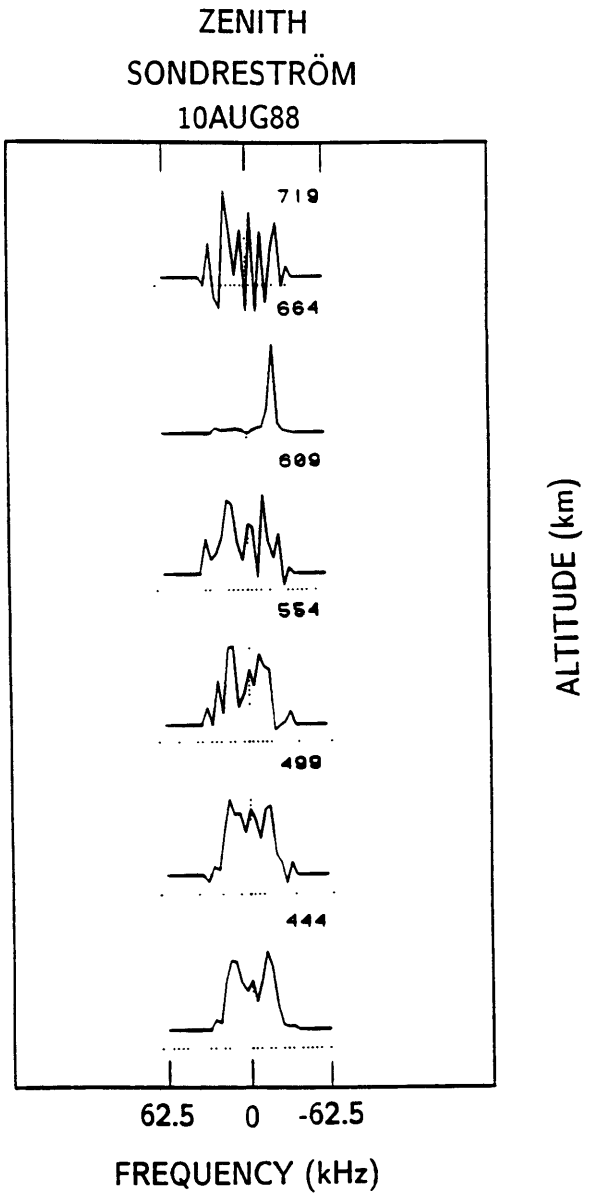

Figure 6-11: Sondreström zenith data showing factor of 5 enhancement in ion acoustic spectrum. Altitude scale is in kilometers.

periments suggests the absence of intense field-aligned currents. The magnitude of these currents is related to the level of geomagnetic activity, generally weak during these experiments. Another reason for the absence of geophysical ERB may be that higher electron drifts are required for enhancement at the short wavelength (12 cm) diagnosed by the Sondreström radar.

6.3 Summary of ERB from Other Sites

Important progress has been achieved towards identifying and understanding enhanced radar backscatter from the ionosphere. Such events are known to occur briefly and infrequently under special ionospheric conditions; enhancements below 250 km are especially rare. The most prominent observations reported by RD91 and COLL91 associate ERB events with red aurora (*viz.*, particle precipitation), large magnetic field variations locally, and elevated electron temperatures. These requirements are also reflected by global magnetic indices for the periods indicating very disturbed conditions. The EISCAT ERB observations have been seen when Kp$\geq$ 5, a level of disturbance occurring about five percent of the time during solar max [*Mayaud*, 1980]. Comparing the Millstone Hill, EISCAT and Sondreström observations suggests that ion acoustic spectra may be enhanced over a wide range of scale sizes; enhancement thresholds appear to decrease with increasing wavelength.

These findings are basically consistent with the current driven source mechanisms of Kindel and Kennel [1971] and Rosenbluth and Rostoker [1962] suggested by FOS88, RD91, and COLL91. These mechanisms show that a relative drift between the electrons and the ions (*i.e.*, a current) in the plasma will produce asymmetric enhancements in the observed ion acoustic spectrum. The frequency shift of the asymmetry depends on whether the electrons are drifting towards (upshift) the radar or away (downshift) from the radar. A puzzling inconsistency with the known mechanisms,

however, stems from the commonly observed simultaneous enhancement of both upshifted and downshifted ion acoustic peaks. The magnitude of enhancements larger than 7 dB and the detection of ERB at nonzero aspect angles are also not described adequately by RR and KK. Possible explanations for these observations based on existing theories and an alternative mechanism for ion acoustic enhancements are presented in Chapter 7.

Chapter 7

Enhanced Radar Backscatter (ERB) Theory

This chapter describes the application and evaluation of theoretical models to explain the observations of ion acoustic ERB described in Chapters 5 and 6.

In section 7.1, the current driven processes first reported by Rosenbluth and Rostoker [1962] and Kindel and Kinnel [1971] are applied to the ERB observations. These theories can explain general features of the data, but require current densities much greater than have been previously measured on satellites (>1 $mamp/m^2$). Furthermore, they are not able to adequately describe the magnitude of ion acoustic enhancements larger than about 7 dB ($\sim 5 \times 10^{-17} m^2/m^3$), the commonly observed symmetric enhancement of upshifted and downshifted wave modes, and the detection of ERB at nonzero aspect angles with respect to the geomagnetic field.

Section 7.2 describes the new application of a mechanism predicting the amplification of ion acoustic waves through the nonlinear coupling of intense Langmuir waves. This idea was originally proposed by Lee [1981] to explain the enhancement of ion lines in heating experiments at Arecibo Observatory, where the HF heater was the source on Langmuir wave turbulence near the heater wave reflection height. In my

investigation of this mechanism, the intense Langmuir waves are excited by the large suprathermal electron population associated with field-aligned currents and auroral arcs. The investigation of a new explanation is warranted because of the inadequacies of existing theories mentioned above, and the realization that the suprathermal electrons' wave-particle interaction with the background plasma represents an additional source of free energy for ion acoustic wave enhancement.

Section 7.3 contains a discussion of the various theories with regard to the observations of Chapters 5 and 6. The nonlinear coupling mechanism predicts both the magnitude and the shape of many of the observed enhancements. Furthermore, it can contribute to ion acoustic enhancements in conjunction with other current driven mechanisms.

7.1 Application of Existing Current Driven Theories

A limited number of theoretical investigations of ion acoustic wave enhancements have been conducted, but two prominent sources considering the topic exist in the literature. The processes investigated by Rosenbluth and Rostoker [1962] for marginally stable plasmas and Kindel and Kennel [1971] for plasma instabilities are potential mechanisms whereby ion acoustic waves are amplified by large electron drifts relative to the ions. The implications of these theories with regard to observed enhancements is discussed below.

7.1.1 Ion acoustic enhancements in a stable plasma

The spectral shape of high frequency ($\omega >> \omega_p$) radiation scattered from a plasma was discussed in Chapter 5 and the references therein; the effects of electron and ion

temperature, density, composition, and bulk drift velocity on the spectra were briefly described. This work was extended by Rosenbluth and Rostoker (henceforth, RR) and Lamb in 1962 to include the effects of a *relative* drift between the electrons and ions on the shape of the scattered wave spectrum. Such a drift, of course, corresponds to a current flowing in the plasma. The basic approach was to modify the linear dielectric function used previously by simply replacing the usual electron Maxwellian distribution function, $f_e(\mathbf{v})$ with a *drifting* Maxwellian distribution,

$$\begin{aligned} f_e(\mathbf{v}) &= \left(\frac{m_e}{2\pi E_{th}}\right)^{\frac{3}{2}} \exp\left[-\frac{m_e \mathbf{v}^2}{2E_{th}}\right] \\ &\Rightarrow \left(\frac{m_e}{2\pi E_{th}}\right)^{\frac{3}{2}} \exp\left[-\frac{m_e(\mathbf{v}+\hat{\mathbf{e}}U)^2}{2E_{th}}\right] \end{aligned} \tag{7.1}$$

Here m_e, E_{th}, and $\hat{\mathbf{e}}U$ correspond to the electron mass, electron thermal energy, and drift velocity, respectively. The assumed direction of the drift velocity relative to the incident (k_i) and reflected (k_r) radar waves is shown in Figure 7-1. The effects on the ion line spectrum are shown in Figures 7-2 and 7-3, where the power spectra for different drift velocities (normalized by the electron thermal velocity) and different electron-to-ion temperature ratios ($T_e/T_i \equiv T_r$) are plotted on a logarithmic scale.

The obvious asymmetries in the ion line enhancements depend directly on the magnitude of the electron drift, approaching infinity for increasing values of y. Mathematically, this means that a singularity in the cross section (zero in dielectric function, $\sigma(\omega) \propto |\epsilon|^{-2}$) exists for sufficiently large values of y; physically, the singularity corresponds to the onset of an instability, and the linear analysis is no longer applicable. The instability threshold drift velocity is very sensitive to T_r, decreasing by more than an order of magnitude as T_r varies from 1 to 5. Even though the spectral asymmetry may be more easily stimulated with increasing T_r, the overall cross section enhancement under these conditions decreases.

Physically the RR enhancements can be understood by recalling the ion line scattering mechanism in the no–drift case. The spectral shape is then determined by

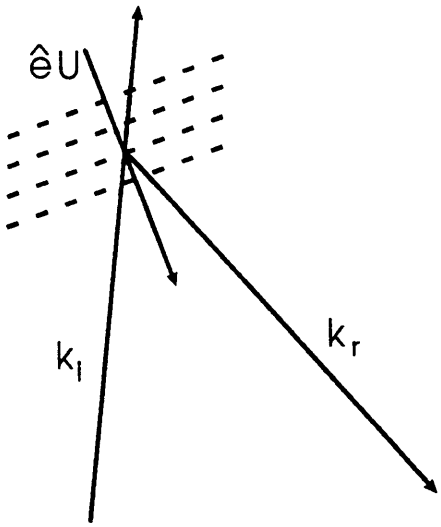

Figure 7-1: Assumed direction of electron drift, $\hat{e}U$, relative to incident and reflected radio waves in the RR mechanism. The drift is perpendicular to the planes of reflection indicated by the dashed lines.

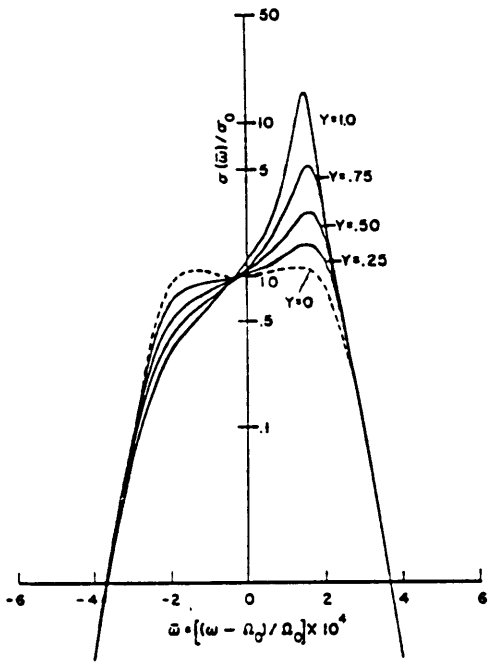

Figure 7-2: Differential scattering cross section for a plasma with electron drift, $y = U/v_{te}$; $T_e = T_i$ [after RR].

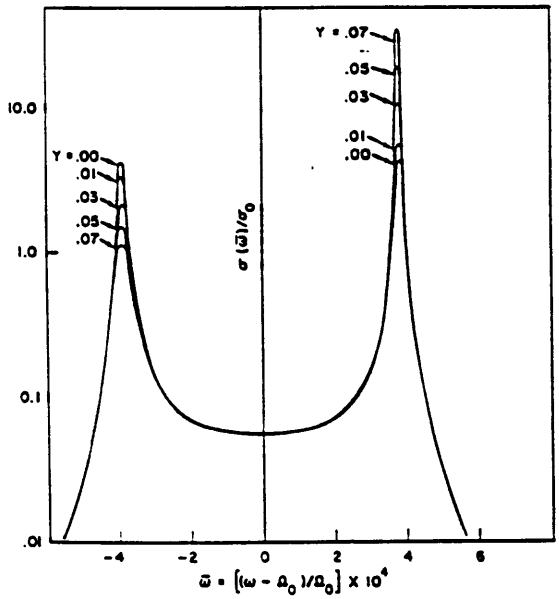

Figure 7-3: Differential scattering cross section for a plasma with electron drift, $y = U/v_{te}$; $T_e = 5T_i$ [after RR].

scattering from electrons shielding thermal density fluctuations propagated by the relatively massive ions in the form of electrostatic acoustic waves. When a drift is introduced by shifting the entire Gaussian electron distribution function in velocity space, there are more electrons available to shield density fluctuations travelling in the direction of the velocity shift and correspondingly fewer in the opposite direction. This explanation is also consistent with the observation that the enhancement of one side of the spectrum is accompanied by a reduction of power in the neighboring hump.

7.1.2 Ion acoustic enhancements via instability

Whereas the mechanism discussed in the previous section applies for a (marginally) stable plasma, Kindel and Kinnel [1971] (henceforth, KK) developed the theory of current driven instabilities in the topside ionosphere when the electron drift velocity exceeds the critical threshold velocity. The physical reason for the instability is that when the electron drift velocity exceeds the phase velocity of ion waves in the plasma, the waves are able to draw energy from the streaming electrons via a collisionless

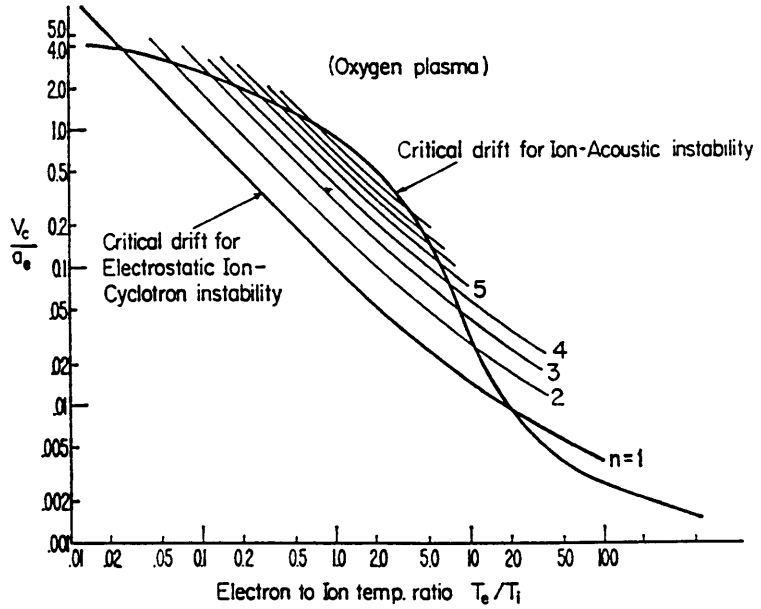

Figure 7-4: Critical drift velocity normalized by the electron thermal speed as a function of T_e/T_i for an O^+ plasma. The threshold is lower for ion cyclotron waves over a wide range of temperature ratios [after KK].

damping process known as Landau damping.

An important result of KK's calculations is that the ion cyclotron wave modes require a lower threshold drift velocity for instability than ion acoustic waves for values of $T_r < 20$, as shown in Figure 7-4. Typical values for T_r in the ionosphere are less than five. As was the case with the RR process, the critical velocity is very sensitive to T_r. This is because the growth of the ion acoustic wave is balanced by ion Landau damping. When $T_r \simeq 1$, the damping is heavy and the drift velocity must exceed the electron thermal speed to produce instability. As T_r increases, however, the phase velocity of the ion acoustic waves increases as well; when the phase velocity of the ion waves exceeds the ion thermal velocity, the Landau damping of those waves is much weaker, and the required drift speeds are correspondingly smaller.

Using typical ionospheric profiles for density and composition, and assuming bulk electron charge carriers, KK cast the critical drift velocity calculation into a critical "electron flux" (i.e., current) calculation for a range of altitudes, as shown in Figure 7-5. Modest values of T_r were assumed in the figure, and the flux required to excite

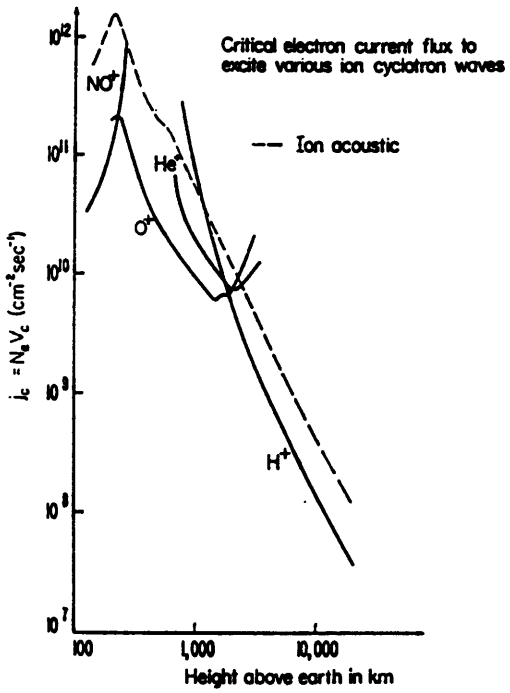

Figure 7-5: Critical electron current flux for instability as a function of altitude for $T_e/T_i \simeq 1$. At every altitude, the threshold for ion acoustic waves exceeds that of cyclotron modes [after KK].

ion acoustic waves is quite high; for reference, the typical background electron flux in the ionosphere is about $2 \times 10^8\ cm^{-2}sec^{-1}$, and the largest localized flux reported in the literature is $6 \times 10^{10}\ cm^{-2}sec^{-1}$ [*Bythrow, et al.*, 1984].

Comparing these numbers with Figure 7-5, the excitation of ion acoustic waves in the ionosphere does not appear likely. However, the curves plotted in the figure are for $T_r \simeq 1$ and an assumed typical density profile. Both parameters have a marked effect on the flux threshold: T_r for the reasons given above, and density because the parameter relevant to the instability is velocity, not flux. Lower densities require higher velocities to deliver the same flux. Applications of KK's results to the real ionosphere should consider these points carefully.

7.2 Nonlinear Mode Coupling Theory of ERB

Presented here is a theoretical investigation of a new mechanism which can enhance radar backscatter in conjunction with known current driven processes, thereby re-

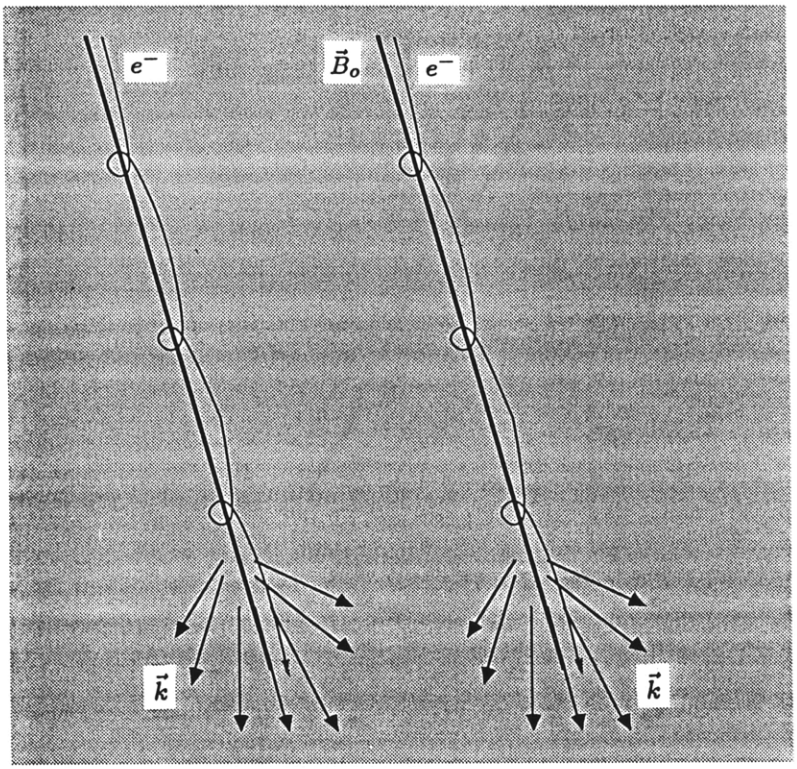

Figure 7-6: Electrons streaming down the magnetic field lines excite a spectrum of intense Langmuir waves. These high frequency waves then couple to drive low frequency ion acoustic waves in the plasma

ducing the threshold amplitudes of the current densities they require. The proposed scenario is as follows. Energetic electrons associated with intense current filaments in the ionosphere excite a suprathermal spectrum of Langmuir waves as they stream through the background plasma. Subsequently the Langmuir waves can become nonlinearly coupled via the ponderomotive force to induce low frequency density perturbations driving ion acoustic waves in the ionospheric plasmas, as described by Lee [1981]. The physics of the proposed mechanism is illustrated conceptually in Figure 7-6.

7.2.1 Intense Langmuir Wave Generation

Because of large Landau damping by bulk electrons, a plasma at or near thermal equilibrium exhibits only very weak electron plasma oscillations (Langmuir waves).

If the electron distribution function has a nonthermal, high energy tail, however, it is possible for the fast electrons to resonantly excite intense Langmuir waves with large phase velocities which are weakly damped [*Pines and Bohm*, 1952]. The intensity, I_p of radiation scattered by these plasma waves in a collisional plasma was first calculated by Perkins and Salpeter [1965], and can be expressed as [*Yngvesson and Perkins*, 1968],

$$I_p = \frac{2\pi K T_p(v_\phi)}{\lambda^2 n e^2} = \frac{T_p(v_\phi)}{2\alpha^2 T} \tag{7.2}$$

The second expression for I_p in equation (7.2) takes the form of an effective temperature of the plasma due to suprathermal electrons normalized by the background temperature. The spectrum of enhanced Langmuir waves in the presence of suprathermal electrons can be calculated by evaluating this normalized velocity dependent plasma temperature T_p,

$$\frac{T_p(v_\phi)}{T} = \frac{f_m(v_\phi) + f_p(v_\phi) + \chi}{f_m(v_\phi) - KT\frac{d}{dE_\phi} f_p(v_\phi) + \chi} \tag{7.3}$$

where f_m and f_p represent, respectively, the Maxwellian and photoelectron contributions to the one-dimensional velocity distribution. They are given by

$$f_m = n\left(\frac{m}{2\pi KT}\right)^{1/2} \sum_{n=-\infty}^{\infty} \frac{e^{-b\sin^2\theta}}{\cos\theta} I_n(b\sin^2\theta) e^{-\left[\frac{(y-n)^2}{2b\cos^2\theta}\right]} \tag{7.4}$$

$$f_p = \int_{E_\phi}^{\infty} \left(\frac{m}{8E}\right)^{1/2} \rho(E)\, dE \tag{7.5}$$

The quantity χ in (7.3) describes the excitation and damping of plasma waves by electron-ion collisions and has the following expression:

$$\chi = \frac{32\pi}{3\lambda^3}\left(\frac{m}{2\pi KT}\right)^{1/2} \ln[4\pi n D^3] \tag{7.6}$$

The parameters in (7.4)–(7.6) are defined by $y = \omega_p/\omega_c$, $b = k^2a^2/2$, and $a = \omega_c^{-1}\sqrt{2KT/m}$; n, T, k, θ, denote the electron density, electron temperature, wave number associated with the backscatter geometry, and the angle between the radar beam and the earth's magnetic field, respectively. I_n represents a Bessel function

of the first kind of imaginary argument. The Maxwellian contribution described by equation (7.4) is complicated by the presence of the magnetic field which introduces a strong aspect angle sensitivity in the collisionless damping rate [*Salpeter*, 1961]. Evaluation of four or five terms of the sum in (7.4) provides good accuracy.

The density of particles per unit volume-energy is given by $\rho(E)$; this parameter is derived from satellite data for the quantitative analysis presented in Section 7.2.3. When $\rho(E)$ is sufficiently large at high energies, a spectrum of enhanced Langmuir waves will be excited near the plasma frequency. Radar observations of these waves, the so-called *plasma line*, have been used to estimate the flux of nonthermal electrons generated by solar radiation [e.g., *Yngvesson and Perkins*, 1968; *Cicerone and Bowhill*, 1971; *Abreu and Carlson*, 1977].

7.2.2 Nonlinear Langmuir Wave Coupling

These Langmuir waves can become a potential source for generating ion acoustic waves through nonlinear coupling via the ponderomotive force according to theory [*Lee*, 1981]. The ponderomotive force induces low frequency ($\omega = \omega_1 - \omega_2$) density perturbations, δn, with the form

$$\delta_n = n_o \frac{\mathbf{F} \cdot (\mathbf{k}_1 - \mathbf{k}_2)\sigma_e \sigma_i}{e^2(\omega_1 - \omega_2)(\sigma_e + \sigma_i)} \tag{7.7}$$

where $\mathbf{F}$ represents the ponderomotive force, (ω_1, $\mathbf{k}_1$) and (ω_2, $\mathbf{k}_2$) represent two high frequency Langmuir waves, and σ_e and σ_i are the electrical conductivities for electrons and ions, respectively. The scattering cross-section of these low-frequency density perturbations can be expressed as

$$\sigma_s(\omega_o + \omega)d\omega = \frac{\sigma_T < |\delta_n(k,\omega)|^2 >}{2\pi V_L t_L} d\omega \tag{7.8}$$

where $<| \delta_n(k,\omega) |^2>$ is the power spectrum of the density perturbations, σ_T is the Thomson differential cross-section, V_L is a very large volume and t_L is a very long

time interval. If the enhanced Langmuir waves are characterized by a spectral density $W(\mathbf{k}_1)$, the expression (7.8) can be written as

$$\sigma_s(\omega_o + \omega) = \gamma k^{-1} \int \int W(\mathbf{k}_1) W(\mathbf{k}_1 - \mathbf{k}_2)\, d\mathbf{k}_1 \tag{7.9}$$

where γ is a parameter to be determined by the characteristics of ionospheric plasmas and the detailed nonlinear mode coupling process.

7.2.3 Analysis with Regard to ERB

The velocity dependent temperature, T_p, expressed by (7.3) represents the enhancement of the Langmuir wave power relative to the weak thermal level power as a function of phase velocity (v_ϕ) and aspect angle (θ); its value depends on three primary parameters, f_m, f_p and χ. Of these three, f_m and χ are determined by the background ionospheric parameters typically associated with observed geophysical ERB events, given by $T = 2000°$ K, $\omega_p/2\pi = 2.8$ MHz, and $\omega_c/2\pi = 1.1$ MHz. As previously stated, f_m represents the Maxwellian contribution to the one-dimensional electron distribution function and vanishes for velocities much larger than the electron thermal velocity ($v_\phi \gg v_{th}$).

At such large velocities, the ratio in (7.3) is usually dominated by the electron-ion collision term, χ, and T_p remains equal to the usual electron temperature, T. If, however, the photoelectron (suprathermal) contribution to the distribution function, f_p, is sufficiently large and its derivative sufficiently small at a given energy, T_p may be many times greater than T, indicating the resonant excitation of intense electron plasma waves. These plasma waves may then couple nonlinearly to drive ion acoustic waves as described in the previous section.

The quantities used to derive $f_p(E)$ in this calculation are from electron flux measurements made aboard the DMSP-F8 satellite (31 eV - 31 keV) and the DE-2 satellite (5 eV - 31 eV) (*W. Denig*, private communication, 1990; *J. D. Winningham*,

private communication, 1987); these data are shown in Figure 7-7a and 7-7b. The electron flux data used are representative of relatively intense auroral arc events observed at high latitudes. The ion flux data from DMSP shows no signature at the time period (see arrow) where the low energy electron flux intensity peaks, indicating that the electrons are carrying significant currents. The resulting values for $\rho(E)$ were then extrapolated linearly down to 1 eV and integrated to give the one-dimensional distribution function along the magnetic field, f_p. Figure 7-8 shows the derived f_m and f_p as a function of particle velocity used to calculate the spectrum of excited Langmuir waves via equation (7.3).

The results of the excited Langmuir wave spectrum are plotted in Figure 7-9. The composite electron distribution function used to calculate the spectrum has been assumed to be one-dimensional along the magnetic field line. As might be expected, for electron energies below about 10 eV, the excited Langmuir wave spectrum is highly field-aligned due to the strong magnetic field dependence of the Landau damping; at higher energies (corresponding to the smaller wavenumbers in Figure 7-9), however, wave phase speeds are sufficiently large to support propagation with relatively weak damping at all aspect angles. To estimate the magnitude of the relative radar cross section enhancement of the ion acoustic fluctuations, a quantity $T_p' \propto W(\mathbf{k}_1)W(\mathbf{k}_1 - \mathbf{k}_2)$, the integrand in (7.9), was calculated; the results are displayed in Figure 7-10. KZ and KY represent the ion acoustic wave vectors parallel and perpendicular to the magnetic field, respectively. The plot shows substantial ion acoustic wave enhancement over a wide range of wavenumbers, with the most intense amplification occurring for wavenumbers less than ten. This is not surprising because smaller wavenumbers correspond to higher energy particles which completely dominate the Maxwellian term in (7.3) at energies much greater than the thermal energy, KT. For the backscatter wave number at which Millstone's 440 MHz incoherent scat-

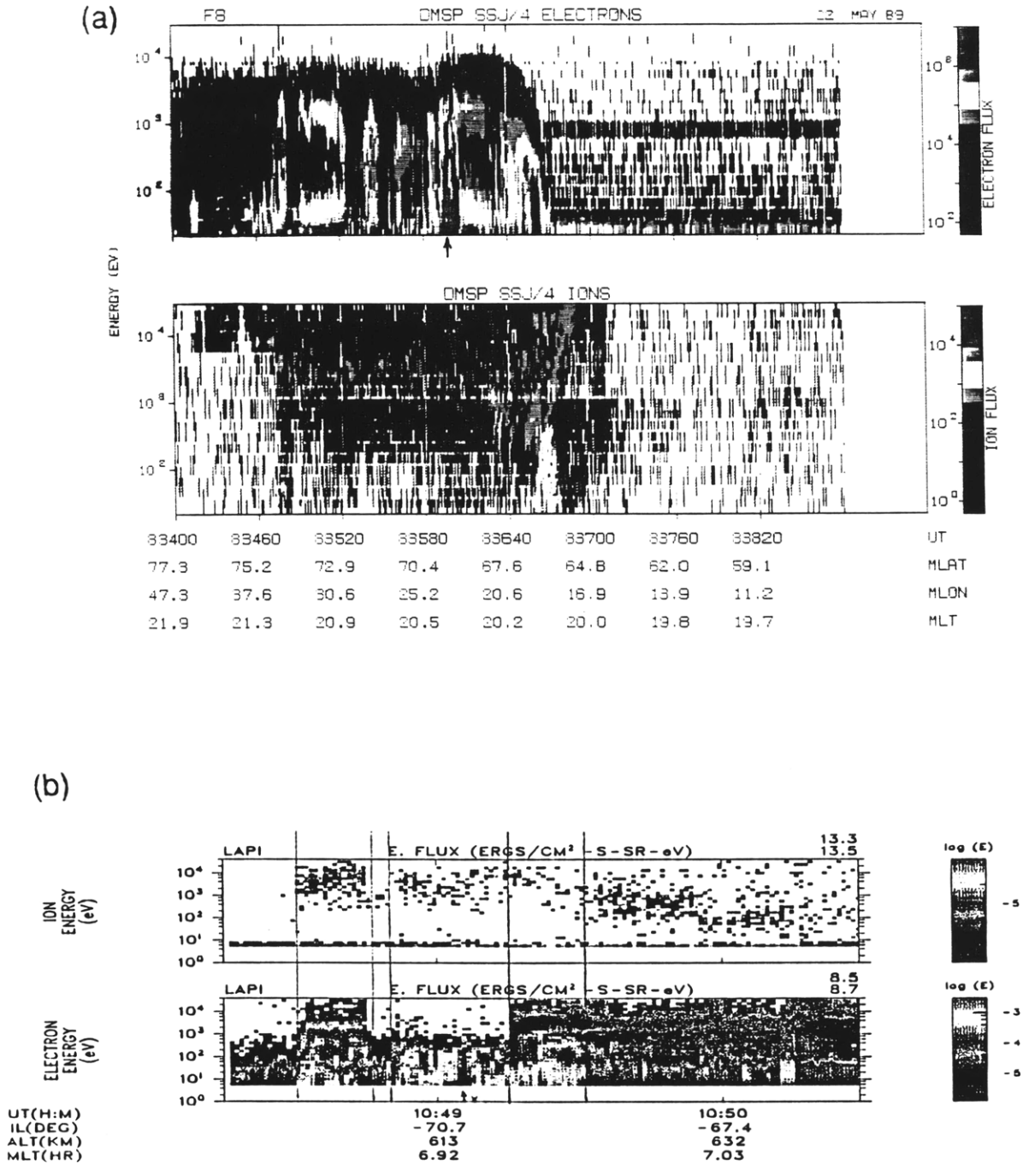

Figure 7-7: Electron spectrograms used to calculate Langmuir wave spectrum: a) electron energy spectrogram from DMSP–F8 and b) electron energy flux from DE–2. The small arrows indicate the time period used for the Langmuir wave spectrum.

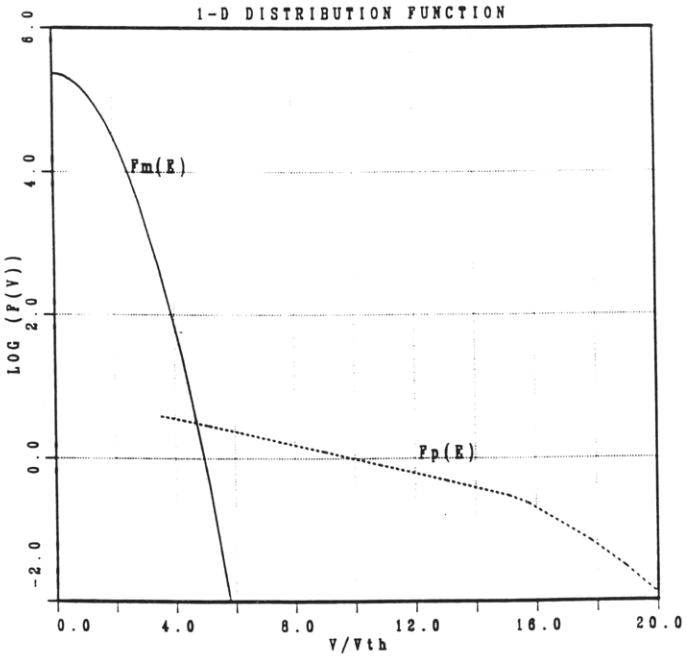

Figure 7-8: The 1-D electron distribution function used to calculate the enhanced Langmuir wave spectrum. The ordinate is in units of m^{-4}sec, while the abscissa is normalized by the electron thermal velocity, V_{te}.

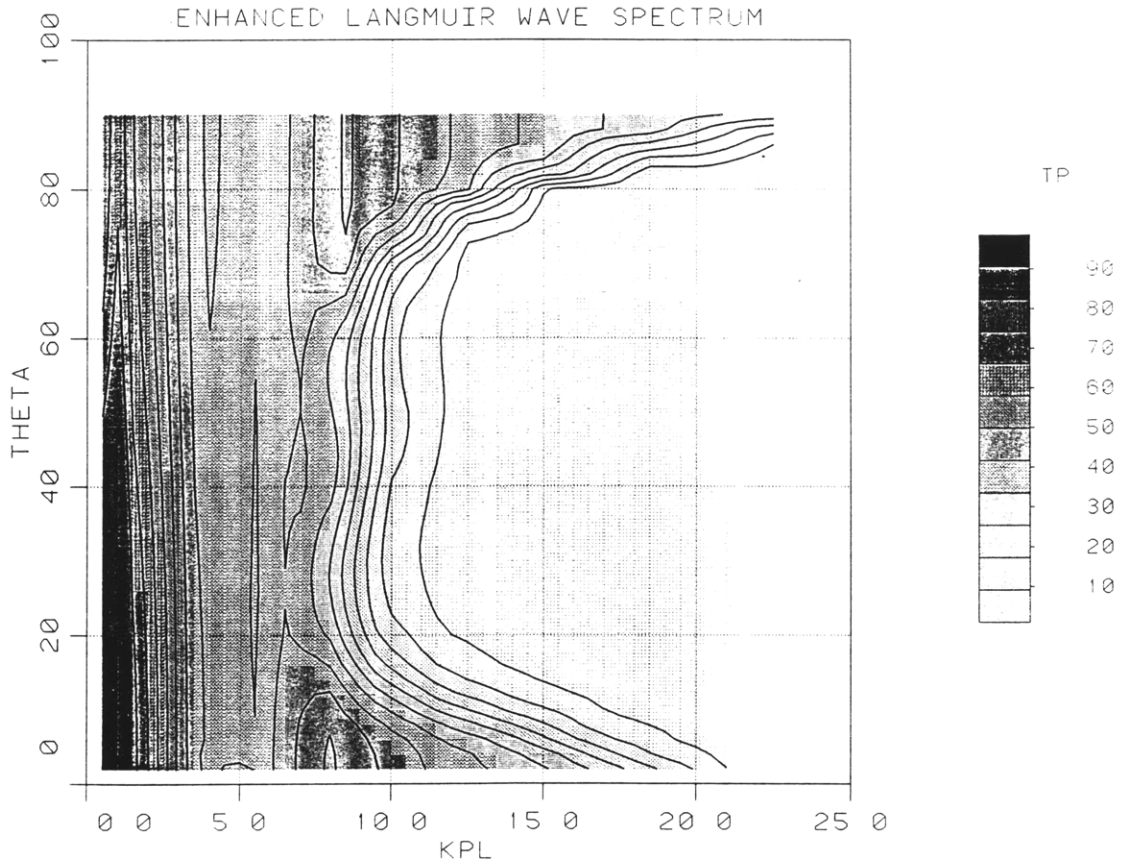

Figure 7-9: Spectrum of Langmuir waves excited by suprathermal electrons as a function of K, wavenumber, and θ, aspect angle with respect to the geomagnetic field.

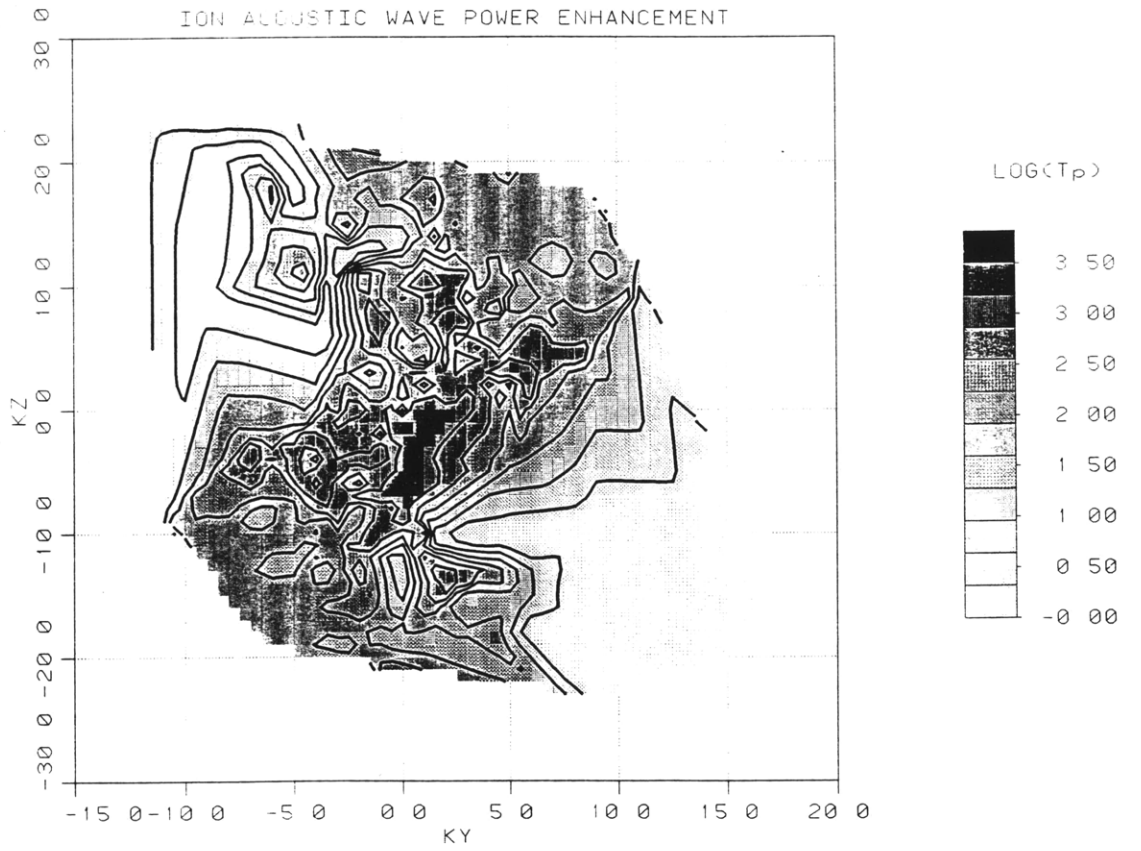

Figure 7-10: Enhancement of ion acoustic wave modes as a function of parallel (KZ) and perpendicular (KY) wavenumbers.

ter radar is sensitive, $k \sim 18.5$ m^{-1}, up to two orders of magnitude enhancement are predicted depending on the aspect angle of the wave mode ($\theta = \tan^{-1}[\mathrm{KZ/KY}]$). Up to three orders of magnitude enhancement are possible for wave numbers of ~ 9 m^{-1}, corresponding to a radar frequency of 224 MHz. No enhancement is predicted at wavenumbers exceeding 20 m-1 in this calculation because the assumed flux of low energy electrons (≤ 10 eV) was too small. The theory predicts increasing enhancements for longer wavelengths.

The predicted enhancement of wave modes with large aspect angles relative to the magnetic field was somewhat unexpected because the suprathermal electron distribution used in the calculation was assumed to be field-aligned. This is partly due to the fact that the highest energy electrons excite Langmuir waves at all aspect angles as mentioned previously, and partly because T_p' is derived from a product of two Langmuir wave modes whose difference frequency and wave vector match those

of ion acoustic modes. Considering all possible combinations of appropriate modes one finds it is possible for the field-aligned electrons to couple energy through the Langmuir waves into a broad spectrum of ion acoustic modes. In addition, the ion acoustic wave spectrum is simultaneously enhanced in both downward and upward directions along the field line.

The enhanced spectrum of Langmuir waves shown here may actually be conservative. Larger amplification of such waves has been measured on rockets in auroral arcs [*Ergun*, 1989; *McFadden, et al.*, 1986]. However, these measurements are made with fixed length booms, sampling a single scale size corresponding to the length of the boom, typically a few meters. These relatively long wavelengths are excited by very high energy particles and do not contribute significantly to the enhancement of ion acoustic modes detectable with radars. It is not clear that the enhanced intensities observed at long wavelengths can be extrapolated to the radar wavelength regime.

Suprathermal electron source

The suprathermal particles which act as the driving source for this mechanism are generally associated with field-aligned currents at auroral latitudes. Field-aligned currents in the ionosphere are usually driven by a significant electric potential drop parallel to the magnetic field in the magnetosphere, which accelerates electrons down the field lines into the ionosphere. Recent satellite observations, however, indicate that strong field-aligned currents are sometimes associated only with suprathermal electron bursts in the absence of a significant parallel potential drop [*Marshall, et al.*, 1991; *Johnstone and Winningham*, 1982]. Rocket measurements in auroral arcs have also detected intense, variable fluxes of low energy electrons [*Boehm, et al.*, 1990], apparently accelerated by large amplitude Alfvén waves as described by Goertz and Boswell [1979] and Temerin et al. [1986]. In each case, the currents are accompanied by a substantial suprathermal electron population capable of driving ion acoustic

waves through nonlinear Langmuir wave coupling.

7.3 Discussion of Results

The methods elucidated in RR have been employed recently to model ion acoustic wave power enhancements, but even the assumption of very large current densities ($\sim 1 - -10$ mamps/m^2) is inadequate to produce the magnitudes of the observed effects ($\sim$20 dB) [FOS88; RD91; COLL91] as will be shown in the next section.

7.3.1 Interpreting Observations with RR

Millstone Hill UHF Data

Figure 7-11 shows an observed spectrum enhanced by a factor of 5 (top, solid curve) and a theoretical spectrum modeled after RR which shows the same enhancement (bottom, solid curve). To model the observed spectrum it is necessary to construct a composite spectrum via the superposition of three separate spectra having assumed values of T_r of 1, 5, and 9, respectively [FOS88]. Varying T_r is not unreasonable since the data are integrated for 30 seconds and the enhancement process most probably evolves over this time period. In addition to the relatively high T_r values, the 25 km/sec drift velocity required to produce the enhancement is essentially equivalent to the instability threshold critical velocity and corresponds to a 400 $\mu amp/m^2$ current.

EISCAT UHF data

In Figure 7-12 RD91 provide the results of the RR model output of ion line spectra for several different bulk electron parallel drift velocities for the observed value of $T_r = 3$. Qualitatively, the asymmetric model spectra look similar to observed UHF radar backscatter enhancements; but, even for an assumed drift of 100 km/sec (current

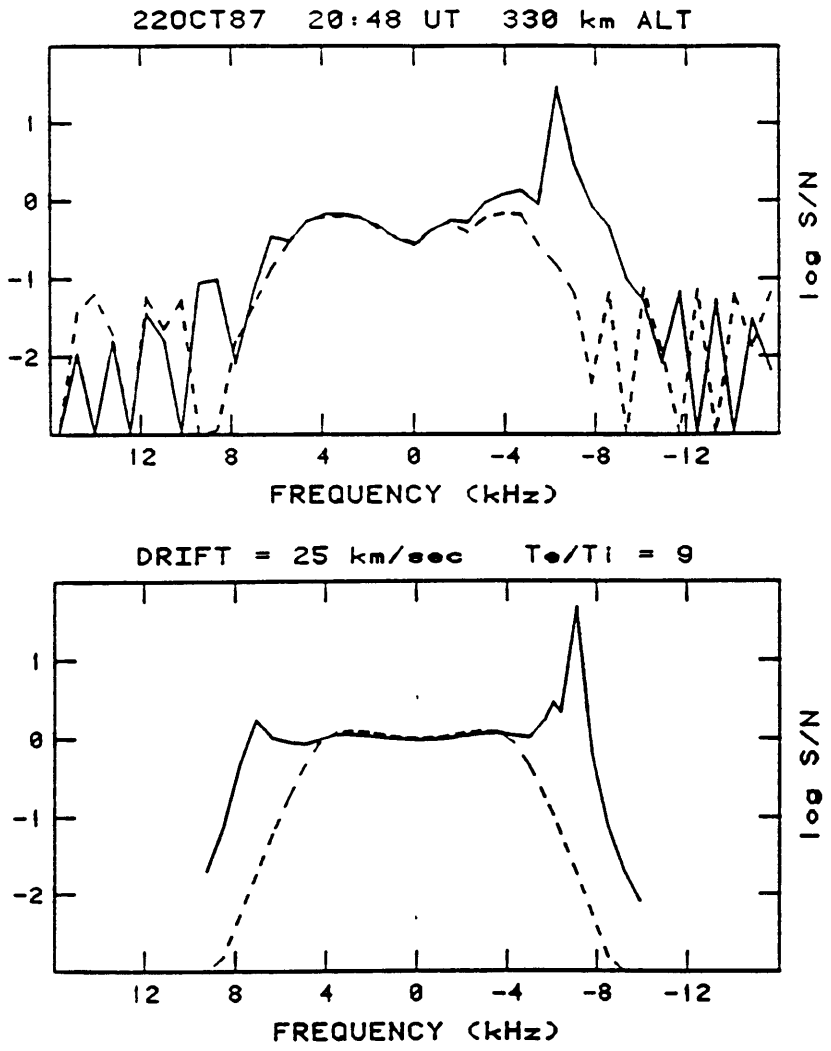

Figure 7-11: a) 7 dB acoustic enhancement observed with Millstone Hill UHF radar (solid line). b) Simulation of enhancement using RR model, assuming $T_r = 1$, 5, and 9 in ratios of 6:2:1, respectively, during a 30 second integration period [after FOS88].

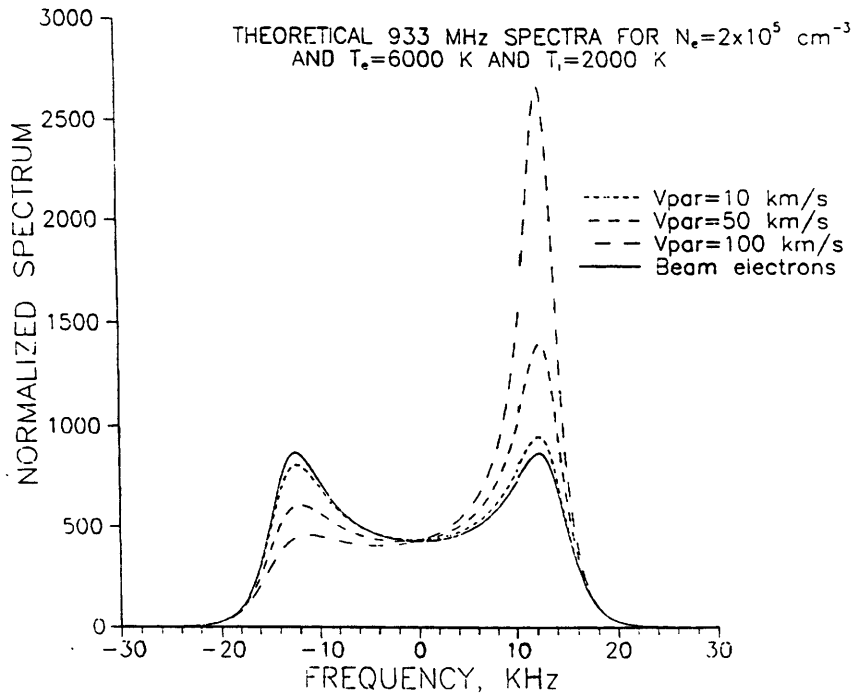

Figure 7-12: Theoretical ion line spectra for selected electron drift velocities for the EISCAT UHF radar. Although the asymmetry increases rapidly, the maximum enhancement in total cross section is only 25% [after RD91].

$\simeq 3$ *mamps*/m^2) equal to the critical velocity, the total cross section is enhanced by only 25%, less than 1 dB. By comparison, the observed cross sections were up to two orders of magnitude greater than normal incoherent scatter returns.

EISCAT VHF data

Figure 7-13 contains a pair of spectra observed with the 224 MHz radar and the corresponding theoretical fits (solid line) obtained by applying the RR model [COLL91]. The correlation between the two is quite good, giving reasonable estimates of the density and temperature ($T_r \simeq 3$) of the ionospheric plasma for the 6–7 dB enhancements. The model electron drift velocity required to achieve these results, however, was barely subthreshold implying a huge current density of a few milliamps per square meter. Furthermore, the fitting program failed entirely when applied to the larger, $\sim$ 15 dB enhancements reported in COLL91; instabilities of the type discussed by

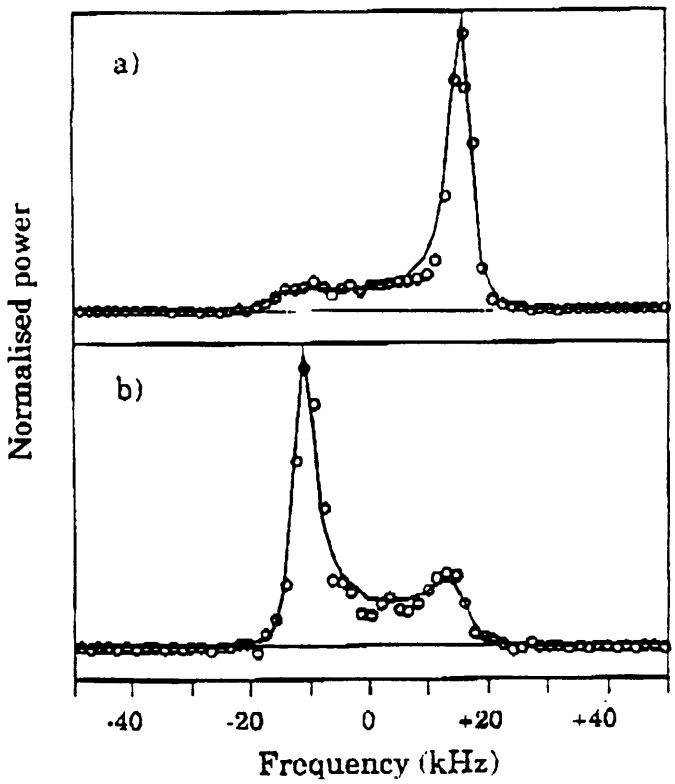

Figure 7-13: 6–7 dB Enhanced spectra observed with the EISCAT VHF radar and the corresponding theoretical fit applying the RR analysis (solid line). The fitting program failed to reproduce spectra exhibiting larger enhancements.

KK were assumed to be responsible for those.

Summary of RR Interpretation

The theory of RR applied to the observed enhancements of ion acoustic waves in the ionosphere produces mixed results. It correctly identifies the important role of soft (near thermal) electrons in the enhancement process, as confirmed by associated red airglow emissions, and the decreasing of the threshold drift velocity for increasing wavelength [COLL91]. The threshold velocity predicted by RR also decreases for elevated electron temperatures and temperature ratios, consistent with measurements reported by RD91 and COLL91, and the association drawn by FOS88 with topside density depletions in the ionospheric trough. However, the RR mechanism appears incapable of explaining other features of the observed data.

The most obvious feature is the magnitude of the enhanced radar backscatter

cross section. Pushing the theory to the limit of validity by assuming nearly critical electron drift velocities produces cross section enhancements of at most 10 dB; several observed enhancements approach 20 dB. Moreover, the large drift velocities required, attributed to bulk electrons, translate into current densities which are huge by ionospheric standards, $\sim$ 1-10 $mamps/m^2$. Currents of this intensity are 1–2 orders of magnitude greater than those that have been reported from in situ satellite measurements [*Bythrow et al.*, 1984; *J. D. Winningham*, private communication, 1988].

Qualitatively, the RR model describes the aesthetic features of some of the data, but important differences arise even at this level of application. Specifically, the theory predicts that an enhancement of one side of the spectrum be accompanied by a reduction in the other side. This is inevitable because of the underlying physics as explained in Section 7.1.1. More commonly the observations are characterized by an enhancement, albeit asymmetric, in both peaks of the spectrum. A possible explanation for this has been offered by RD91; namely, that the enhanced peaks are separated temporally on time scales not resolved by the 10 second integration period, or that opposing currents are flowing adjacent to one another on small spatial scales which cannot be resolved by the radar beam, some four kilometers in diameter at 400 km altitude.

These arguments may apply to some of the data. However, the persistence of some of the observed enhancements, particularly those detected with the EISCAT VHF radar (4 min. duration), and the large velocity gradients inherently implied by the small spatial scales suggested, raises doubts about the widespread adoption of these explanations for the large number of spectra exhibiting both upshifted and downshifted peak enhancements (nearly 40% of the more than 500 topside geophysical UHF ERB events found at EISCAT to date). An additional argument for simulta-

neous enhancements may be based on the distribution of the types of enhancements observed.

In Figure 7-14 the total number of ion acoustic ERB events recorded at EISCAT to date are categorized as being either upshifted, downshifted or symmetric enhancements and binned according to altitude. At higher altitudes, the distribution is dominated by symmetric enhancements. If this were due simply to inadequate measurement resolution in space or time (that is, the symmetric enhancements are simply superpositions of asymmetric enhancements of opposite peaks), one would also expect the number of downshifted and upshifted enhancements, relative to each other, to be roughly equal. Surprisingly, however, there are nearly twice as many downshifted peaks as upshifted at these altitudes, suggesting that the radar is not randomly smearing out the effects of a phenomenon which fluctuates between upshifts and downshifts on small spatial–temporal scales. One must either explain the proper mix of upshifted and downshifted enhancements at high altitudes in geophysical terms, or accept that the symmetric enhancements can be simultaneously stimulated and represent a limitation of the RR theory.

The application of the RR theory with regard to the detection of enhanced ion lines by a radar pointed at large aspect angle relative to the direction of the electron drift velocity produces mixed results. Enhancements occur only when the electron drift direction is perpendicular to the plane of reflection of the radar waves (see Figure 7-1). For backscatter geometry, this implies the drift must be parallel (or antiparallel) to the radar beam to observe enhancements. Backscatter observations of large enhancements extended along the magnetic field lines obtained with the radar pointed up the field lines are consistent with this interpretation. For remote sites diagnosing the same volume at large aspect angles, however, the field-aligned drift direction does not satisfy the geometry in Figure 7-1 with respect to the scattered waves and much weaker

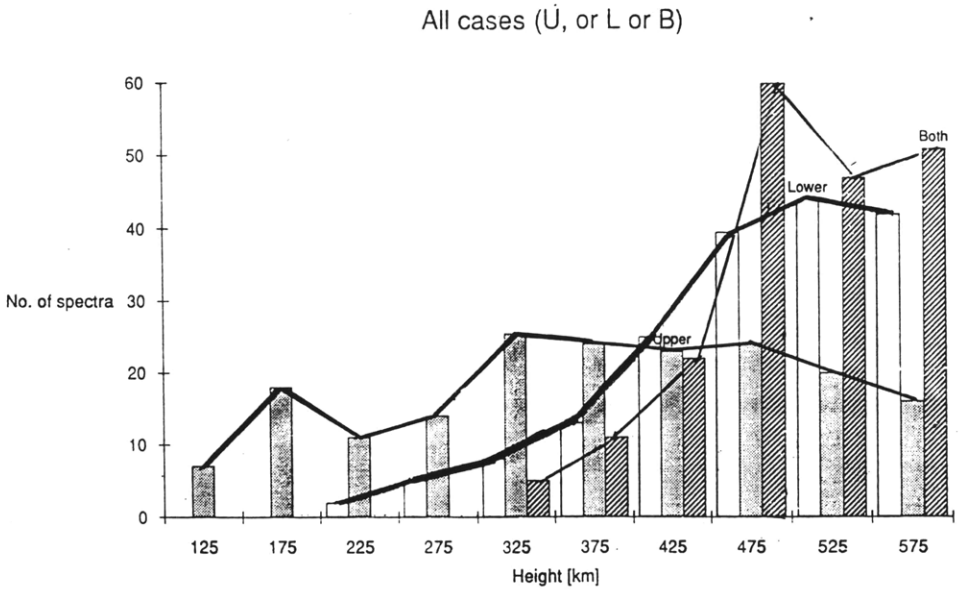

Figure 7-14: Histogram showing relative numbers of upshifted, downshifted and symmetric enhancements of the ion line recorded by the EISCAT UHF radar [after *M. Rietveld*, private communication, 1991].

enhancements would result. Thus, the theory seems consistent with the absence of EISCAT UHF remote site observations noted previously.

However, most of the ERB observations at Millstone Hill, Sondreström and several from EISCAT have been acquired at aspect angles of 20° or more with respect to the magnetic field. The well established zenith observations at all three sites also represent measurements at significant non-zero aspect angles. An interpretation of these observations with the RR mechanism would suggest that the assumed electron drifts are not always highly field-aligned. Some satellite measurements of intense currents have shown that the current-carrying electron fluxes were field-aligned by factors of about four to one [*J. D. Winningham*, private communication, 1988], which would not produce enhanced spectra at aspect angles greater than about 20° based on the RR mechanism. It is difficult to calculate the maximum aspect angle at which enhanced scattering can be detected because the exact nature of the currents inducing the enhancements is not well known. The conclusion that can be stated is that electron currents flowing obliquely at angles of up to 30° to the magnetic field are required by RR theory to explain the observations of ERB at large aspect angles.

7.3.2 Interpretations Based on KK Theory

The processes investigated by KK are valid in the drift velocity regime where RR's mechanism is no longer applicable. Their theory provides quantitative guidelines to which ion wave modes are least stable for given ionospheric conditions, and the growth rates of the various wave modes once the critical instability velocity is exceeded. Despite widespread recognition of its importance, detailed application of this theory to existing data has been limited for a couple of reasons.

One reason stems from the fact that the observations consist of enhancements of ion acoustic waves in the ionosphere. KK's work indicates that ion cyclotron wave

modes are destabilized at significantly lower drift velocity thresholds than acoustic waves, except for T_r values greater than about 20 in O^+ plasmas. Having no previous evidence that such large temperature ratios exist in the ionosphere, one must either accept this interpretation as first proof, or consider alternative explanations for the growth of the ion acoustic waves.

One such alternative is that the cyclotron waves do become unstable first, but the electric fields inducing the electron velocity drifts accelerate them beyond the acoustic wave threshold anyway. The cyclotron modes are strongly field-aligned and would probably be undetected by radar waves propagating at small aspect angles relative to the magnetic field, as is the case for the experiments considered here. That still leaves the problem of invoking an acceleration mechanism sufficiently robust to withstand unknown levels of energy loss due to the excitation of cyclotron waves, and proceed to destabilize ion acoustic waves. Sorting out such issues is nontrivial and requires significant additional theoretical investigation.

Another reason for lack of utilization of KK's results is simply the difficulty of comparing the theory's predictions with existing observations of enhanced spectra. The theory predicts which modes will be excited and at what rate, but it doesn't prescribe what the spectral shape will be and how large the waves will grow before saturating, characteristics generally determined by complicated nonlinear processes not treated by KK.

7.3.3 Implications of Nonlinear Langmuir Wave Coupling

As can be seen in Figure 7-10, the nonlinear wave coupling mechanism predicts significant enhancements in the cross section of ion acoustic modes observed by UHF radars. Furthermore, the enhancements are larger for longer wavelengths (smaller k), in agreement with the observations of COLL91 at VHF frequencies. These results are

also provided by the theories of KK and RR, though for different reasons.

A unique aspect of the wave coupling process is its prediction of enhancements for both upshifted and downshifted spectral peaks simultaneously. This can occur because the coupling mechanism excites the ion acoustic waves via the low frequency ponderomotive force due to the beating of intense Langmuir waves. Even though the Langmuir wave spectrum consists of waves moving primarily in the direction of the suprathermal electron flux responsible for their excitation, the various beating combinations of the waves can nonlinearly couple energy into a broad spectrum of ion waves. The symmetrically enhanced spectra are commonly observed (see Chapter 6), and previous explanations for their occurrence have been unsatisfactory.

With regard to the observations of ERB at large aspect angle relative to the magnetic field, the nonlinear coupling theory predicts enhancements of the ion acoustic waves over a broad spectrum of wave vectors. The result is that, even for the field-aligned distribution function assumed in the calculation of enhanced modes, ion acoustic waves are enhanced up to 10 dB at propagation angles up to 45° across the field-aligned direction (see Figure 7-10). Not surprisingly, the enhancement levels decrease as the aspect angle increases, though they are still significant. Thus, the nonlinear coupling theory provides an explanation for the observations of ERB at significant aspect angles.

A notable feature of the wave coupling mechanism is that the underlying physics are completely different from previous theories. In RR and KK, the wave modes grow because of a shift in the thermal electron distribution function; when the shift exceeds the phase velocity of ion wave modes, the *ion* waves grow at the expense of the electron kinetic energy in a wave–plasma interaction. In the nonlinear coupling process, on the other hand, streaming electrons stimulate *electron* waves initially. The energy is then transferred to ion wave modes via the nonlinear beating of the high frequency plasma

waves in a wave–wave interaction. The difference in the mechanisms is important to understand because both types of interactions may occur simultaneously, each contributing to the overall enhancement of ion acoustic waves in the ionosphere.

A Note on Distribution Functions

The intensity of the predicted enhancements of ion modes via nonlinear coupling is sensitive to the electron distribution function assumed in the calculation. In particular, the choice of the suprathermal component, f_p, affects the results significantly. In the calculation presented here and illustrated in Figures 7-9 and 7-10, actual satellite data was utilized in constructing the electron distribution function down to energies of 5 eV, about 20 times greater than the electron thermal energy. Nevertheless, the resulting f_p is based on a composite of three measurements and does not represent an "ensemble average" for auroral events; rather, it represents a *possible* distribution function for the ionosphere which may not be typical, but is by no means extraordinary, either.

A different f_p would produce a different enhancement spectrum than the one shown here. For example, if the low energy electron component ($\leq$ 50 eV) is omitted, a substantial reduction in the enhancement of short wavelength ion modes results. These modes are the very ones detected by UHF radars, indicating the importance of the the low energy particle population. Altering either the slope or the magnitude of f_p at any energy can cause significant changes in the final enhancement spectrum. Nevertheless, the general features of the enhancements shown here are preserved provided the assumed distribution function is characterized at low energies by a modest slope which steepens gradually with increasing electron energy and intersects the thermal electron population at about $5V_{th}$.

An intriguing possibility involves inverting the calculation to infer electron distribution functions from an observed ion line spectrum. Besides posing nontrivial math-

ematical obstacles, an attempt to perform this procedure faces an issue of uniqueness, since more than one distribution function can produce essentially identical enhancements. However, it may be possible with reasonable apriori assumptions and additional investigation to infer information about the suprathermal electron distribution function from enhanced incoherent scatter spectra.

7.4 Summary of ERB at Ion Acoustic Frequencies

Suprathermal electrons associated with field-aligned currents can excite a broad spectrum of Langmuir waves within the space plasma. Significant enhancement of ion acoustic waves through nonlinear Langmuir wave coupling is apparently possible when the local electron distribution function has a substantial nonthermal component, as in the presence of intense field-aligned currents. This mechanism may play an important role, acting in conjunction with other current driven processes, such as RR and KK, in amplifying the radar cross section of ion modes. It predicts important observed effects such as the simultaneous enhancement of upshifted and downshifted spectral peaks, increasing levels of enhancement for increasing wavelengths, and the enhancement of modes at large aspect angles. The RR mechanism explains only asymmetric enhancements. The most commonly observed ERB spectra exhibit enhancements of both peaks with moderate levels of asymmetry. These spectra may represent a superposition of effects described by the nonlinear coupling and RR theories, respectively, since they are based on different physical processes and can contribute to ERB independently. Calculations of current density which omit the contribution of the nonlinear wave coupling mechanism may seriously overestimate the intensity of the field-aligned currents associated with the observed ion line enhancements.

Chapter 8

Summary and Conclusions

8.1 Significant Results

Several important results have been found in the investigation of nonlinear ionospheric interactions with VLF and UHF radio waves. A summary of these results can be segregated naturally by the frequency regimes of the specific interactions.

8.1.1 VLF wave-plasma interactions

The spectral broadening of VLF waves reported by Bell et al. [1983] refers to the apparent bandwidth expansion (up to 10% of the carrier frequency) of monochromatic VLF waves launched from ground-based transmitters and received by satellites in the topside ionosphere. Nonlinear scattering of the incident VLF waves by ionospheric density irregularities with scale lengths not exceeding several tens of meters has been identified theoretically as a potential source mechanism for this phenomenon. We have found that the scattered wave is an elliptically polarized, quasi-electrostatic mode, consistent with observations, with an enlarged spectrum of wave numbers. The apparent broadening results from the Doppler shift induced by the motion of the satellite-borne receiver; the magnitude of the shift is directly proportional to the

wave numbers of the short scale length modes.

When the amplitude of the VLF wave becomes sufficiently large, parametric processes generating lower hybrid waves and density irregularities are predicted theoretically. The first process excites zero frequency field-aligned fluctuations by the beating interaction of VLF waves and lower hybrid waves when the electric field strength of the VLF waves exceeds a few millivolts per meter. The density fluctuations can induce apparent VLF spectral broadening by scattering the incident VLF waves nonlinearly as described above.

In the second process, these lower hybrid waves generate high frequency lower hybrid sidebands and low frequency field-aligned modes. The lower hybrid sidebands are predicted to be upshifted and downshifted from the carrier frequency. This would explain spectral broadening observations of a suppression of the satellite received signal at the carrier frequency. The upshifted mode has a relatively small phase velocity and can accelerate electrons and ions effectively, causing the formation of density irregularities and enhanced airglow in the ionosphere. The threshold amplitude for this instability decreases rapidly with altitude, ranging from more than 1000 mvolts/m below 800 km altitude to about 25 mvolts/m above 1000 km, due to decreasing plasma density and the transition from heavier to lighter ion species. These thresholds are not easily exceeded by ground-based transmitters, and this mechanism is therefore not believed to be the dominant process responsible for spectral broadening. However, the excitation of these processes in the near field of the 10 kW VLF transmitter aboard the ACTIVE satellite was anticipated.

A series of unique UHF radar backscatter experiments involving VLF transmissions from the satellite were conducted at Millstone Hill and Arecibo Observatory. The immediate vicinity of the ACTIVE satellite was diagnosed for evidence of enhanced radar backscatter induced by the powerful VLF waves. Ground based VLF

receivers were also deployed to record spectral characteristics for comparison with measurements acquired onboard a moving subsatellite. The results of these experiments are inconclusive, with no strong evidence supporting the excitation of parametric instabilities by the VLF waves. The probable cause stems from the severely degraded performance of the onboard VLF antenna; radiated power was reduced by at least 20 dB, below the threshold values required for parametric excitations.

8.1.2 UHF propagation effects

The recently observed dramatic enhancements of UHF radar backscatter (ERB) under naturally occurring conditions have been identified as the growth of ion acoustic wave modes in the presence of intense field-aligned currents in the ionosphere [FOS88, RD91, COLL91]. Observational efforts to investigate this phenomenon at Millstone Hill include the statistical reduction of large data sets to remove hard target contamination, multi-diagnostic experiments (MICAD), and zenith radar experiments.

The statistical analyses are basically of two types, using satellite velocity distributions or satellite altitude distributions to infer the presence of geophysical ERB events. The catalog distributions have been compared to the corresponding distributions of coherent echoes found in large data sets, typically from low elevation angle azimuth scans. In one experiment (13–15JAN88) conducted under very disturbed conditions (Kp$>$ 6), it was not possible to statistically infer the presence of geophysical ERB based on a comparison of the observed and simulated coherent echo velocity distributions. The data were acquired by scanning the radar in a restricted azimuth range to the north at a 4° elevation angle. The apparent lack of geophysical ERB is attributed to the equatorward expansion of the active auroral region to the south of Millstone Hill during the major magnetic storm which commenced for two of the three observing days.

Velocity distribution comparisons performed for another experiment (8–10NOV87) conducted during moderately disturbed conditions show the presence of an anomalously large number of coherent echoes observed at ion acoustic frequencies. Because the distributions are based on approximately 60 hours of data they are statistically significant. Some of the echoes in the ion acoustic regime are attributed to geophysical ERB occurring at auroral latitudes.

A third experiment (6-10MAR89) was conducted under magnetic conditions that varied from moderately to very disturbed ($3 \leq \mathrm{Kp} \leq 6$). Comparisons of the observed and simulated velocity distributions for this experiment were inconclusive. However, an anomalously large number of enhanced echoes were observed at low altitudes during three time periods when the equatorward storm surge approached Millstone Hill from the north. No ion acoustic echoes were observed at low altitudes on the days of moderate disturbance. These results are interpreted as the signature of the auroral region approaching the close proximity of the Millstone Hill radar and inducing ERB events. Because the normally distant active region expanded to mid-latitudes, we were able to observe the ERB at low altitudes and separate the returns from those due to hard targets.

Another long radar experiment (6–10OCT86) analyzed by the statistical comparison methods yielded no interesting results in either the velocity or altitude distributions. This experiment was conducted under very quiet conditions. The conclusion is that no ERB occurred at high or mid-latitudes due to a lack of activity.

In the May 22, 1989 MICAD experiment, ion acoustic ERB was observed in conjunction with in situ measurements of intense field-aligned currents and large fluxes of soft suprathermal electrons. The radar backscatter was enhanced by 7 dB above the normal incoherent scatter signal from an ionospheric plasma density of $4.1 \times 10^4\ cm^{-3}$. The ERB observation occurred about 30 seconds prior to the in

situ detection of intense field-aligned currents ($\sim$ 50 $\mu amps/m^2$) in nearly the same spatial volume. Three additional satellite passes through the same latitude band before and after these observations show that region was characterized by large fluxes of soft precipitating electrons and current activity for several tens of minutes. These observations establish the association of suprathermal electron fluxes and enhanced radar backscatter.

ERB events at ion acoustic frequencies have also been detected in zenith radar experiments at Millstone Hill, EISCAT and Sondreström. The zenith pointing direction is significant because it constrains the possible Doppler shifts from hard targets to nearly zero magnitude; coherent echoes detected at the ion sound speed can unambiguously be attributed to geophysical mechanisms. Zenith ERB observations are acquired at nonzero aspect angles with respect to the magnetic field. At Millstone Hill, this angle is about 18°. Because we are not looking parallel to the enhancements in the zenith case, the echoes appear to be localized targets, though some extension in range is possible (see Figure 5-17).

Radar observations of ERB from EISCAT show that the enhancements can be extended in range for at least 500 km along the magnetic field line. These enhancements are accompanied by large magnetometer fluctuations ($\sim$ 500 nT), elevated electron temperatures ($3000° \leq T_e \leq 6000°$), and red aurora. The magnitude of the enhancements is up to 20 dB relative to normal incoherent backscatter, though enhancements of 5–10 dB are seen more commonly. Many weaker enhancements have probably not been found yet due to sensitivity limitations of the automated detection algorithm. About 38% of the topside spectra were enhanced symmetrically, 37% were asymmetrically enhanced downshifted peaks, and the remaining 25% were asymmetrically enhanced upshifted peaks.

Nonlinear Wave Coupling Theory

Previous explanations of the ion acoustic ERB phenomenon have been based on the theories of RR and KK. A new mechanism has been presented whereby the growth of ion acoustic waves is accomplished through the nonlinear coupling of intense Langmuir waves. The high frequency Langmuir wave spectrum is generated by large fluxes of suprathermal electrons associated with auroral arcs and field-aligned currents. This mechanism occurs under the same geophysical conditions associated with the observations; namely, elevated electron temperatures, local magnetometer fluctuations, and red aurora.

The theory predicts increasing excitation of ion acoustic modes with increasing wavelengths, in agreement with RR and KK. Unlike either of the previous explanations, however, the nonlinear wave coupling mechanism can produce simultaneous enhancements in both upshifted and downshifted ion acoustic modes, a commonly observed feature at EISCAT. This is possible because the coupling mechanism excites ion acoustic waves over a broad spectrum of wave vectors via the low frequency ponderomotive force due to the beating of intense Langmuir waves.

The broad spectrum of enhanced ion acoustic waves resulting from the nonlinear wave coupling process also explains the observations of ERB at nonzero aspect angles at Millstone Hill, EISCAT and Sondreström. Significant enhancements are predicted at aspect angles up to 45°, even when the suprathermal electron flux responsible for the excitation of the Langmuir waves is assumed to be precisely field-aligned. The RR theory allows for nonzero aspect angle ion acoustic growth only when the electron drift velocity has a cross-field component. The magnitudes of the cross-field component in field-aligned currents is not well known, but it is estimated that enhancements due to the RR theory would be restricted to aspect angles less than about 20°.

The underlying physics of the nonlinear wave coupling and the RR processes,

respectively, are quite different. The RR process is triggered by bulk electron drifts which have the effect of increasing the radar backscatter from ion density fluctuations moving with the drift and decreasing backscatter from antiparallel fluctuations. In the nonlinear coupling process, electrons first transfer their energy to high frequency electron plasma waves via collisionless damping; these waves then beat together nonlinearly to drive low frequency ion acoustic modes. The two mechanisms can act in conjunction to cause the observed amplification of the ion acoustic waves. The most commonly observed ERB spectra at EISCAT are characterized by enhancements in both peaks which are slightly to moderately asymmetric. Such spectra may well represent a superposition of the contributions of the RR mechanism and the nonlinear wave coupling process.

Appendix A

Equations of Motion for Ionized Gases

The fluid equations are commonly used to describe many phenomena in ionospheric plasmas. They are given below.

A.1 Fluid Equations

Momentum Conservation

$$mn(\frac{\partial}{\partial t} + \mathbf{v}\cdot\nabla)\mathbf{v} = nq(\mathbf{E} + \mathbf{v}\times\mathbf{B}) - \nabla p - mn\nu\mathbf{v} \tag{A.1}$$

Continuity Equation

$$\frac{\partial}{\partial t}n + \nabla\cdot(n\mathbf{v}) = 0 \tag{A.2}$$

Equations (A.1) and (A.2) are repeated for each species (e.g., ions, electrons). The quantities represented in the equations are

m particle mass

n density

$\mathbf{v}$ particle velocity

$\mathbf{q}$ particle charge

$\mathbf{E}$ macroscopic electric field

$\mathbf{B}$ macroscopic (static) magnetic field

ν neutral-particle collision frequency

The left hand side of equation (A.1) is the normal convective derivative. The first term on the right hand side represents the electromagnetic Lorentz force on charged particles; the second term represents the pressure gradient force; the last term approximates the momentum lost through charged particle-neutral collisions. Equation (A.2) is the familiar expression for the conservation of particles. Additional equations are the thermodynamic equation of state and Maxwell's equations.

Equation of State

$$p = C\rho^{\gamma} \tag{A.3}$$

where C is a constant, ρ is the density, and γ is the ratio of specific heats, C_p/C_v.

Maxwell's Equations

$$\nabla \cdot \mathbf{E} = \sigma/\epsilon_o \tag{A.4}$$

$$\nabla \times \mathbf{E} = -\frac{\partial}{\partial t}\mathbf{B} \tag{A.5}$$

$$\nabla \cdot \mathbf{B} = 0 \tag{A.6}$$

$$\nabla \times \mathbf{B} = \frac{1}{c^2}\frac{\partial}{\partial t}\mathbf{E} + \mu_o \mathbf{J} \tag{A.7}$$

The charge and current densities are then given by

$$\sigma = \sum_j n_j q_j \qquad (j = i, e) \tag{A.8}$$

$$\mathbf{J} = \sum_j n_j q_j \mathbf{v}_j \tag{A.9}$$

These equations form the complete set of commonly used fluid equations.

A.2 Kinetic Equations

Although the fluid equations provide a valid description of many plasma processes, they do not predict interesting wave–particle interactions in plasmas; specifically, the collisionless damping and excitation of plasma waves by charged particles. The dynamics of the plasma in the kinetic approach are specified in terms of a smooth distribution function of particles, $f(\mathbf{r}, \mathbf{v}, t)$, rather than averaged, macroscopic quantities such as velocity and density. The distribution function represents the ensemble average (in 6-dimensional **r**-**v** phase space) of the individual particles in the system. The plasma kinetic equation describes the evolution of $f(\mathbf{r}, \mathbf{v}, t)$ in time and space.

Plasma Kinetic Equation

$$\frac{\partial}{\partial t} f(\mathbf{r}, \mathbf{v}, t) + \mathbf{v} \cdot \frac{\partial}{\partial \mathbf{r}} f(\mathbf{r}, \mathbf{v}, t) + \frac{q}{m} (\mathbf{E} + \mathbf{v} \times \mathbf{B}) \cdot \frac{\partial}{\partial \mathbf{v}} f(\mathbf{r}, \mathbf{v}, t) = C \tag{A.10}$$

This equation is repeated for each particle species present. The C on the right side of the equation represents a collision operator which couples the distribution functions of all interacting species. For many problems of physical interest (e.g., processes above 150 km altitude), collisions may be neglected; the right hand side of equation (A.10) vanishes and is known as the famous *Vlasov Equation* of plasma physics.

$$\frac{\partial}{\partial t} f(\mathbf{r}, \mathbf{v}, t) + \mathbf{v} \cdot \frac{\partial}{\partial \mathbf{r}} f(\mathbf{r}, \mathbf{v}, t) + \frac{q}{m} (\mathbf{E} + \mathbf{v} \times \mathbf{B}) \cdot \frac{\partial}{\partial \mathbf{v}} f(\mathbf{r}, \mathbf{v}, t) = 0 \tag{A.11}$$

The kinetic Maxwell equations are identical to equations (A.4)–(A.7) provided the definitions for charge (A.8) and current (A.9) densities, respectively, are changed to

zeroth and first order velocity averages of the distribution function:

$$\sigma = \sigma_{ext} + \sum_j q_j \int d^3v \; f_j(\mathbf{r}, \mathbf{v}, t) \tag{A.12}$$

$$\mathbf{J} = \mu_o \mathbf{J}_{ext} + \mu_o \sum_j q_j \int d^3v \; \mathbf{v} \, f_j(\mathbf{r}, \mathbf{v}, t) \tag{A.13}$$

Generally, the distribution function for a given species is assumed to have the form ($f(\mathbf{r}, \mathbf{v}, t) = f_o + f_1 + ...$) where f_o is assumed to be a Maxwellian distribution, and f_1 (and possibly higher order terms) is treated as a small perturbation about f_o. The equations are then linearized to simplify solutions. These equations are closely related to the fluid equations. In fact, a direct method to derive the fluid continuity and momentum equations consists of taking the zeroth and first order velocity moments, respectively, of the plasma kinetic equation.

Appendix B

Review of Parametric Instability Theory

The parametric excitation of wave modes in space plasmas generally refers to a non-linear process whereby two or more waves grow at the expense of another wave, which supplies the free energy and is usually referred to as the "pump" wave.

B.1 Linear Wave Coupling

To understand this process involving the nonlinear coupling of multiple waves, let us first consider the simpler process of linear wave coupling involving only two waves, in which energy from a source wave is coupled into another wave mode excited in the medium. Identifying the source wave as the driving term (E_o) and the excited wave as the response of the medium (x) which has a natural oscillation frequency (ω), we can describe the process mathematically by a simple driven harmonic oscillator equation,

$$\frac{d^2x}{dt^2} + \omega^2 x = E_o \tag{B.1}$$

Without solving the equation we know that if the source wave drives the system at

its resonant frequency, ω, the energy will be absorbed effectively and large amplitude waves will be excited. An example of a physical process in which this occurs is the coupling of electromagnetic waves into electrostatic electron cyclotron waves in a magnetized plasma.

When injected electromagnetic waves match the frequency at which the electrons in the plasma gyrate around the magnetic field lines, the wave energy is absorbed efficiently by accelerating the electrons causing the growth of so-called cyclotron waves. This process is commonly used to heat plasmas in laboratory experiments. Parametric excitation of multiple wave modes is more complicated than this simple example of wave coupling, but a similar treatment may be used to explain its general features.

B.2 Three Wave Parametric Processes

A parametric instability may involve the interaction of three or four different plasma waves. For simplicity, a three wave process is considered here.

B.2.1 Harmonic Oscillator Analogy

Mathematically, the parametric process is described in a manner analogous to a system of coupled harmonic oscillators. The oscillators, x_1 and x_2, are driven by an external force, E_o, and coupled by constants, c_1 and c_2, respectively. The equations of motion are (following *Chen*, [1984]),

$$\frac{d^2x_1}{dt^2} + \omega_1^2 x_1 = c_1 x_2 E_o \tag{B.2}$$

$$\frac{d^2x_2}{dt^2} + \omega_1^2 x_2 = c_2 x_1 E_o \tag{B.3}$$

Here ω_1 and ω_2 represent the resonant frequencies of x_1 and x_2, respectively, but the oscillators have finite Q; that is, they can respond to a range of frequencies about the resonance. If we let $x_1 = \tilde{x}_1 \cos\omega_1' t$ and $x_2 = \tilde{x}_2 \omega_2' t$ and express the driving term as

$E_o = \tilde{E}_o \cos \omega_o t$, equation B.2 becomes

$$\begin{aligned}(\omega_2{}^2 - \omega'_2{}^2)\tilde{x}_2 \cos \omega'_2 t &= c_2 \tilde{E}_o \tilde{x}_1 \cos \omega_o t \cos \omega'_1 t \\ &= c_2 \tilde{E}_o \tilde{x}_1 \frac{1}{2}\{\cos[(\omega_o + \omega'_1)t] + \cos[(\omega_o - \omega'_1)t]\} \quad \text{(B.4)}\end{aligned}$$

The driving terms on the right can excite oscillators x_2 with frequencies

$$\omega'_2 = \omega_o \pm \omega'_1 \quad \text{(B.5)}$$

Thus, x_2 can be driven only at the difference and sum frequencies of the driver and the other excited mode. The driving terms can cause a frequency shift so that ω'_2 is only approximately equal to ω_2. In addition, ω'_2 can be complex in a physical system since there is damping (neglected for simplicity) or, possibly, growth in the case of an instability.

If we assume small frequency shifts and damping or growth rates, so that $\omega'_2 \approx \omega_2$, then (B.5) imposes a frequency matching condition,

$$\omega_o \approx \omega_2 \pm \omega_1 \quad \text{(B.6)}$$

The assumption of small frequency shifts in plasmas is valid because off resonant modes are heavily damped, effectively prohibiting their excitation.

If the oscillators represent waves in a plasma, we must include a spatial dependence in the sinusoids and replace ωt by $\omega t - \mathbf{k} \cdot \mathbf{r}$. Then there is also a wavelength matching condition,

$$\mathbf{k_o} \approx \mathbf{k_2} \pm \mathbf{k_1} \quad \text{(B.7)}$$

In this simple treatment, we have shown that the excited waves' frequencies and wave vectors are only approximately equal to those of resonant wave modes; equation (B.5) is strictly true and represents nothing more than conservation of energy (multiply each side of the equation by Planck's constant, $\hbar$). Similarly, (B.7) states conservation of momentum.

Bibliography

[1] Abreu, V. J., and H. C. Carlson, Photoelectron energy loss and spectral features deduced by the plasma line technique, *J. Geophys. Res., 82*, 1017–1023, 1977.

[2] Appleton, E. V., and M. A. F. Barnett, Local reflection of wireless waves from the upper atmosphere, *Nature, 115*, 333-334, 1925.

[3] Bell, T. F., H. G. James, U. S. Inan, and J. P. Katsufrakis, The Apparent spectral broadening of VLF transmitter signals during transionospheric propagation, *J. Geophys Res., 88*, 4813–4840, 1983.

[4] Boehm, M. H., C. W. Carlson, J. P. McFadden, J. H. Clemmons, and F. S. Mozer, High–resolution sounding rocket observations of large–amplitude Alfvén waves, *J. Geophys. Res., 95*, 12157–12171, 1990.

[5] Breit, G., and M. A. Tuve, A radio method of estimating the height of the conducting layer, *Nature, 116*, 357, 1925.

[6] Buonsanto, M. J., J. C. Foster, A. D. Galasso, D. P. Sipler, and J. M. Holt, Neutral winds and thermosphere/ionosphere coupling and energetics during the geomagnetic disturbances of March 6–10, 1989, *J. Geophys Res., 95*, 21033–21050, 1990.

[7] Bythrow, P. F., T. A. Potemra, W. B. Hanson, L. J. Zanetti, C.-I. Meng, R. Huffman, F. Rich, and D. Hardy, Earthward directed high-density Birkeland currents observed by HILAT, *J. Geophys. Res., 89*, 9114–9118, 1984.

[8] Chen, F., *Introduction to Plasma Physics and Controlled Fusion*, Plenum Press, 309–315, 1984.

[9] Cicerone, R. J., and S. A. Bowhill, Photoelectron fluxes measured at Millstone Hill, *Radio Sci., 6*, 957-966, 1971.

[10] Collis, P. N., L. Häggström, K. Kaila, and M. T. Rietveld, EISCAT radar observations of enhanced incoherent scatter spectra; their relation to red aurora and field-aligned currents, *Geophys. Res. Lett., 18*, 1031–1034, 1991.

[11] Dougherty, J. P., and D. T. Farley, A theory of incoherent scattering of radio waves by a plasma, *Proc. Roy. Soc. (London), A259*, 79–99, 1960.

[12] Ergun, Robert E., Linear and nonlinear wave processes in the auroral ionosphere, U. C. Berkeley, Ph. D. Dissertation, 1989.

[13] Evans, J. V., Theory and practice of ionosphere study by Thomson scatter radar, *Proceedings of the IEEE, 57*, 496–530, 1969.

[14] Farley, D. T., A plasma instability resulting in field-aligned irregularities in the ionosphere, *J. Geophys. Res., 68*, 6083–6097, 1963.

[15] Fejer, J., Scattering of radiowaves by an ionized gas in thermal equilibrium, *Can. J. Phys., 38*, 1114–1133, 1960.

[16] Foster, J. C., C. del Pozo, K. Groves, and J.–P. St. Maurice, Radar observations of the onset of current driven instabilities in the topside ionosphere, *Geophys. Res. Lett., 15*, 160–163, 1988.

[17] Foster, J. C., J. R. Burrows, and P. M. Banks, High latitude ionospheric troughs associated with inward directed Birkeland currents, *EOS, 57*, 1976.

[18] Goertz, C. F., and R. W. Boswell, Magnetosphere–ionosphere coupling, *J. Geophys. Res., 82*, 2235, 1977.

[19] Groves, K. M., M. C. Lee, and S. P. Kuo, Spectral broadening of VLF radio signals traversing the ionosphere, *J. Geophys. Res., 93*, 14683–14687, 1988.

[20] Gurnett, D. A., and L. A. Frank, VLF Hiss and Related Plasma Observations in the Polar Magnetosphere, *J. Geophys. Res., 77*, 172, 1972.

[21] Hagfors, T., Density fluctuations in a plasma in a magnetic field, with applications to the ionosphere, *J. Geophys. Res., 66*, 1699–1712, 1961.

[22] Helliwell, Robert A., *Whistlers and Related Ionospheric Phenomena*, Stanford University Press, 121-123, 1965.

[23] Inan, U. S., and T. F. Bell, Spectral broadening of VLF transmitter signals observed on DE 1: A quasi-electrostatic phenomenon?, *J. Geophys. Res., 90*, 1771–1775, 1985.

[24] Inan, U. S., T. F. Bell, and H. C. Chang, Particle precipitation induced by short-duration VLF waves in the magnetosphere, *J. Geophys. Res., 87*, 6243–6264, 1982.

[25] Johnson, N. L., History and consequences of on-orbit breakups, *Adv. Space Res., 5*, 11–19, 1985.

[26] Kessler, D. J., Orbital debris issues, *Adv. Space Res., 5*, 3–10, 1985.

[27] Kindel, J. M., and C. F. Kennel, Topside current instabilities, *J. Geophys. Res., 76*, 3055–3078, 1971.

[28] Koons, H. C., B. C. Edgar, and A. L. Vampola, Precipitation of inner zone electrons by whistler mode waves from VLF transmitters UMS and NWC, *J. Geophys. Res., 86*, 640–648, 1981.

[29] Kuo, S. P., and M. C. Lee, Stimulated scattering instability of lower hybrid waves, *Phys. Fluids, 29*, 1024, 1986

[30] Lamb, George L., The scattering of electromagnetic waves by nonequilibrium plasmas, *Los Alamos Scientific Laboratory Internal Report*, LA–2715, 1962.

[31] Laaspere, T., W. C. Johnson, and L. C. Semprebon, Observations of auroral hiss, LHR noise and other phenomena in the frequency range 20 Hz–540 KHz on OGO 6, *J. Geophys. Res., 76*, 4477, 1971.

[32] Lee, M. C., Ion line enhancement in ionospheric heating experiments, *J. Phys. D: Appl. Phys., 14*, 851–860, 1981.

[33] Lee, M. C., and S. P. Kuo, Production of lower hybrid waves and field-aligned density striations by whistlers, *J. Geophys. Res., 89*, 10873–10880, 1984.

[34] Marshall, J. A., J. L. Burch, J. R. Kan, P. H. Reiff, and J. A. Slavin, Sources of field–aligned currents in the auroral plasma, *Geophys. Res. Lett., 18*, 45–48, 1991.

[35] Mayaud, P. N., *Derivation, Meaning and Use of Geomagnetic Indices*, AGU Geophysical Monograph 22, 1980.

[36] McEwen, D. J., and R. E. Barrington, Some characteristics of the lower hybrid resonance noise bands observed by the Alouette I satellite, *Can. J. Phys., 45*, 13, 1967.

[37] McFadden, J. P., C. W. Carlson, and M. H. Boehm, High-frequency waves generated by auroral electrons, *J. Geophys. Res., 91*, 12079–12088, 1986.

[38] Perkins, Francis, and E. E. Salpeter, Enhancement of plasma density fluctuations by nonthermal electrons, *Phys. Rev., 139*, A55–A62, 1965.

[39] Pines, David and David Bohm, A collective description of electron interactions: II. Collective vs individual particle aspects of the interaction, *Phys. Rev., 85*, 338–353, 1952.

[40] Providakes, J., D. T. Farley, W. E. Swartz, and D. Riggin, Plasma irregularities associated with a morning discrete auroral arc: Radar interferometer observations and theory, *J. Geophys. Res., 90*, 7513–7523, 1985.

[41] Rietveld, M. T., P. N. Collis, and J.–P. St. Maurice, Naturally enhanced ion acoustic waves in the auroral ionosphere observed with the EISCAT 933–MHz radar, *J. Geophys. Res., in press*, 1991.

[42] Rishbeth, H., Basic physics of the ionosphere: A tutorial review, *J. IERE, 58*, S207–S223, 1989.

[43] Rosenbluth, M. N., and N. Rostoker, Scattering of electromagnetic waves by a non-equilibrium plasma, *Phys. Fluids, 5*, 776–788, 1962.

[44] Salpeter, E. E., Electron density fluctuations in a plasma, *Phys. Rev, 120*, 1528–1535, 1960.

[45] Salpeter, E. E., Plasma density fluctuations in a magnetic field, *Phys. Rev, 122*, 1663–1674, 1961.

[46] Schlegel, K., and D. R. Moorcroft, Unusual *F*-region echoes observed with EISCAT, *Max-Planck-Institut für Aeronomie internal report*, MPAE-W-05-89-13, 1989.

[47] *ACTIVE space plasma–wave laboratory* Acad. of Sci. of the USSR, Space Research Institute Report, 1987.

[48] Storey, L. R. O., An investigation of whistling atmospherics, *Phil. Trans. Roy. Soc. (London), A246*, 113–141, 1953.

[49] Swanson, D. G., *Plasma Waves*, Academic Press, 1989.

[50] Sudan, R. N., J. Akinrimisi, and D. T. Farley, Generation of small scale irregularities in the equatorial electrojet, *J. Geophys. Res., 78*, 240, 1973.

[51] Temerin, M., J. McFadden, M. Boehm, C. W. Carlson, and W. Lotko, Production of flickering aurora and field–aligned electron flux by electromagnetic ion cyclotron waves, *J. Geophys. Res., 91*, 5769, 1986.

[52] Thomson, J. J., *Conduction of Electricity Through Gases*, Cambridge University Press, London, 1906.

[53] Ungstrup, E., W. J. Heikkila, J. C. Foster, and W. O. Lennartsson, Compositional changes, time and density variations in the magnetosphere associated with Birkeland currents and particle acceleration, *Adv. Space Res., 6*, 113-116, 1986.

[54] Wahlund, J.-E., H. J. Opgenoorth, L. Häggström, K. J. Winser, and G. O. L. Jones, EISCAT observations of topside ionospheric ion outflows during auroral activity: Revisited, *J. Geophys. Res., in press*, 1991.

[55] Yngvesson, K. O., and F. W. Perkins, Radar Thomson scatter studies of photoelectrons in the ionosphere and Landau damping, *J. Geophys. Res., 73*, 97–109, 1968.

